Integrated Readout at the Quantum-Classical Interface of Semiconductor Qubits

Alice Charlotte Mahoney
School of Physics
University of Sydney

A thesis submitted for the degree of
Doctor of Philosophy

2017

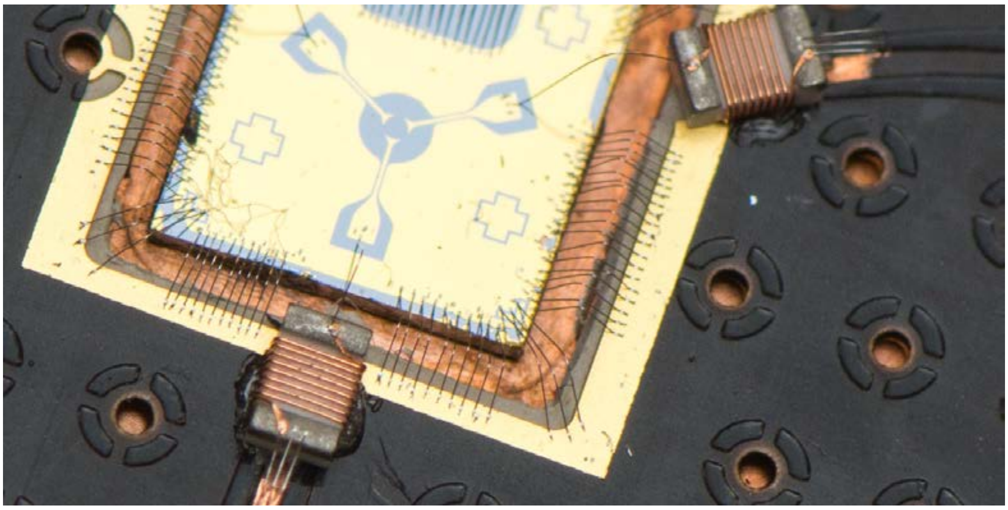

Supervisor:
Prof. David J. Reilly

Author:
Alice C. Mahoney

Associate supervisor:
Prof. Andrew C. Doherty

Integrated readout at the quantum-classical interface of semiconductor qubits

Abstract

Quantum computing promises to deliver uniquely powerful information processing machines, by exploiting the quantum phenomena of superposition and entanglement. In solid-state systems, there has been significant progress in the isolation and control of the fundamental units needed to build such machines, known as *qubits*. However, scaling-up the number of qubits to the point where sophisticated algorithms can be performed presents considerable experimental challenges. In particular, it is becoming increasingly apparent that a new class of tools will be required to interface between fragile quantum systems, and the classical readout and control hardware of the outside world.

This thesis presents experimental investigations towards the development of a scalable readout architecture for semiconductor qubit platforms. Fast readout of a GaAs-AlGaAs double quantum dot in the few-electron regime is first demonstrated via an embedded dispersive gate sensor (DGS), alleviating the burden of requiring separate charge sensors for every qubit. The sensitivity and bandwidth of this technique are extracted and benchmarked against well-established readout methods. Dispersive gate sensing of quantum point contacts (QPCs) is then presented, probing charge rearrangement within the local electrostatic environment of quasi one-dimensional channels. A low-loss, lumped-element, *LC* resonant circuit is also implemented for frequency multiplexed readout.

The second set of experiments concern the design and characterisation of miniaturised, on-chip circulators based on the quantum Hall effect, and the quantum anomalous Hall effect. Microwaves are first capacitively coupled into edge magnetoplasmon modes in a mesoscopic GaAs-AlGaAs droplet. Non-reciprocal forward transmission comparable to off-the-shelf components is observed, which is accounted for within an interferometric picture. This circulator design is then extended to thin films of the three-dimensional topological insulator, Cr-doped $(Bi,Sb)_2Te_3$, wherein similar non-reciprocity is demonstrated in the absence of an external magnetic field.

Declaration

This thesis comprises peer-reviewed publications, unpublished experiments, and designs and techniques developed over the course of my PhD. All work was undertaken in the Quantum Nanoscience Lab at the University of Sydney, under the supervision of Professor David Reilly. Chapters 1 and 2 review the literature and theory which motivate this work, while Chapters 3 - 7 present new results. Full author lists for Chapters 3 - 7 are included in the section *Publications*, and author contributions and affiliations are listed at the end of each chapter. For all published work, permission to include data in this thesis has been granted by the corresponding author. If not otherwise acknowledged, the work presented in this thesis is my own.

Signed ....

Alice Charlotte Mahoney

Date: June 2017

Acknowledgements

> *“The best that most of us can hope to achieve in physics is simply to misunderstand at a deeper level” ∼ Wolfgang Pauli*

Over the course of my PhD, I have been fortunate enough to work with a great number of people who have helped inspire a passion for and deepen my (mis)understanding of physics.

First and foremost, I would like to thank my supervisor, David Reilly, for convincing me to join the quantum nanoscience lab (QNL), introducing me to the field of condensed matter physics, and for enabling me to work on such interesting projects. David’s tutelage, direction and encouragement throughout my PhD have been invaluable, and have helped me to challenge myself and grow as a researcher.

In addition, I am grateful to have been part of the quantum physics group at the University of Sydney, and the ARC Centre of Excellence for Engineered Quantum Systems, EQuS. Thank you to Stephen Bartlett, Andrew Doherty and Mike Biercuk for many useful chats, journal clubs, and for fostering such a lively academic community. In particular, I have benefited enormously from discussions and collaborations with Andrew, who has helped me to both think deeper about physics, and learn how to build an intuition for theory.

The QNL has been a great place to do a PhD, due in no small amount to the students, post-docs, and engineers I have been able to work alongside. Again, I would be remiss not to mention David’s role in leading by example to create an environment of hard work, humility, and good humour, which has attracted so many dedicated and generous scientists. John

Hornibrook has been a constant presence throughout my time in the QNL, across all three labs. His level-headedness, dry humour, and readiness to trouble-shoot fridge problems at any time of day or night has been very much appreciated. Ewa Rej has likewise been a great role model from the very beginning, inspiring lab members with her perseverance amidst experimental challenges and immaculate log-booking. I am grateful to have been able to work on many projects with James Colless, whose work ethic and dedication to understanding all aspects of an experiment set a benchmark for lab work during the early years of the QNL. James' generosity with his time, and willingness to discuss physics or rf electronics is truly appreciated. Finally, the last of the original lab crew, thanks to Xanthe Croot who I have had the privilege of learning physics with over the past decade. Xanthe's determination, optimism, and tireless energy (whether in regards to understanding phonons, cryogenics or marathon running) has been inspirational and a great motivator. I would also like to acknowledge the assistance of David, John, James, and Seb, for proof-reading and providing comments on various sections of this thesis.

It has been exciting to see the QNL expand (in terms of people, lab size, and research directions) over the course of my time here. I am grateful to Slyvain Blainvillain who taught me the tricks and, perhaps more importantly, mindset to succeed in semiconductor nanofabrication. I thank Ian Conway Lamb who selflessly shared his knowledge of mechatronic engineering, drones and Youtube videos (mostly related to mechantronic engineering and drones), and Seb Pauka, whose diligence, edifications to my coding and many great quotes will not be forgotten. I have also enjoyed watching MC Jarratt transition into a fridge repair and nanofab expert over the past couple of years, and have appreciated Steven Waddy's[1] efforts to improve our experimental set-ups by critically analysing each resistor and grounding configuration. In addition, I have been fortunate to spend time with and learn from 'Team NMR'- Torsten Gaebel, David Waddington, and Tom Boele. I have also enjoyed working alongside Romain Bara, Harry Steel, and the new engi-

---

[1] Photograph on page iii courtesy of Steven Waddy.

neering recruits, including Kushal Das and many others.

Perhaps one of the things I have most enjoyed during my PhD has been the opportunity to interact with and learn from a global community of physicists. I would like to acknowledge the staff at the ANFF UNSW node, especially Joanna Syzmanska, for nanofabrication support and training. Thank you to Hong Lu and Art Gossard from UCSB who provided us with the GaAs-AlGaAs wafers that enabled us to measure the first quantum dots in the QNL. Thanks also to Geoff Gardner, John Watson, and Mike Manfra from Purdue University for supplying us with high mobility heterostructures that were the basis for the quantum Hall plasmonics experiments described in this thesis. I am particularly grateful for the nanofabrication and measurement support provided by John Watson.

I was fortunate to meet David DiVincenzo during a conference early on in my PhD, and I thank him and Stefano Bosco from RWTH Aachen University for many fruitful discussions which culminated in the work in Chapter 6 of this thesis. Collaborating with Lucas Peeters, Eli Fox and David Goldhaber-Gordon from Stanford University on the quantum anomalous Hall experiments in Chapter 7 was a great experience from which I learned a lot. Thank you also to Xufeng Kou, Lei Pan, and Kang Wang from UCLA for enabling us to perform measurements on such exciting material systems ($(\mathrm{CrBiSb})_2\mathrm{Te}_3$).

I also benefited significantly from being able to attend the Microsoft Station Q meetings at UCSB, and to gain a broader perspective of the field. In particular, thank you to Mike Freedman, Charlie Marcus and Leo Kouwenhoven for taking the time to explain many new areas of physics to me, and for the opportunity to learn about and take measurements on a new material system during the final stages of my PhD (proximitised nanowires). Thank you also to Chetan Nayak and Jen Cano for many useful contributions and insights into the quantum Hall experiments presented in Chapter

6 of this thesis.

I am indebted to the administration team within the School of Physics at USYD, in particular those who worked with the QNL. Leanne Price, Wicky West, and Alexis George's tireless efforts have allowed for the smooth day-to-day running of the lab, and kept me afloat during my PhD. Thanks also go to the School of Physics workshop and technical support team, for their assistance building and machining parts for the experiments in this work.

Last but certainly not least, thanks to my friends, house mates and family for providing both distraction and perspective when I needed it, and to my parents, for their never-ending support and encouragement.

Included Publications

Listed below are details of the papers that have been included in this thesis. Asterisks indicate authors contributed equally.

Chapter 3 - “Dispersive readout of a few-electron double quantum dot with fast rf gate sensors”
Physical Review Letters, **110**, 046805 (2013).
J. I. Colless, **A. C. Mahoney**, J. M. Hornibrook, A. C. Doherty, H. Lu, A. C. Gossard, and D. J. Reilly

Chapter 4 - “Frequency multiplexing for readout of spin qubits”
Applied Physics Letters, **104**, 103108 (2014).
J. M. Hornibrook, J. I. Colless, **A. C. Mahoney**, X. G. Croot, S. Blanvillain, H. Lu, A. C. Gossard and D. J. Reilly

Chapter 5 - “Dispersive gate sensing the local electrostatic environment of a quantum point contact”
In preparation, (2017).
A. C. Mahoney, X. G. Croot, H. Lu, A. C. Gossard, J. D. Watson, G. C. Gardner, M. J. Manfra, and D. J. Reilly

Chapter 6 - “On-chip microwave quantum Hall circulator”
Physical Review X, **7**, 011007 (2017).
A. C. Mahoney*, J. I. Colless*, S. J. Pauka, J. M. Hornibrook, J. D. Watson, G. C. Gardner, M. J. Manfra, A. C. Doherty, and D. J. Reilly

Chapter 7 -“Zero-field edge magnetoplasmons in a magnetic topological insulator”
ArXiv preprint, arXiv:1703.03122 (2017).
A. C. Mahoney*, J. I. Colless*, L. Peeters*, S. J. Pauka, E. J. Fox, X. Kou, Lei Pan, K. L. Wang, D. Goldhaber-Gordon, and D. J. Reilly

Contents

List of Figures

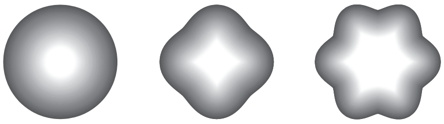

0

Outline

"I don't know anything, but I do know that everything is interesting if you go into it deeply enough." ~ *Richard Feynman*

BUILDING a quantum computer is a truly formidable quest that has inspired a generation of physicists. Richard Feynman was one of the earliest minds to recognise the transformative effect that quantum physics might have on computing, and how the combination of the two could push the limits of our understanding of the physical world. In a speech in 1981, he postulated that to perform calculations capturing the quantum mechanical laws of nature, a simulator is required that is itself quantum mechanical [1]. Since then, algorithms have been found that use the quantum phenomena of superposition and entanglement to more efficiently solve a range of key problems, from factoring large numbers to searching unsorted databases, which are presently intractable on classical computers [2, 3].

The catch, however, is that in order to realise such a machine, we first need to push the limits of our ability to access the fundamental building blocks of nature. Experimentally, this effort requires at once the isolation of individual quantum systems, as well as a means of accessing the information held within- aims that can often be conflicting. Towards quantum computation, individual quantum bits (qubits) must be controllably coupled to each other and to the tools used to probe them, but importantly not to environmental channels which can lead to the loss of coherence. The techniques and structures designed for qubit readout and control must therefore be both highly sensitive as well as non-invasive. Working towards constructing such a toolbox is a key driver of this thesis, which presents a number of experiments concerning the fast readout of semiconductor qubits. In particular, this work focuses on the development of compact, highly-integrated readout architectures, such as what will be required as the number of qubits is scaled-up towards implementing sophisticated algorithms. This thesis is divided into three main parts:

Part I

Part I serves as an primer to the theory and body of literature that lay the foundations for the experiments presented in this work. In Chapter 1, two-dimensional electron gases formed in GaAs-AlGaAs heterostructures are explored, followed by an introduction to quantum dots, and quantum point contacts (QPCs). Chapter 2 describes some of the physics underlying the integer, fractional, and quantum anomalous Hall effects, as well as edge magnetoplasmons.

Part II

Part II details experimental results focusing on fast, scalable readout of quantum dots in GaAs-AlGaAs. A demonstration of dispersive gate sensing (DGS) of a double quantum dot via a confining gate electrode is presented in Chapter 3. The bandwidth and sensitivity of this approach are extracted and benchmarked against traditional charge sensing techniques. In Chapter 4, a superconducting, lumped-element, readout scheme is presented, designed for addressing large arrays of qubits. Frequency multiplexed readout of a double quantum dot is performed using both a DGS and an rf-QPC. Chapter 5 details a preliminary investigation into the local electrostatic environment of QPCs, using dispersive gate sensing. Unexpected features in the dispersive response for asymmetric QPC gate geometries are investigated.

Part III

Part III focuses on harnessing quantum Hall plasmonics for directional signal routing in semiconductor-based qubit systems. Chapter 6 first details microwave absorption of quantum Hall edge states in a GaAs-AlGaAs mesoscopic droplet coupled to a coplanar transmission line. This technique is then extended to the implementation of an on-chip quantum Hall circulator using chiral edge magnetoplasmons at high magnetic fields. Chapter 7 presents a similar circulator device fabricated using thin films of the three-dimensional topological insulator- Cr-doped $(\mathrm{Bi,Sb})_2\mathrm{Te}_3$. Non-reciprocal rf transmission is demonstrated via robust conducting edges at zero magnetic field, and the effects of lattice temperature and incident power are discussed.

The final chapter reflects on this body of work as a whole, and suggests future directions for the experiments presented here.

Appendix

Appendices *A* through *F* include supplemental text, figures and technical details relevant to the experiments presented in this work. This includes supporting data, nanofabrication recipes, and further details and schematics of the experimental setups.

Part I

Background and theory

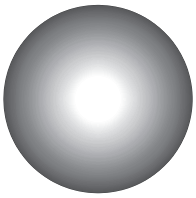

1

Transport in GaAs-AlGaAs two-dimensional electron gases

The following two chapters introduce some of the relevant theory and literature to provide a formal context for the experiments in Parts II and III of this work. For a more detailed coverage of theoretical and experimental progress in the field, a selection of useful reviews are referenced throughout.

THE last 50 years have witnessed significant theoretical and experimental progress within the field of condensed matter physics. Importantly, many of the experimental breakthroughs have been made possible by advances in the technology used to synthesise, measure, and provide the environmental conditions necessary to probe matter at the nanoscale. This has enabled physicists to observe order and emergent phenomena across a variety of quantum systems. The discoveries of the integer and fractional quantum Hall effects [4, 5] are two key examples where the advent of new technologies[1] played a crucial role. These discoveries spurred on a worldwide investigation into new phases of matter, and have since been recognised as the first experimental examples of topologically protected systems.

Here we introduce some of the physics underlying electron systems within epitaxially-grown semiconductor layer stacks. In particular, we focus on two-dimensional electron gases formed in GaAs-AlGaAs heteorstructures a few thousandths of a degree above absolute zero. Chapter 1 explores zero-dimensional quantum dots - so-called ‘artificial atoms’, before turning to quasi one-dimensional quantum point contacts (QPCs). In these systems, quantised transport can be observed in the natural units of e^2/h, where e is the charge of a single electron and h is Planck’s constant. In Chapter 2, we extend this discussion to the quantum Hall effect, where the application of a perpendicular magnetic field leads to quantised behaviour in these same units, but with precision of almost one part per billion.

1.1 Mesoscopic physics in solid-state systems

1.1.1 Electronic band theory

In order to introduce the important length and energy scales for the systems described in this work, and to motivate the platform of semiconductors, we begin with a discussion of electronic band structure in solid-state systems (for details and background see Refs. [7, 8, 9, 10, 11]). Electron states in crystalline materials can be described by solutions to the Schrödinger equation in a periodic potential, called Bloch waves. These single-particle energy eigenstates are expressed for a lattice position r, and wave vector k, in

---

[1] Dilution refrigeration, molecular beam epitaxy, and the development of modulation doping were all integral to these discoveries [6]

the form

$$\psi_{n,k}(r) = e^{ik\cdot}u_{n,k}(r) \tag{1.1}$$

where the function $u_{n,k}(r)$ relates to the periodicity of the crystal lattice, and the term $e^{ik\cdot r}$ denotes the solutions as plane waves [8]. The subscript n is an integer and gives the band index, grouping together electronic energy levels, $E_{n,k}$. Gaps in between these bands correspond to energetically forbidden regions.

Within this picture, free electrons in a system fill up the allowable energy levels from lowest to highest. This filling takes into account the Pauli exclusion principle, prohibiting two electrons with the same quantum numbers from occupying a single state. The kinetic energy of each electron is given by

$$E = \frac{p^2}{2m} \tag{1.2}$$

where p is the canonical momentum $hk/2\pi$ or $\hbar k$, and m is the electron mass. The Fermi energy, E_F is defined at $T = 0$ as the energy of the highest filled electronic state. In momentum space, the locus of points spanned by E_F forms an effective 3D surface of gapless electronic excitations. Inside the surface lies a sea of electrons, while outside the surface only empty states exist. As $k = 2\pi/\lambda$, it follows then that the Fermi wavelength λ_F, can be understood as setting the minimum wavelength that electrons in a material can possess [11]:

$$\lambda_F = \frac{h}{\sqrt{2mE_F}}. \tag{1.3}$$

In metals, λ_F is of order a few Ångström (10^{-10} m) and E_F lies within a partially filled energy band known as the *conduction* band (e.g. in Cu, λ_F ~0.46 nm and $E_F \sim$ 7 eV [12]). Here the presence of nearby available states that electrons can scatter into facilitates the flow of electric current, with only a small additional energy required.

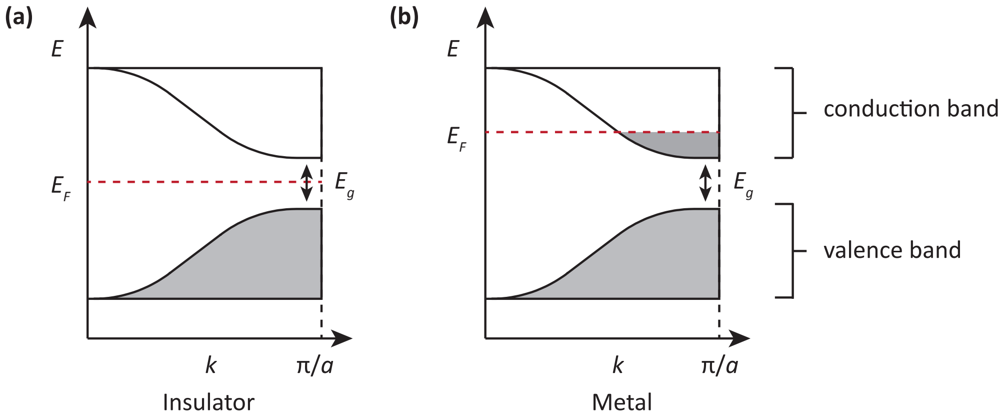

Figure 1.1: Energy band diagrams. The conduction and valence bands are shown for an insulator **(a)**, and a metal **(b)**, within the first unit cell in reciprocal, k space. a represents the lattice constant while E_g denotes a gap between the two bands. Electrons are filled up to the Fermi level, E_F - indicated by red dashed line. In metals (shown in (b)), this results in a partially filled conduction band with nearby free-states to facilitate transport. Adapted from Ref. [10].

Insulators on the other hand are characterised by a fully filled band of valence electrons with a gap, E_g to the empty conduction band. At $T > 0$ the Fermi level denotes an occupation probability of 0.5 and lies within this space, preventing electrical conduction. These two cases are schematically shown in Fig. 1.1.

For semiconductors (which are the focus of this work), E_F similarly falls within a gap at $T = 0$ K [10]. However unlike in insulators, a small fraction of the electrons in semiconductors can be thermally excited into the unoccupied states in the conduction band, giving rise to electrical transport. Further, the introduction of a small amount of dopants or impurities into semiconductor stacks can lead to the addition of extra energy levels near the band edges, enabling the conductivity to be varied significantly. The carrier density is then related to the density of dopants, which leads to values of $\lambda_F \sim$ tens of nanometres (an order of magnitude larger than in metals) [11].

From a practical point of view, in order to confine single electrons within systems of size L, there are two other important length scales we need to introduce. These are the elastic and inelastic scattering lengths, l_e and l_i [11]. l_e refers to the distance between collisions of electrons with impurities, or with lattice defects, over which the total kinetic energy and momentum are conserved. The inelastic scattering length, l_i, is related to the distance that electrons can travel before losing phase coherence from interactions with other electrons or phonons.

With these length scales in mind, we now specify two key physical constraints for isolating electrons in crystalline materials. Firstly, the Fermi wavelength must be large enough so that it is of order the physical box we are able define with current technologies. Secondly, l_e and l_i must be much longer than L or λ_F to prevent loss of energy or phase information. Semiconductors provide an attractive platform due to the large characteristic wavelength and the cleanliness of the samples which can be synthesised (e.g. l_e can be over 150 μm in certain III-V semiconductor materials). In addition, in recent decades the use of electron beam lithography has allowed on-chip structures tens of nanometres across to be defined. For certain semiconductor structures it is therefore possible to experimentally confine electrons satisfying all of the conditions

$$\lambda_F, L < l_e < l_i. \tag{1.4}$$

In these systems, the individual charges behave like missiles ricocheting off walls. This is known as the quantum ballistic transport regime.

1.1.2 GaAs-AlGaAs heterostructures

Gallium arsenide- aluminium gallium arsenide (GaAs-AlGaAs) heterostructures have historically represented some of the most desirable environments in which to confine and study single electrons (for reviews, see Refs. [13, 14]). This section gives a brief background of these semiconductor layer stacks and summarises a few key characteristics. As flagged above, the ubiquity of this material has been due in part to the pristine semiconductor interfaces that can be obtained. As the lattice constants of GaAs and AlGaAs differ by only 0.14%, the heterostructure can be grown via molecular beam epitaxy (MBE) with minimal strain between the layers.

Crucially, the slight difference in the conduction and valence band spacing of the two semiconductors[1] gives rise to a potential junction which forms at their interface. Figure 1.2 schematically depicts a typical GaAs-AlGaAs heterostructure. The layer stack comprises a few hundred microns of GaAs with AlGaAs covering the top. These layers are grown above a superlattice with alternating sheets of GaAs and AlGaAs, creating a series of potential wells in which to trap impurities. In the AlGaAs region, Si atoms are added to provide a surplus of mobile charge carriers needed for conduction. These dopants are set back from the interface by some distance, and pin the Fermi level just below conduction band edge in GaAs. As the Fermi level is continuous, the conduction band dips lower than E_F where the two semiconductor layers meet, and electrons from the valence band can fall into the resultant triangular potential well (see Fig. 1.2 (b)). At sufficiently low temperatures, all of the electrons reside in the lowest energy subband of this well, possessing the same quantum number in the z direction. This quantisation in z is described by the wavefunction $\Psi_n(z)$. The result of this confinement is the formation of a two-dimensional electron gas, or more commonly, 2DEG. The electron wavefunction $\Psi_{k,n}(r)$ can then be written as plane waves in (x, y) in the form

$$\Psi_{k,n}(r) = e^{-i(k_x x + k_y y)}\Psi_n(z) \tag{1.5}$$

for the wave vector $k = (k_x, k_y)$. The eigenenergies, E_n, of the n^{th} subband are given by the parabolic dispersion relation

$$E_n(k) = E_z(n) - \frac{\hbar^2}{2m^*}(k_x^2 + k_y^2) \tag{1.6}$$

where m^* refers to the effective electron mass.

2DEGs forming in GaAs-AlGaAs heterostructures are typically characterised by two key parameters: the electron sheet density and the carrier mobility (see Ref. [10] for detailed coverage). The density n_s, is determined by the dopant concentration and the distance to the dopant setback layer [15]. The mobility μ, is often understood in terms

---

[1] $\sim$ 1.5 eV for GaAs and $\sim$ 2.2 eV for AlAs.

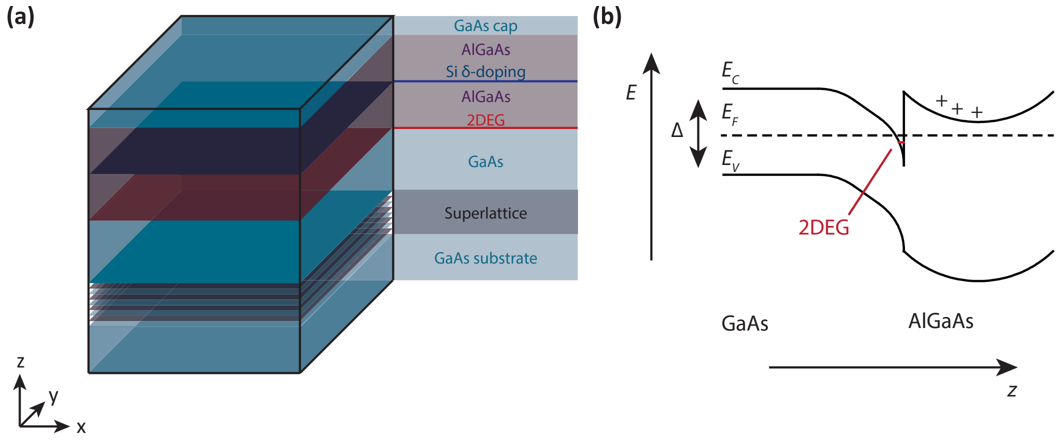

Figure 1.2: GaAs-AlGaAs heterostructure. **(a)** Shows a layer stack comprising epitaxially grown GaAs and AlGaAs on top of a GaAs substrate. A superlattice is used to trap defects, while Si atoms provide an excess of electrons for doping. In **(b)**, at the intersection of the two different semiconductors, a triangular potential well forms due to bending of the conduction band below E_F. At low temperatures when the thermal energy k_BT is less than the energy spacing in the well, all of the electrons will reside in the lowest subband. This collection of mobile charges with the same z quantum number is known as a two-dimensional electron gas, or 2DEG.

of the drift velocity v_d of charged carriers when accelerated under an electric field, E,

$$v_d = \mu E. \tag{1.7}$$

For the purposes of this introduction however, it is more useful to be able to relate μ to physical properties of a material. To do this we start by defining the current density, J and conductivity, σ:

$$J = n_s e v_d, \tag{1.8}$$

$$\sigma = \frac{J}{E} = n_s e \mu. \tag{1.9}$$

From equation 1.9, we can see that higher mobilities and carrier densities lead to increased conductivity and lower sheet resistance. Considering now a particle in steady state motion, the force acting on it will be

$$F = eE = \frac{m^* v_d}{\tau} \tag{1.10}$$

where $\tau = l_e/v_F$ is the momentum relaxation time. Combining the above expressions gives

$$\mu = \frac{e\tau}{m^*}. \tag{1.11}$$

In this way the mobility of a material can be related to the time between electron scattering events, and provides a useful metric by which to compare heterostructures. In GaAs the low effective electron mass of $m^* = 0.067 m_e$, enables high mobility 2DEGs to be created with a strong degree of electrostatic confinement at the heterointerface. This corresponds to a potential well of depth ~ 0.3 eV (see Ref. [16] for a detailed review).

For the heterostructures described in this work[1], n_s is typically of order 2×10^{15} m^{-2}, and $\mu \sim 40$ m^2/V s.

1.2 Quantum dots

1.2.1 Creation

Having introduced some of the relevant characteristics of 2DEGs, we now turn to the interesting quantum systems that can be defined and measured within these environments, including single and double quantum dots, and quantum point contacts. 2DEGs are typically controlled via electrostatic fields set by electrode *gates*. These metallic structures generally comprise Ti/Au stacks ($\sim$ 100 nm thickness) evaporated on the surface of a heterostructure. At sufficiently cold temperatures, the application of negative voltages reverse-biases the gates, allowing the metal to be held at a constant voltage with respect to the 2DEG. The resulting electric fields locally change the electrochemical potential, creating depletion zones and residual puddles of electrons. By making the gate voltages increasingly negative until the size of these charge islands are on the order of the Fermi wavelength, zero-dimensional quantum dots can be formed.

Quantum dots are weakly coupled to their environment and can be filled with one or more electrons (see Fig. 1.3). The quasi-metallic charge reservoirs on either side of these dots (known as *leads*) provide a continuum of states for the shuttling of electrons on and off the central island. In order to access the leads, metallic regions (known as *ohmics*) are annealed at high temperature into the layer stack to make a low-resistance connection with the 2DEG (ideally around $\sim$ 50 Ω)[2]. Setting up a potential difference across two ohmics on opposite sides of a quantum dot allows a current to flow and for the conductance of the dot to be directly measured.

---

[1] See Chapters 3 - 5.

[2] These ohmic contacts are made from a eutectic alloy stack of AuGe, with an atomic weight ratio of 88:12, or 2:1 layer height when evaporating.

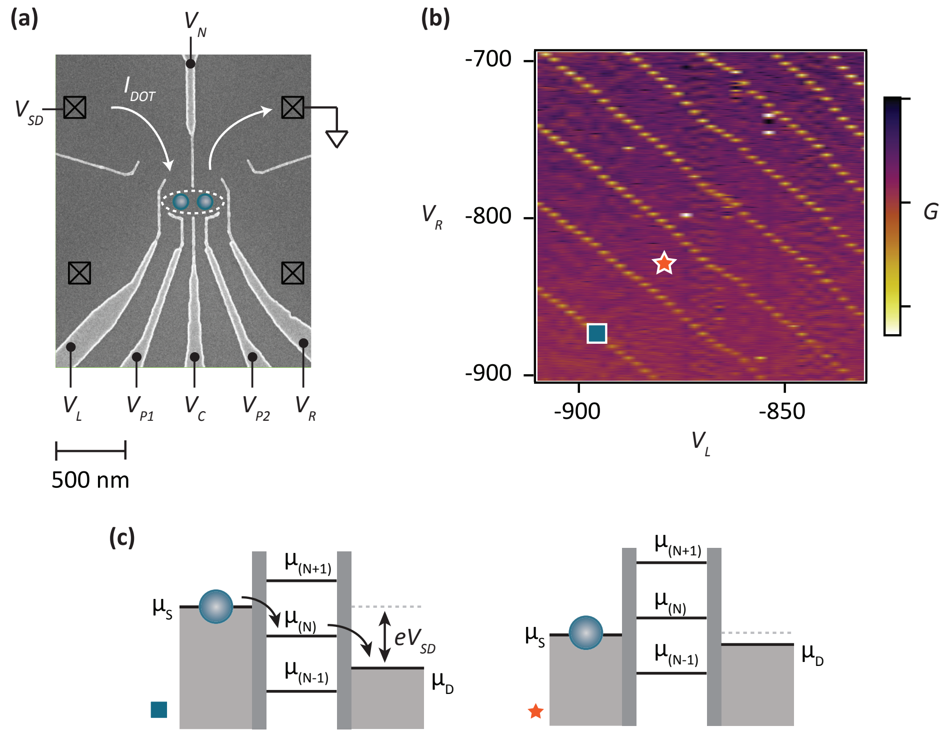

Figure 1.3: Single quantum dot. (a,b) Electron micrograph of a quantum dot gate structure measured in the Quantum Nanoscience Lab at the University of Sydney. The device in (a) can be configured as a single (white dotted region) or double (blue circles) quantum dot via the application of negative voltages on the gate electrodes (light grey patterns). Squares with crosses represent ohmic contacts, which are annealed into the heterostructure to make contact with the 2DEG. In (b), conductance, G, through a single quantum dot is measured (colour axis) while sweeping the voltages on the left and right wall gates (V_L and V_R). Bright yellow stripes indicate charge transitions. **(c)** shows a cartoon illustrating transport in a single quantum dot for two different regimes. On the left, an energy level of the dot (denoted μ_N) lies within the bias window of the source and drain reservoirs (μ_S and μ_D respectively), allowing an electron to tunnel on and off the central island. On the right, tunnelling is not energetically allowed and the occupation of the dot remains constant. (c) adapted from Ref. [14].

1.2.2 Artificial atoms

The electrostatic confining potential that houses a quantum dot can support a number of spin-degenerate energy levels. It is for this reason that quantum dots are often referred to as *artificial atoms*, as their well-defined energy states can be compared to atomic orbitals [17]. The allowable energy states can be understood within the constant interaction model, where the relationship between electrons in a dot and its electrostatic environment is characterised by a total capacitance term, C [14]. The energy of the dot $U(N)$ in its ground state with N electrons is given by

$$U(N) = \frac{(-|e|(N - N_0) + \sum_i C_i V_i)^2}{2C} + \sum_j^N E_j \tag{1.12}$$

where E_j is a summation over the single particle energy levels up to N, and C_i and V_i refer to the capacitance and voltage contributions of the nearby structures (including the source and drain leads, and the electrode gates). The electrochemical potential, μ, on the island is then defined as

$$\mu \equiv U(N) - U(N-1). \tag{1.13}$$

The additional energy associated with bringing an extra electron onto the dot is

$$E_{add}(N) = \mu(N+1) - \mu(N) = E_C + \Delta E \tag{1.14}$$

where $E_C = e^2/C$ is the charging energy (similar to the ionisation energy for an atom) and ΔE gives the level spacing [14].

For small sized dots the self capacitance term, C, is small and so the energy required to increase the electron occupation of the dot becomes large. Considering the dot and its environment as the plates of a capacitor, this value of C also sets the time taken to charge up an island with an extra electron. This process occurs with a time constant of $\Delta t = R_t C$ where R_t is the tunnelling resistance. Invoking the Heisenberg uncertainty relation in the form $\Delta E_c \Delta t > h$, it is therefore necessary that

$$R_t > \frac{h}{2e^2} \tag{1.15}$$

in order to resolve E_C (where the factor of 1/2 accounts for the degenerate spin up and spin down states). This rather simple, intuitive derivation gives rise to the conductance quantum

$$G_0 = \frac{2e^2}{h}, \tag{1.16}$$

and also sets the condition for observing single electron tunnelling events through the energy levels of a quantum dot [18]. A second key requirement is that the thermal energy of the electrons must be sufficiently low such that they cannot be easily excited on or off the dot, i.e.

$$k_B T < \frac{e^2}{C} \tag{1.17}$$

where k_B is Boltzmann's constant.

1.2.3 Transport

When the electrochemical potential of a quantum dot lies within the energy states or *bias window* set by the reservoirs, $\mu_s \geq \mu(N) \geq \mu_D$, a flow of current proportional to the source-drain voltage is observed, $\mu_s - \mu_d = -|e|V_{SD}$ (blue square in Figure 1.3 (c)) [14]. This is visible as peaks in the conductance. In this way, varying the source-drain bias can be used to effect transport through the dot. Equivalently, the potential level of the island itself can be tuned via the capacitive coupling of a *plunger* gate (V_{P1} or V_{P2} in Fig. 1.3 (a)). Both scenarios can be used to induce charge tunnelling events, until the energy needed to fill the dot with one extra electron is greater than the chemical potential at the leads. In this situation the energy level of the dot lies outside the bias window, and tunnelling is barred. This is known as Coulomb blockade, and is indicated by the orange star in Fig. 1.3 (b) and (c).

1.3 Double quantum dots

1.3.1 Charge stability diagram

A double quantum dot system is formed when two individual collections of charge are sufficiently coupled that the state of one dot affects the other (see review article in Ref. [14]). For the purposes of this work, we are most interested in the few-electron regime where almost all of the charge is emptied from the double potential well. In this situation the number of electrons on the left and right islands are denoted as (L,R). For example, a two-electron charge configuration can be (0,2), (2,0) or (1,1).

A map of these charge combinations can be created using the electrostatic handles V_R and V_L for the right and left wall gate voltages respectively. A simple charge stability diagram is shown in Fig. 1.4 (a). Experimentally, the capacitance between the electrode gates and dots leads to a cross coupling and tilting of the charge stability diagram. This is illustrated in Fig. 1.4 (b). The corners of the hexagonal shaped regions indicate *triple points* where tunnelling can occur in succession from one lead to another via the energy states of the two dots.

As an example of a charge transport process, we refer to Fig 1.4 (b) and begin in the middle of the (0,1) region. Varying V_L leads to the addition an electron in the left dot by moving horizontally across into (1,1). Similarly, shifting vertically upwards by changing V_R opens up the (1,2) electron configuration. If a combination of the right and left gate wall voltages are employed to move perpendicular to the charge transition from the (0,1) into the (1,0) state, the potentials of the two dots can be changed relative to each other while the average remains constant. This line is referred to as the detuning axis, ϵ.

The energy spectrum of the (0,2) and (1,1) charge states is shown in Fig. 1.4 (c) as a function of ϵ. If the dots are weakly coupled by the parameter t_c, the degeneracy around $\epsilon = 0$ is lifted and an avoided crossing with gap equal to $2t_c$ forms.

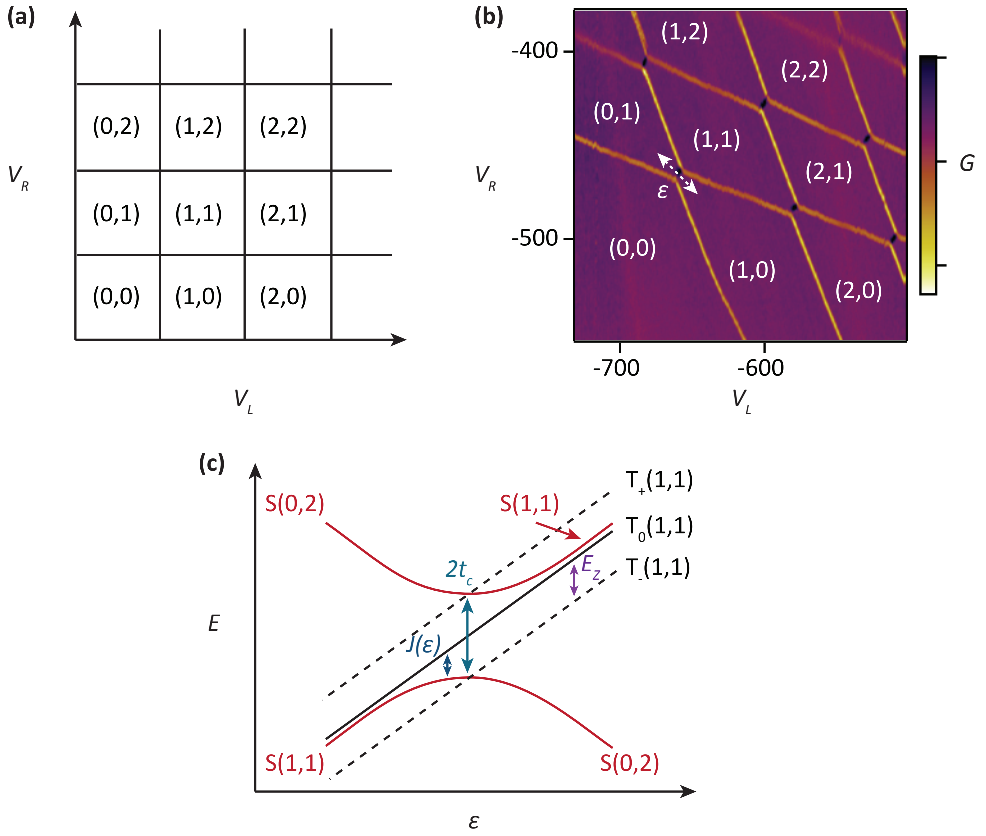

Figure 1.4: Double quantum dot. Charge stability diagrams for a double quantum dot in the few-electron regime without, **(a)**, and with, **(b)**, capacitive coupling. Charge occupancy of the left and right dots is denoted as (L,R). Yellow lines in (b) indicate tunnelling to the leads, whereas black lines correspond to interdot charge transitions. The detuning axis ϵ is denoted by the white dotted line. The energy level diagram for a double quantum dot as a function of ϵ is shown in **(c)**, taking into account the spin singlet and triplet states for the (0,2) and (1,1) charge configurations. The application of a small magnetic field splits the T_- and T_+ states by the Zeeman energy E_Z. (a) and (c) are adapted from Ref. [14].

1.3.2 Including spin

Introducing electron spin into this picture, conservation laws dictate that certain transitions are more energetically favourable than others. For clarity, the up and down spin states are represented as ↑ and ↓. For the case of two-electron double dot configurations, the electron spins give rise to the singlet and triplet energy states,

$$|S\rangle = \frac{1}{\sqrt{2}}(\uparrow\downarrow - \downarrow\uparrow) \tag{1.18}$$

$$|T_0\rangle = \frac{1}{\sqrt{2}}(\uparrow\downarrow + \downarrow\uparrow) \tag{1.19}$$

A small in-plane magnetic field ($\sim$ 100 mT) can split the triplet states by the Zeeman energy $E_Z = g\mu_b B$ where μ_b is the Bohr magneton $\hbar e/2m \approx 58$ μeV/T for a free electron, and g=-0.44 in GaAs[1] (Fig. 1.4 (c)). This gives the $T_{\text{-}}+$ and $T_{\text{-}}-$ components

$$|T_+\rangle = \uparrow\uparrow \tag{1.20}$$

$$|T_-\rangle = \downarrow\downarrow \tag{1.21}$$

The overall two-particle wavefunction of the electrons is antisymmetric due to the Pauli exclusion principle. This means that for a triplet state with two electrons residing in one dot, one of the electrons must occupy a higher orbital energy state. This requirement gives rise to a difference in energy between the (0,2)S singlet and (0,2)T_0 triplet state, known as the exchange energy, J (Fig. 1.4 (c)). Furthermore, as tunnelling events are spin conserving, transport can be blocked when trying to force two electrons in a spatially separated triplet state into a single dot. For example, consider

---

[1] The Landé g-factor for free electrons is 2, but is affected by the spin-orbit coupling in solid-state materials

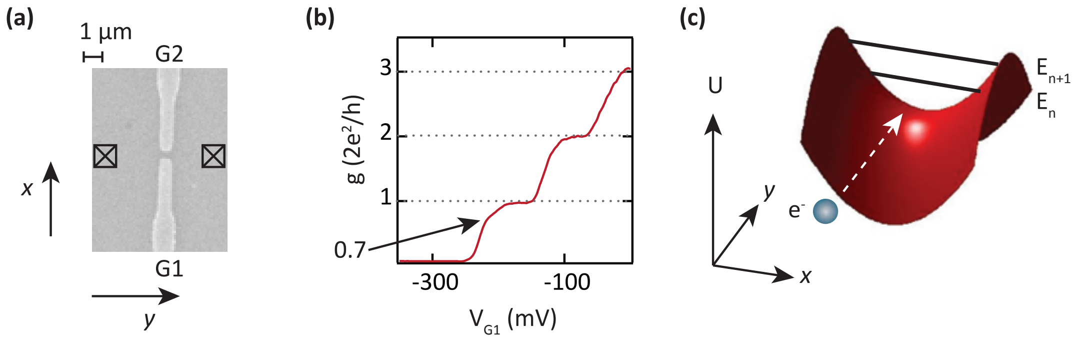

Figure 1.5: Quantum point contact. **(a)** Shows a electron micrograph of a QPC split-gate geometry. In **(b)**, the conductance through the channel is measured as a function of gate voltage V_{G1}, and shows a series of steps quantised in the units of $2e^2/h$. **(c)** depicts a cartoon of a QPC saddle point potential, along with equally-spaced energy sub-bands denoted E_n and E_{n+1}. See Ref. [19].

transport from $(0,1) \rightarrow (1,1) \rightarrow (0,2) \rightarrow (0,1)$. For the transition from the (1,1) to the (0,2) state, either the (1,1) singlet or triplet can be formed. If it is the latter, then the antisymmetric orbital ground state of the triplet will prohibit the system from entering into the (0,2) configuration. This situation gives rise to spin-blockade.

1.4 Quantum Point Contacts

1.4.1 Transport

In the few electron regime where tunnel rates to the reservoirs are low (less than a few MHz), directly measuring the occupancy of a quantum dot or double dot via transport is no longer feasible. Nearby charge sensors are commonly used for this purpose, and are designed to be capacitively rather than tunnel-coupled to a quantum dot. The quantum point contact or QPC is one such example, comprising a narrow, quasi one-dimensional channel of 2DEG that is sensitive to changes in the local electrostatic environment. However, before turning to the use of QPCs as charge sensors, we first provide a brief overview of the physics of these channels. As we shall see, QPCs are rich systems in their own right in which to study the fundamentals of quantum transport.

The defining feature of a QPC is its width, w (along x) which must be of order the Fermi wavelength (typically $\sim$ 50 nm in our systems). This is controlled via static voltages on surface gates ($G1$ and $G2$ in Fig. 1.5 (a)). The potential barriers associated with these gates serve to laterally confine the 2DEG channel on either side, and can be increased to reduce the width of a QPC continuously. This picture of a QPC as a narrow channel which is adiabatically connected to two much larger reservoirs can be modelled as an effective saddle point potential [20]. As V_{G1} is made more negative, the constriction is narrowed while the barrier height is increased. This corresponds to lifting the seat of the QPC saddle, as shown in Fig. 1.5 (c). Crucially, confinement in x leads to the formation of a parabolic potential $U(x)$ where a series of equally spaced energy sub-bands exist. Transport along y from reservoir 1 to reservoir 2 (potentials μ_1 and μ_2) can only occur through these modes. As the QPC constricts further, the sub-bands move upwards, depopulating once they cross the Fermi energy E_F. This results in a stepwise decrease in the channel conductance as higher modes empty, indicated in Fig. 1.5 (b). This integer quantisation was first discovered experimentally by groups in Delft [21], and Cambridge [22] in 1988. For detailed discussions, see Refs. [18, 23].

Following the derivation in Ref. [19], the system can be described using the Hamiltonian

$$H = \frac{{p_x}^2}{2m^*} + eV(x) + \frac{{p_y}^2}{2m^*} \tag{1.22}$$

which considers just the transport occurring at the effective bottleneck of the QPC [19, 24]. The solutions take the form of energy eigenvalues for a harmonic oscillator

$$E_n = (n - \frac{1}{2})\hbar\omega_0 + \frac{\hbar^2 {k_y}^2}{2m^*} \tag{1.23}$$

where $\hbar\omega_0$ is the energy spacing of the n k_y states, which are free to move in y but are confined along x. When a potential difference is applied across the QPC, $eV = \mu_1 - \mu_2$, the reservoirs μ_1 and μ_2 are no longer equal and a current can flow. The full expression is obtained for I by multiplying the current density $j_x = nev$ by the cross-sectional area and the transmission coefficient $T_n(E)$ of the n^{th} sub-band to obtain

$$I = e\sum_{n=1}^{N}\int_{\mu_1}^{\mu_2} dE\frac{1}{2}\frac{dN}{dE}v_n(E)T_n(E) \tag{1.24}$$

Multiplying the 1D density of states by the velocity gives

$$\frac{dN}{dE}v_n(E) = \frac{2}{\pi}{\frac{dE_n}{dk_y}}^{-1}\frac{1}{\hbar}\frac{dE_n}{dk_y} = \frac{4}{h} \tag{1.25}$$

Therefore, as the energy terms in the density of states and the group velocity cancel, the resultant current carried by each subband is independent of energy. As $G = I/V$, it follows that

$$G = \frac{2e^2}{h}\sum_{n=1}^{N}T_n(E_F). \tag{1.26}$$

This is the well-known Landauer formula [25]. In the limit of no backscattering, the transmission sum $\sum_{n=1}^{N}T_n(E_F)$ is just equal to N and so

$$G_0 = \frac{2e^2}{h}N. \tag{1.27}$$

This quantisation of the conductance corresponds to full transmission of N individual spin-degenerate modes through the QPC.

A typical pinch-off profile for a QPC is shown in Fig. 1.5. Flat steps occurring at multiples of $G = 2e^2/h$ indicate integer quantisation of the conductance, shown for the lowest three modes. Below the last plateau however, an additional inflection is observed to occur around $G = 0.7G_0$. This anomalous feature, and indeed the set of phenomena that surround it, cannot be described within a single-particle framework. A substantial body of literature has attempted to account for this feature, drawing on Kondo effects, spontaneous spin polarisation and Wigner crystallisation [26], however consensus is still lacking as to its origin.

1.4.2 dc and rf charge sensing

Finally, tying together quantum dots and QPCs, we briefly mention the use of 1D channels as charge sensors. When a QPC is placed near to a quantum dot, small changes in the charge occupancy of the island can modify the potential of the constriction. As the conductance through a QPC is strongly non-linear with respect to gate voltage, maximal sensitivity is obtained where dG/dV is large. This is illustrated in Fig. 1.5, where the working point is on the riser just below the last $2e^2/h$ plateau. Operating in this regime also serves to minimise charge screening effects that can become significant when the channel is more open.

As the transmission coefficient of a QPC, $T_n(E)$ is dependant on the charge state of a nearby dot, QPCs can also be used to perform spin readout via a spin-to-charge conversion. We consider the two-electron spin blockade sequence described in §1.3.2: if a spin triplet state is formed, the conductance through the QPC will remain unchanged. However, if a singlet is formed, tunnelling is allowed into the (0,2) charge configuration and eventually off the dot. The result of this is a decrease in $T_n(E)$ of the QPC.

Fast, radio-frequency (rf) readout of quantum dots can be performed by making use of a QPC embedded in a resonant circuit. This technique was first demonstrated in Ref. [27] via the addition of a copper wire-wound inductor in series with a 1D constriction. On resonance where $\omega = 1/\sqrt{LC}$, the inductance L cancels the parasitic capacitance (around $C = 0.3$ pF) of the circuit and acts to effectively transform the high impedance of the sensing channel (of order the resistance quantum, $1/2 \times 25\ 813\ \Omega$) down to the $50\ \Omega$ characteristic impedance of the rf transmission line. As with the case of dc charge sensing, the impedance of the QPC constriction is affected by charge movement on the island, such that variations in the amplitude and phase of the resonator can be interpreted as changes in the dot occupation.

2

The quantum Hall effect

This Chapter focuses on the quantum Hall family of effects, where the application of a magnetic field normal to a plane of electrons can lead to the emergence of entirely new behaviour. Here we briefly introduce some of the physics underlying this phenomena from the viewpoint of both theory and experiments.

Within quantum point contacts (QPCs), spin-degenerate transport quantised in the fundamental units of $2e^2/h$ can arise from purely electrostatic confinement [21, 22]. The observation of quantised conductance through these one-dimensional channels was foreshadowed by the earlier discovery of the quantum Hall effect in a two-dimensional electron gas (2DEG) in 1980 [4]. In these systems, it was found that the application of a large perpendicular magnetic field, B, could constrain electron motion and lead to the presence of conductive edges in units of

$$\frac{e^2}{h} = 1/(25,812.807572\Omega). \tag{2.1}$$

The extreme precision to which this value can be measured has lead to its adoption as a metrological standard, related to the impedance of free space, Z, and the fine structure constant, α[1].

In this Chapter we first introduce the integer quantum Hall effect (IQHE), following both a semi-classical and quantum description. We then extend this discussion to the fractional quantum Hall regime, wherein strongly interacting systems of electrons rearrange to form a Fermi sea of weakly coupled composite particles. Closely related is the quantum anomalous Hall effect, where robust edge states at a sample boundary can exist in the absence of an external magnetic field. This phenomena is reviewed briefly for the case of thin-film 3D topological insulators with ferromagnetic exchange. Finally attention is turned to edge magnetoplasmons (EMPs)- the dynamic manifestation of quantum Hall edges.

2.1 The integer quantum Hall effect

2.1.1 Semi-classical description

A standard dc Hall bar is shown in Fig. 2.1, comprising a GaAs-AlGaAs mesa in the xy plane with 6 ohmic contacts. The source and drain ohmics at either end of the bar facilitate the flow of current, I, between them. Narrow arms at the sides of the mesa are connected to high-impedance voltage probes. In this way, the potential difference along

---

[1] The fine structure constant $\alpha = 2\pi e^2/hc \approxeq 1/137$ is a fundamental quantity in electrodynamics proportional to the ratio of the electric and magnetic flux of an electron

the x or y direction (V_{xx} and V_{xy} respectively) can be measured. The longitudinal and transverse resistances, R_{xx} and R_{xy}, are defined by the ratio of the voltage difference across the terminals, to the current through the device, $R_{xx} = V_{xx}/I$, $R_{xy} = V_{xy}/I$.

As we saw in the previous chapter, when $B = 0$, the application of an electric field, E_x, across a sample leads to the acceleration of charge carriers with a velocity, v_x, proportional to the mobility, μ,

$$v_x = -\mu E_x = \frac{-eE_x\tau}{m*}. \tag{2.2}$$

The momentum scattering time is given by τ while m^* is the effective electron mass. When $B > 0$, the Lorentz force $F = ev \times B$ causes electrons to be deflected across the xy plane. The subsequent charge build-up gives rise to an electric field in the y direction, $E_y = -v \times B$, perpendicular to the direction of current. The equation of motion for the system then becomes

$$m^* \frac{dv}{dt} = -e(E + v \times B). \tag{2.3}$$

The current density is defined as

$$J = -n_s ev = \sigma E \tag{2.4}$$

where n_s is the electron sheet density and σ represents the conductivity tensor. The resistivity, ρ is the matrix inverse of σ.

Along one side of the sample, the longitudinal resistivity, ρ_{xx}, is found by combining expressions 2.2 and 2.4:

$$\rho_{xx} = \frac{E_x}{J_x} = \frac{m^*}{n_s e^2 \tau}. \tag{2.5}$$

The transverse resistivity, ρ_{xy}, can be obtained by considering that in the rest frame of

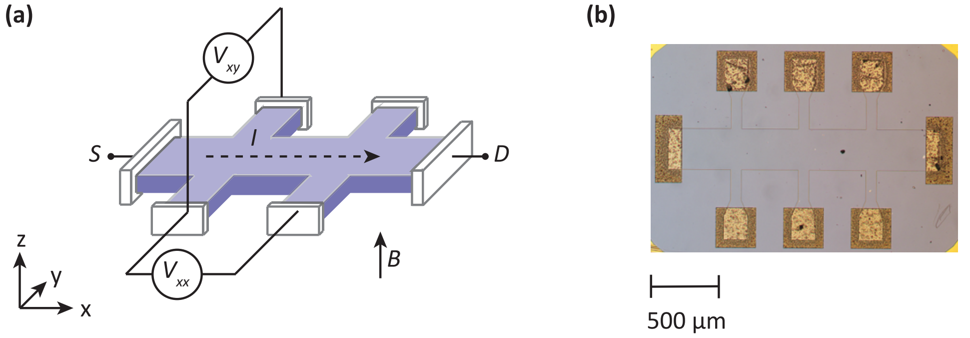

Figure 2.1: Hall bar. **(a)** Illustration of a typical Hall bar setup. Current is measured from left to right via the source and drain contacts (S, D). The voltage drop along the direction of current (V_{xx}) and orthogonal to it (V_{xy}) are measured as shown. A magnetic field B is applied normal to the plane of the sample, in the z direction. **(b)** Photograph of a Hall bar device fabricated and measured within the QNL. Gold regions depict annealed ohmic contacts.

the electron, the Lorentz force must cancel E_y such that current flows solely along x. Under these conditions we find

$$\rho_{xy} = -\rho_{yx} = \frac{E_y}{J_x} = \frac{B}{n_s e}. \tag{2.6}$$

Owing to the curved motion, electrons in the bulk of the sample are confined to equipotential orbits around localized hills or valleys arising from disorder. The cyclotron frequency of these orbits is given by

$$\omega_c = \frac{eB}{m^*}, \tag{2.7}$$

which is independent of the individual particle velocity. For a finite sized sample, the physical sides impose boundary conditions on the orbits, forcing the electrons near the edge to reflect and skip around the mesa. Charges along the perimeter that are scattered by impurities can only move backward by the length of the cyclotron radius, before continuing along with the edge. In this way, backscattering in the opposite direction is suppressed. These directional transport channels are known as edge states.

2.1.2 Quantum treatment

In order to understand the origin of quantised Hall conductance at high magnetic fields, we need to move to a quantum mechanical picture (see Refs. [10, 28]). For the case of a uniform field B along the z direction, the Hamiltonian describing an electron in a 2D plane is modified by the vector potential A, and can be written as

$$H = \frac{1}{2m^*}(p + eA)^2 + V(z) \tag{2.8}$$

where $p = (p_x, p_y)$ denotes the momentum and $V(z)$ is the confining potential in the z direction. By choosing the vector potential in the Landau gauge as

$$A = B(-y, 0, 0) = -By\hat{x}, \tag{2.9}$$

and considering only in-plane contributions, we have

$$H_{xy} = \frac{1}{2m^*}(p_x + eBy)^2 + \frac{1}{2m^*}{p_y}^2. \tag{2.10}$$

This Hamiltonian is translationally invariant in the x direction and can be rewritten as

$$H_{xy} = \frac{p_y^2}{2m^*} + \frac{1}{2}m^*\omega_c^2(y - y_0)^2 \tag{2.11}$$

using the substitutions $\omega_c = eB/m^*$, $y_0 = l^2 p_x/\hbar$ and the magnetic length $l = \sqrt{\hbar/eB}$. This corresponds to the equation of a harmonic oscillator centred around y_0, whose energy levels are given by

$$E_n = \hbar\omega_c(n + \frac{1}{2}). \tag{2.12}$$

These states can be understood as Landau levels (LLs), which are quantised δ-function energy bands in the density of states (DOS) separated by an energy gap of $\hbar\omega_c$. Including the Zeeman effect, expression 2.12 then becomes

$$E_n = \hbar\omega_c(n + \frac{1}{2}) \pm \frac{1}{2}g^*\mu_b B \tag{2.13}$$

where g^* is the effective Lande g factor in the host medium, and μ_B is the value of the Bohr magneton. Each of these levels is degenerate, with the number of allowed energy states per unit area n_B proportional to the magnetic field, such that

$$n_B = \frac{B}{\Phi} \tag{2.14}$$

where Φ is the flux quantum equal to h/e. We can now introduce an important parameter used to describe quantum Hall systems, ν. This term is defined as the number of electrons per magnetic flux quanta penetrating the sample, and can be calculated by the ratio of the 2D electron sheet density n_s to the states (or flux) density n_B,

$$\nu = \frac{n_s}{B/\Phi} = \frac{n_s h}{eB}. \tag{2.15}$$

At higher magnetic fields, each Landau level can take on more electrons, and so the number of filled LLs, or the *filling factor*, ν, is reduced.

2.2 Effects at the edge

The filling factor of a system can also be equated to the total number of edge states. At the physical boundaries of a sample the confining potential increases, causing the LLs to adiabatically rise upwards in energy at the sides (see Refs. [9, 10, 28, 29]). At the regions where each LL intersects E_F, free states become available for electrons to scatter into. This gives rise to conductive 1D channels forming along the edge. These edge states are *chiral*, and propagate in a direction determined by the applied magnetic field. The physical separation between the forward and backward moving edges at either side of a sample means that there are no free states in the opposite direction for electrons to scatter into, leading to dissipationless transport. The total current in such

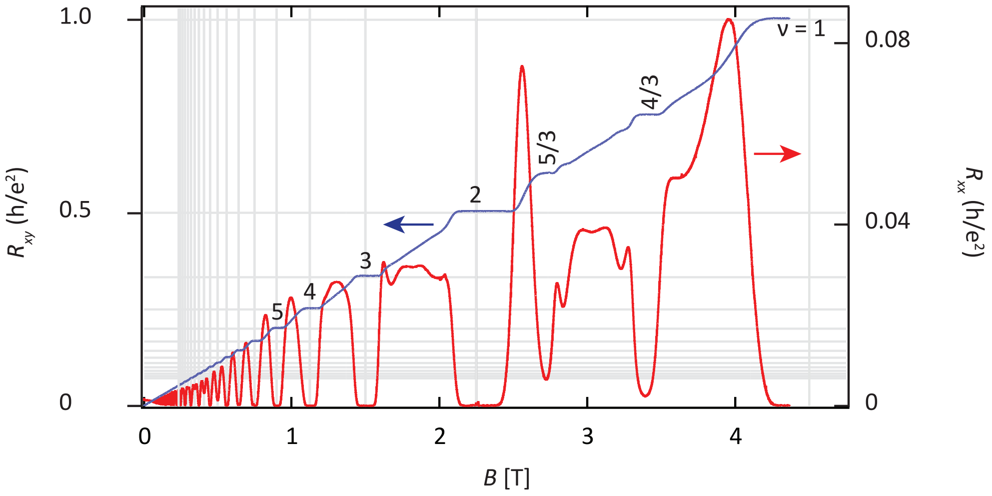

Figure 2.2: Transport in the integer quantum Hall effect. Longitudinal (red) and transverse (blue) resistances in units of h/e^2 measured on a GaAs-AlGaAs high mobility Hall bar in the QNL. Data taken at a lattice temperature of 20 mK. Horizontal grey lines indicate integer multiples of the Hall conductance. Vertical lines indicate magnetic fields corresponding to integer filling factors.

a system is found by integrating over the group velocity,

$$v_k = \frac{1}{\hbar}\frac{\partial_k E}{\partial k}, \tag{2.16}$$

multiplied by the probability that a state n is occupied (ρ_n):

$$I = \frac{-eL_y}{2\pi}\int_{-\infty}^{\infty} dk \frac{1}{\hbar}\frac{\partial E}{\partial_k}\frac{\rho_n}{L_y} = \frac{-e}{h}\int_{\mu_1}^{\mu_2} dE = \nu V_H \frac{e^2}{h}. \tag{2.17}$$

Here the prefactor ν indicates that each occupied LL contributes one edge state of conductance e^2/h to the total current [30].

A typical magnetotransport measurement is shown in Fig. 2.2. For a constant value of ν where R_{xy} is quantised and R_{xx} is vanishingly small, the situation can be described by Fig. 2.3 (indicated by red dotted line in inset). The (ordinarily constant) 2D density of states is split into a series of strips which, in the presence of disorder, broaden into narrow bands of allowable states (b). In the case of Zeeman splitting, each band separates into spin-polarised levels with spacing equal to $g_s\mu_b B$. At integer filling factors, the Fermi energy lies in the gap between Landau Levels and electrons in the bulk encircle equipotential regions in closed cyclotron orbits (c). These give rise to localised states that exist both slightly above and below E_N (grey regions in (b)), but do not contribute to transport. As a result, the system is gapped and R_{xx} tends to zero while R_{xy} remains constant despite increasing B.

At the edges of the sample, an increase in the potential leads to a flow of current where each LL meets E_F (a). In realistic systems however, the electrons at the edge will rearrange to screen interactions as the potential rises. In this self-consistent picture [31] each LL is described as a compressible strip with finite width separated by incompressible regions (d). In these incompressible regions there are no partially filled states at the Fermi energy, and the density n is constant (e).

When the Fermi level moves into the bulk Landau levels, the situation is illustrated in Fig. 2.4. As the magnetic field is increased, the degeneracy of each LL also increases

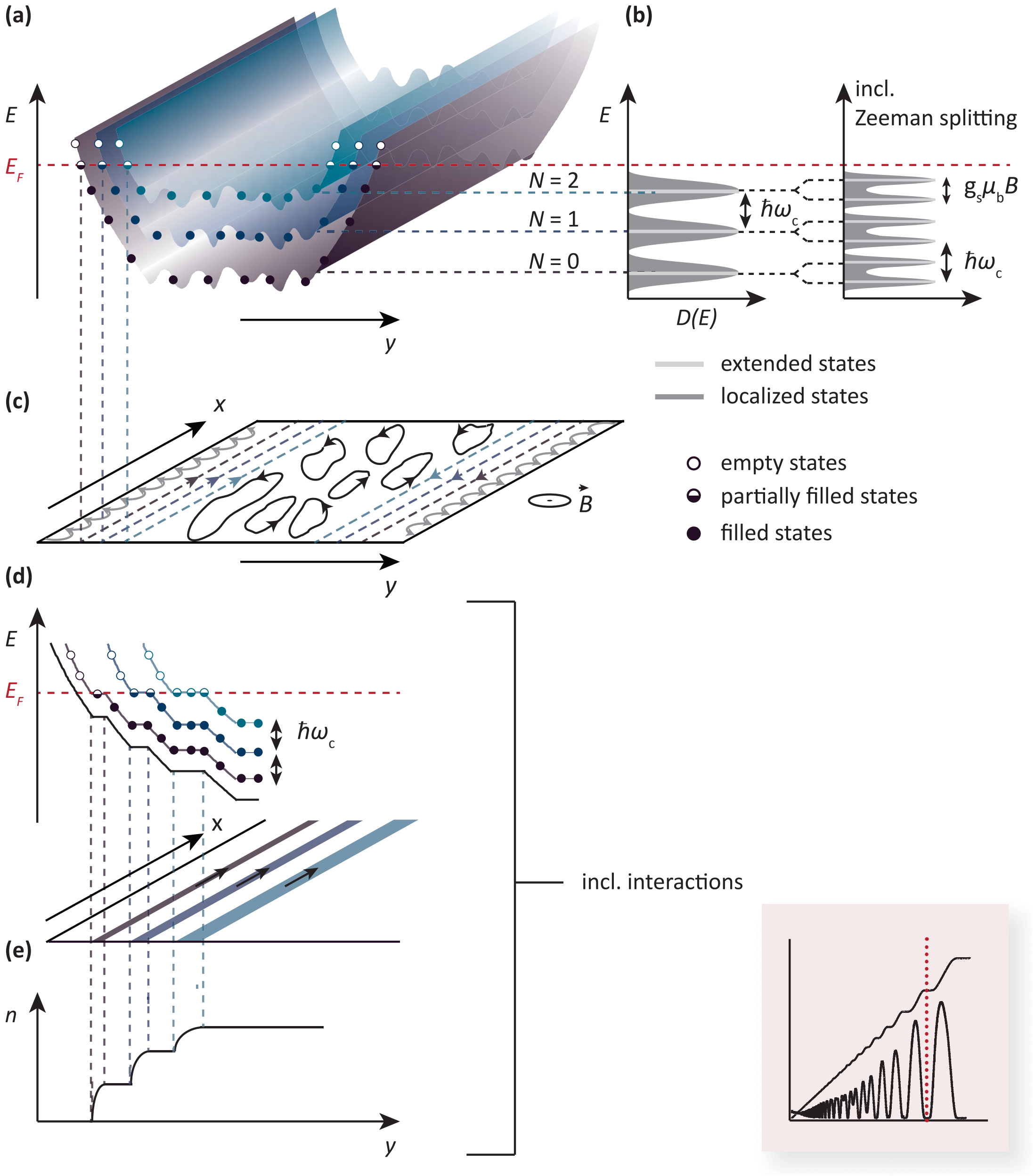

Figure 2.3: IQHE at a constant filling factor. Corresponding magnetotransport illustration is shown in inset, pink box. **(a)** Energy spectrum of Landau levels for a 2D sample in the xy plane. At the edges of the sample, an increase in the confining potential causes the LLs to rise upwards in energy, intersecting E_F and leading to 1D conducting edges. **(b)** shows the splitting of the 2D density of states by $\hbar\omega_c$ in the presence of a magnetic field (light grey strips). Disorder in the sample acts to broaden the strips into narrow bands. In the case of a strong B field, the bands are split by the Zeeman energy, $g_s\mu_bB$. When E_F lies in between LLs, the electrons in the bulk are localised in cyclotron orbits around potential hills and valleys and do not contribute to transport **(c)**. This situation can also be described within a self-consistent model, where each edge state corresponds to compressible strip with varying density **(d,e)**.

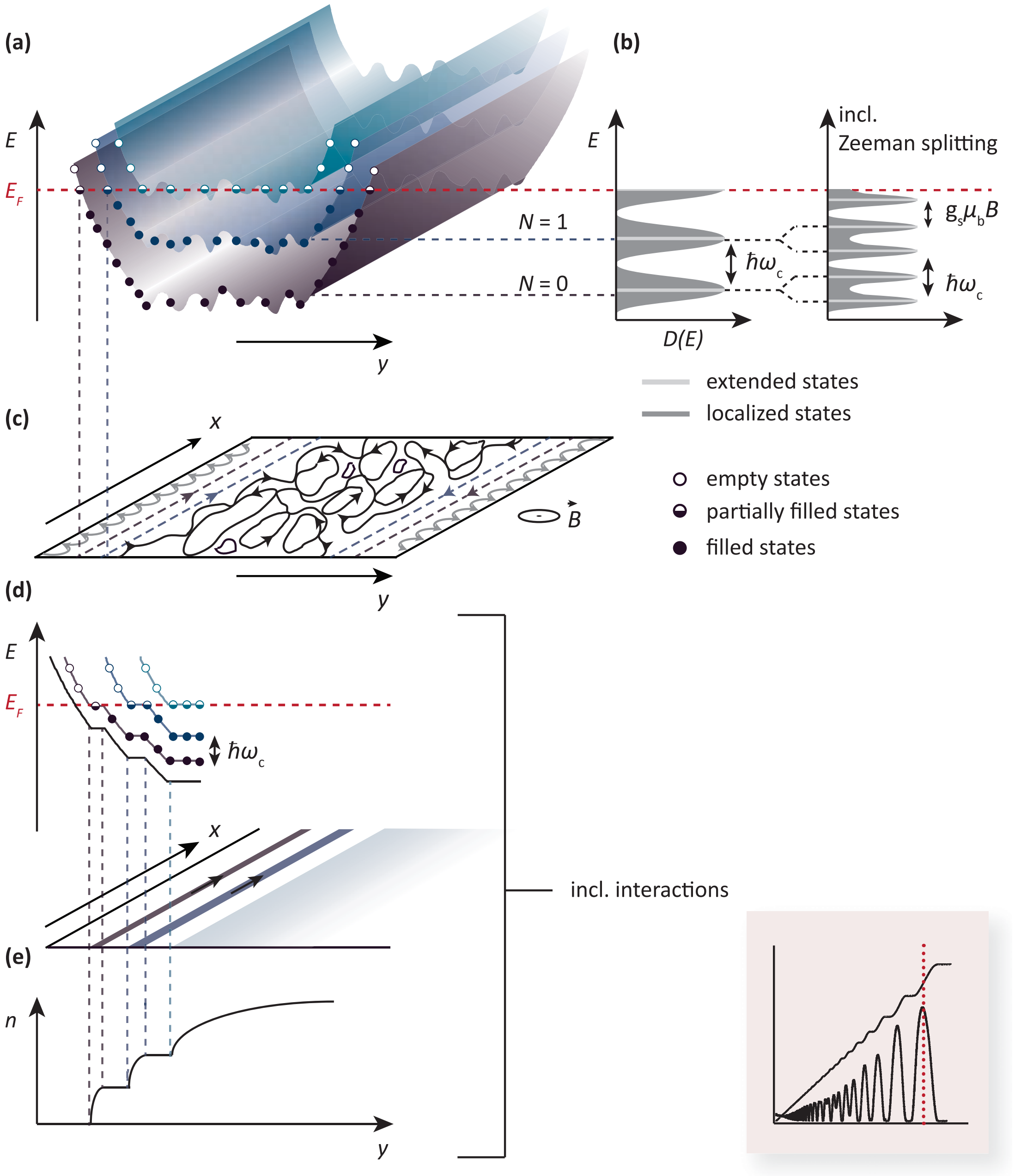

Figure 2.4: IQHE between filling factors. Corresponding magnetotransport illustration is shown in inset, pink box. As the magnetic field is increased, the degeneracy of each LL also increases and higher levels depopulate **(a)**. When E_F lies within the extended states (dark grey regions in **(b)**), transport can occur across the sample, leading to finite transverse resistance **(c)**. At this point, the sample bulk can be represented by a compressible region (d,e) where electron scattering occurs and changes in the density n can be supported.

and the gap between neighbouring states widens. The LLs corresponding to higher filling factors depopulate sequentially as more free states become available in the lower levels. When the Fermi energy lies at a maximum in the density of states (Fig. 2.4), transport can occur across the sample via extended states which connect the two sides (c). The bulk of the sample is then compressible (d,e). Owing to this path between opposite moving edges, backscattering is no longer suppressed and the longitudinal resistance increases rapidly.

2.3 The fractional quantum Hall effect

2.3.1 Laughlin wavefunction

While the IQHE can be described by a sea of non-interacting electrons, the fractional quantum Hall effect (FQHE) is a key example of a strongly interacting system where Coulomb effects play a central role. Fractional quantum Hall states are denoted by the filling factors $\nu = p/q$ where p and q are both integers. As with the IQHE, these values of ν correspond to energetically gapped states, and are characterised in transport measurements by flat plateaus in ρ_{xy} and minima in ρ_{xx}. In the case of the FQHE however, this energy gap (where $\Delta_{p/q} << \hbar\omega_c$) is understood to arise from highly correlated electron behaviour [10]. The fractional filling factors 4/3 and 5/3 are indicated in Fig. 2.2.

The first experimental observations of non-integer plateaus in the Hall conductance came from Horst Störmer and Daniel Tsui [5], who discovered an entirely new set of features existing in very high mobility GaAs-AlGaAs heterostructures in the presence of large magnetic fields. A theoretical model was later proposed by Robert Laughlin in 1983, who postulated that under certain conditions, fractional charge carriers could condense into a kind of collective ground state [32]. Taking the dominant Coloumb interactions into account, Laughlin outlined a many-body ground state wavefunction for odd-denominator filling factors $\nu = 1/m$

$$\Phi = \prod_{i<j}^{N} (z_i - z_j)^m e^{\frac{-1}{4l^2} \sum_{j=1}^{N} |z_j|^2} \tag{2.18}$$

where l is the magnetic length and z_i and z_j specifies the positions of the ith and jth particles up to a total of N. For such filling factors, all of the electrons will be in the lowest Landau level and possess the same kinetic energy. This wavefunction scales with the distance between the particles $(z_j - z_i)$, such that interactions are minimised (see Ref. [10]).

2.3.2 Composite fermions

In a more general theory proposed by Jain (see a description in Ref. [28]) these fractional excitations are described in terms of composite fermions (CFs), whose behaviour in an effective magnetic field can be likened to that of a gas of electrons in the integer quantum Hall effect. Intuitively we can therefore think of the role of CFs as equivalent to the weakly interacting electrons in the IQHE. Crucial to this model is the formation of magnetic flux vortices (or regions of zero charge density) that can exist under strong perpendicular magnetic fields. CFs arise from the pairing of electrons with these magnetic flux quanta, in order to screen Coulomb interactions and reduce the energy of the many-body system. A fractional quantum Hall state with $\nu = 1/m$ can then equivalently be described as a single quasiparticle excitation with effective charge $e^* = e/m$.

We consider the case of a composite fermion formed from an electron binding with an even number, $2p$, of localised vortices (see Refs. [9, 10]). The magnetic field experienced by the CF will be reduced by an amount proportional to the total flux quanta, given by $2p\Phi n_s$. The effective magnetic field is therefore

$$B^* = B - 2p\Phi n_s. \tag{2.19}$$

Recalling that $\nu = n_s\Phi/B$, we can see that B^* goes to zero for $\nu = 1/2p$ i.e. in the case fractions with an even denominator. This corresponds to a Fermi liquid, akin to in the IQHE. Through this argument we can also see that, as the interaction energy in the system is $\propto \sqrt{B}$, the transition from $B \to B^*$ leads to only weak interactions between the CFs. Using the above notation, each filling factor in the FQHE effect can be denoted by energy levels split by $\hbar\omega_c^*$ and written as

$$\nu^* = \frac{nh}{eB^*}, \tag{2.20}$$

while fractional and integer filling factors can be related using the general form:

$$\nu = \frac{\nu^*}{2p\nu^* \pm 1}. \tag{2.21}$$

2.4 The quantum anomalous Hall effect

Having introduced the IQHE and FQHE, we now touch on the concept of topology before turning to the quantum anomalous Hall effect (QAHE). Topology is a branch of mathematics concerned with the physical properties of systems that are preserved under continuous deformation, for example variations in the shape or size of an object (see Refs. [33, 34, 35]). While this field originated at the start of the 20th century[1], the discovery of the quantum Hall effect in 1980 represented the first experimental realisation of topologically protected behaviour in nature [4]. As we saw in the previous sections, the conducting edges in the IQHE are quantised to remarkable precision in units of e^2/h, and can only change in a discrete fashion. This quantisation is robust to physical perturbations, including the length of the edge or presence of disorder in a sample. In fact, it is the topologically non-trivial electronic band structure in the quantum Hall effect that gives rise to this phenomena, and endows the edges with *topological protection*.

To understand this, we first take a step back and consider 2D surfaces more generally. The *genus* of an object is a global property that is related to the number of holes in a system. Objects with the same genus can be smoothly deformed into one another. The canonical example is a sphere which has a genus of 0, and a doughnut which has a genus of 1. A doughnut can be pulled and elongated, but can not enter the same geometric class as a sphere without closing the gap in its centre. The two objects are topologically distinct. The Gauss-Bonnet and later Shiing-Shen Chern theorems [36] convey this relationship between geometry and topology as the integral of a surface's

---

[1] Although, it arguably has roots in the work of Euler in the 18th century.

curvature over an area. This concept can be mapped onto condensed matter systems by considering particle wavefunctions in momentum space (see §1.1). Integrating the Berry curvature over the Bloch bands gives rise to an integer quantity known as the Chern number, n, which classifies the topological character of different systems (see Refs. [33, 35] for detailed discussion).

In the IQHE, n is unity for each Landau level within a sample, and zero outside the sample. Such a system can be considered as a topological insulator where a gap exists between the fully filled and empty energy levels. It follows then that in order for n to change from a finite value to zero, a gap in the system has to close. In this way, energy levels that give rise to non-zero n must depopulate by crossing E_F at some point. This condition leads to the opening of n gapless 1D modes at the sample boundary, forming conductive edge channels. In the quantum Hall effect, the Chern number is therefore equivalent to the number of QH edge states in a system, with the sum of all Chern numbers giving the total conductivity in units of e^2/h [34].

While topological effects can be observed in the IQHE regime, realising this phenomenon requires a large magnetic field in order to break time reversal symmetry. In seminal work by Thouless [37] and later Haldane [38], a new type of ordering was predicted to occur in specific material systems in the absence of an external magnetic field. This topological phase of matter was later understood as the basis for the QAHE.

There are two key ingredients required to experimentally realise the QAHE: strong spin-orbit coupling, and the introduction of ferromagnetic doping (for reviews, see Refs. [39, 40, 41, 42]). The spin-orbit (S-O) interaction is a relativistic effect experienced in the rest frame of an electron that couples its spin to its orbital moment. The effect of S-O coupling in the QAHE is to drive inversion between the conduction and valence bands, as shown in Fig. 2.5. This leads to a topologically non-trivial band structure. The presence of ferromagnetic exchange then lifts the degeneracy at the Dirac point and opens a gap in 2D surface states ((c) in Fig. 2.5). This long-range coupling of magnetic impurities is proposed to be mediated by two different mechanisms: the RKKY interaction or Van Vleck paramagnetism [43]. Experimentally, these properties can be realised by introducing chromium or vanadium dopants in thin films of materials with

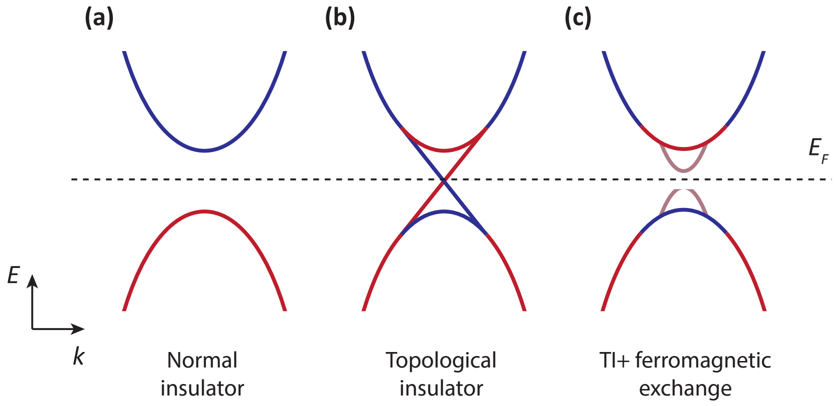

Figure 2.5: Band structure cartoon of topological insulators. (a) Energy band diagram for a normal insulator, with the fully filled valence band shown in red and the empty conduction band in blue. As the Fermi energy E_F (dashed black line) lies within gap between the two bands, the flow of current is prohibited. **(b)** Illustrates a topological insulator, where there is bulk band inversion between the conduction and valence bands. Topologically protected surface states can exist within the gap. In **(c)**, introducing ferromagnetic dopants like chromium or vanadium to a topological insulator leads to the breaking of time reversal symmetry, and opens a gap in the 2D surface states. Adapted from Ref. [34].

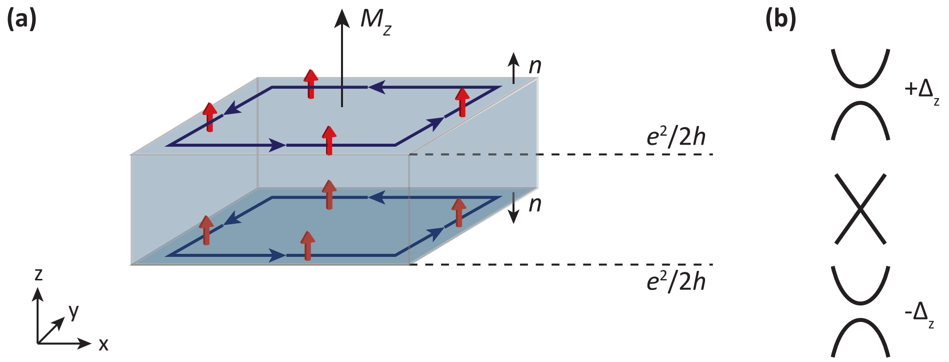

Figure 2.6: 3D thin-film magnetic topological insulator. **(a)** Illustration of two chiral paths (dark blue) located around the top and bottom corners of a thin-film topological insulator with ferromagnetic doping. The sample has been uniformly magnetised in the z direction such that $M_z = +1$ (indicated by the red arrows). Each channel contributes $e^2/2h$ to the total conductance, leading to a common fermionic, chiral path along the domain wall with $\sigma_H = e^2/h$. The relevant energy band structure is shown in **(b)**. The top and bottom surfaces have different topological characters (and therefore Chern numbers) owing to the net sample magnetisation and opposite pointing normal vectors. The energy gap between the bands is given by $\pm\Delta_z$. At the sidewall between the surfaces of different magnetisation, the gap closes and the Chern number is zero. Adapted from Refs. [42, 44].

a topologically non-trivial band structure. For example, the $Bi_2Se_3/Bi_2Te_3/Sb_2Te_3$ families.

Figure 2.6 illustrates the quantum anomalous Hall effect in a 3D magnetic thin film with strong S-O coupling. When polarised past the coercive field along z, all the electron spins align in one direction leading to a net sample magnetisation M_z. However as the normal vector takes opposite signs for the top and bottom surfaces, the Chern number must transition between $n = \pm 1$. This leads to the formation of a chiral edge state along the domain boundary at the side wall. The total conductance of this edge is given by the sum of the top and bottom surfaces, each contributing $e^2/2h$ for a total of $\sigma_H = e^2/h$. Experimentally, the first realisation of the QAHE was in Cr-doped $(Bi,Sb)_2Te_3$ in 2013 [45].

2.5 Edge magnetoplasmons

2.5.1 Classical description

In this final section, we describe the plasmon excitations that have been observed in 2DEGs with an applied perpendicular magnetic field. Of particular interest to us are *edge magnetoplasmons* (EMPs) - collective oscillations that are supported by the 1D chiral edge states in the quantum Hall regime.

EMPs in 2D fluids were first observed on the surface of liquid Helium in 1985 [46, 47]. In these systems, it was found that charged waves could propagate at the sample boundary with a frequency and dispersion distinct from that of the bulk modes. These resonant excitations were first interpreted within a classical framework [48, 49, 50], which has since proved successful in describing many of the microscopic features EMPs. Here we begin by discussing bulk plasmons in 2DEGs, following a description in Ref. [51]:

We consider a 2D fluid in the xy plane comprising a sea of negatively charged carriers. The system can be brought out of its equilibrium state by creating a charge perturbation of some length along x. Experimentally this could be achieved by applying a gate voltage to locally raise the electrochemical potential. This shift of δx causes a charge imbalance, and subsequently a restorative electric field. The movement of electrons under this field then creates a charge deficit in the opposite direction, leading to a periodically varying charge density wave back and forth across the sample. The oscillation frequency of this mode ω_p is given by

$$\omega_p^2(q) = \frac{2\pi n_s e^2}{m^* \epsilon_0 \epsilon^*}|q| \tag{2.22}$$

for wave vector q [50]. As the electric field E exists in 3 dimensions, it is therefore not only the properties of the electron plane, but also the effective dielectric of the substrate and surrounding environment (encapsulated in the term ϵ^*) that contribute to the plasmon velocity [51, 52]. The above relation holds in the limit of minimal scattering, so that the momentum relaxation time is much longer than the angular period $1/\omega$, i.e. $\omega\tau \gg 1$.

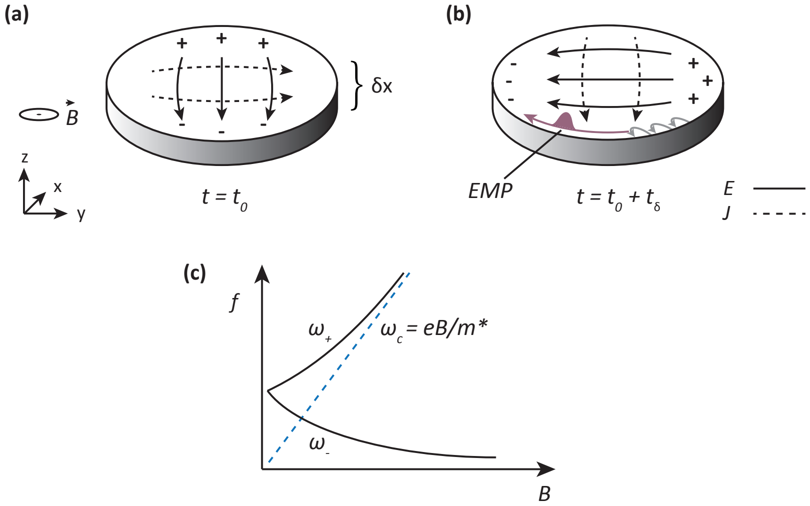

Figure 2.7: Edge magnetoplasmon modes. **(a)** and **(b)** Illustration of edge magnetoplasmons in a disk-shaped plane of electrons, adapted from Ref. [50]. A charge perturbation of δx gives rise to an electric field, E. In the case of an applied perpendicular magnetic field, B, the direction of the resultant current density, J, is along the y axis. At a time $t = t_0 + \delta t$ in (b), the electric dipole across the sample causes a redistribution of charge, leading to a density wave. In the quantum Hall effect regime, 1D channels at the edge can support such propagations, collectively known as EMPs. **(c)** Shows the upper and lower plasmon branches ω_+ and ω_- representing the bulk and edge-mode magnetoplasmon dispersions with magnetic field. At high magnetic fields, the bulk mode approaches the cyclotron frequency ω_c, while the edge mode follows an approximate $1/B$ curve.

In the presence of a magnetic field B applied in the z direction, the total angular frequency of the bulk magnetoplasmon modes will be the sum of contributions from ω_p and the cyclotron frequency $\omega_c = eB/m^*$.

$$\omega_{mp} = \omega_p + \omega_c. \tag{2.23}$$

This spectrum is gapped such that $\omega_p > \omega_c$.

2.5.2 EMPs in quantum Hall fluids

In the case of a strong perpendicular magnetic field, the electrons in the bulk of a QH liquid are localised in cyclotron orbits, and 1D gapless edge channels exist at the sample boundary [50, 51]. We consider a 2DEG located at $y = 0$, where the confining potential at the edge contributes to E_y. A local perturbation caused by a charge dipole can lead to an electric field across a sample as in [51] (Fig. 2.7 (a)). In the limit $\sigma_{xy} \gg \sigma_{xx}$ (corresponding to an integer-valued filling factor) the Hall angle θ_H approaches 90° and the direction of the resultant current density, J, is nearly perpendicular to E, where

$$J = \sigma_{xy} E. \tag{2.24}$$

This leads to a build up of negative charges along one side of the sample proportionate to the Hall current. The accumulation of charge at the edge gives rise to a secondary electric field and orthogonal current density. Electrons are propelled on towards the next edge, resulting in a self-propagating electric field and charge density wave which rotates around the sample with a phase velocity, v_D. Substituting $\sigma_{xy} = \nu e^2/h$ and $\nu = nh/eB$ into equation 2.5.2, we find

$$J = ne\frac{E}{B}. \tag{2.25}$$

We can therefore approximate v_D by the ratio of the electric to magnetic fields at the edge. This resultant oscillatory mode is localised to the perimeter P of the quantum Hall fluid where the charges accumulate, and is carried by the edge channels which cross the Fermi energy near the sample boundary. As the quantum Hall fluid along the edge is incompressible for integer filling factors, these ripples in the charge density are area-preserving.

From Ref. [50], the angular frequency ω_{EMP} for the fundamental EMP mode is given by

$$\omega_{EMP} = \frac{\sigma_{xy}}{2\pi\epsilon_0\epsilon^*} q(ln\frac{2}{qw} + C) \tag{2.26}$$

Which depends on the transverse Hall conductivity σ_{xy} and the wavevector $q = 2\pi/P$. For the case of a sharply defined edge with a step function density profile, the constant term C is equal to 1. The logarithmic correction arises from the long range nature of the Coulomb interaction, while w is a complex quantity related to the diagonal polarisability of the 2DEG and represents the physical width of the EMP mode away from the edge,

$$w = i\frac{\sigma_{xx}(\omega, B)}{2\omega\epsilon_0\epsilon^*}. \tag{2.27}$$

In the weakly-damped, collisionless Drude model, we can take limits of $\omega \ll \omega_c$ and $\omega\tau \gg 1$ and find the approximation

$$w = \frac{n_s m^*}{2\epsilon_0\epsilon^* B^2} \tag{2.28}$$

which relates the width to the electron density, and indicates that as B increases w narrows, confining the EMPs closer to the edge.

The dispersion in frequency for a fundamental EMP mode with magnetic field, along with the bulk plasmon mode is shown in Fig. 2.7 (c). While the upper branch ω_+ (the bulk mode, $\omega_p \propto n_s^{1/4}$) approaches the cyclotron frequency, the lower branch ω_- (the EMP mode, $\omega \propto n_s$) travels at a significantly reduced frequency which decreases with increasing magnetic field.

Part II

Scalable readout of GaAs-AlGaAs quantum dots

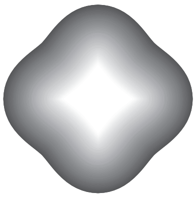

3

Dispersive readout of a few-electron double quantum dot with fast rf gate sensors

We report the dispersive charge-state readout of a double quantum dot in the few-electron regime using the in situ gate electrodes as sensitive detectors. We benchmark this gate-sensing technique against the well established quantum point contact (QPC) charge detector and find comparable performance with a bandwidth of ~ 10 MHz and an equivalent charge sensitivity of ~ 6.3 $\times 10^{-3}$ *e*/$\sqrt{\mathrm{Hz}}$*. Dispersive gate-sensing alleviates the burden of separate charge detectors for quantum dot systems and promises to enable readout of qubits in scaled-up arrays*[*].

---

[*] This Chapter is adapted from J. I. Colless[1], A. C. Mahoney[1], J. M. Hornibrook[1], A. C. Doherty[1], H. Lu[2], A. C. Gossard[2], and D. J. Reilly[1], "Dispersive readout of a few-electron double quantum dot with fast rf gate sensors", *Physical Review Letters*, **110**, 046805 (2013). DOI:https://doi.org/10.1103/PhysRevLett.110.046805. ©2013 American Physical Society

3. DISPERSIVE READOUT OF A FEW-ELECTRON DOUBLE QUANTUM DOT WITH FAST RF GATE SENSORS

Non-invasive charge detection has emerged as an important tool for uncovering new physics in nanoscale devices at the single-electron level and allows readout of spin qubits in a variety of material systems [53, 54]. For quantum dots defined electrostatically by the selective depletion of a two dimensional electron gas (2DEG), the conductance of a proximal quantum point contact (QPC) [55, 56, 57, 58, 59] or single electron transistor (SET) [60, 61] can be used to detect the charge configuration in a regime where direct transport is not possible. This method can, in principle, reach quantum mechanical limits for sensitivity [62] and has enabled the detection of single electron spin-states [55, 58, 63] with a 98% readout fidelity in a single-shot [64]

An alternate approach to charge-state detection, long used in the context of single electron spectroscopy [65], is based on the dispersive signal from shifts in the quantum capacitance [66, 67] when electrons undergo tunnelling. Similar dispersive interactions are now the basis for readout in a variety of quantum systems including atoms in an optical resonator [68], superconducting qubits [69, 70, 71] and nanomechanical devices [72].

In this Chapter we report dispersive readout of quantum dot devices using the standard, *in situ* gate electrodes coupled to lumped-element resonators as high-bandwidth, sensitive charge-transition sensors. We demonstrate the sensitivity of this gate-sensor in the few-electron regime, where these devices are commonly operated as charge or spin qubits [14] and benchmark its performance against the well established QPC charge sensor. We find that because the quantum capacitance is sufficiently large in these devices, gate-sensors have similar sensitivity to QPC sensors. In addition, we show that gate-sensors can operate at elevated temperatures in comparison to QPCs.

Previous investigations, in the context of circuit quantum electrodynamics (c-QED), have engineered a dispersive interaction between many-electron dots and superconducting coplanar wave guide resonators [73, 74, 75, 76, 77]. Recently, the charge and spin configuration of double quantum dots has also been detected by dispersive changes in a radio frequency resonator coupled directly to the source or drain contacts of the device [76, 78, 79, 80]. The present work advances these previous studies by demonstrating that the gates, already in place to define the quantum dot system, can also act as fast and sensitive readout detectors in the single-electron regime. This is a surprising result, given the small capacitive coupling between the gate and dot, but lifts a barrier to qubit readout in large scaled-up quantum dot arrays by alleviating the need for many ohmic contacts, large on-chip distributed resonators, or proximal charge detectors.

3.1 Experimental setup

Our gate-sensor, shown in Fig. 3.1 (a), comprises an off-chip superconducting Nb on Al_2O_3 spiral inductor ($L \sim 210$ nH) in resonance with the distributed parasitic capacitance ($C_p \sim 0.23$ pF) that includes a TiAu gate electrode used to define the quantum dots (resonance frequency $f_0 = 1/2\pi\sqrt{LC_p} = 704$ MHz, Q-factor ~ 70). As the sensitivity of the resonator is improved by minimising this parasitic capacitance, we deep etch the sapphire substrate between windings of the Nb inductor (lowering the dielectric constant) and make use of short bond wires between the inductor and GaAs chip[1]. The dots are 110 nm below the surface of a GaAs/$Al_{0.3}Ga_{0.7}$As heterostructure (electron density 2.4×10^{15} m^{-2}, mobility 44 m^2/V s at 20 K) that is mounted on a high-frequency circuit board [81] at the mixing chamber of a dilution refrigerator with base temperature $T \sim 20$ mK. The electron temperature T_e, determined by Coulomb blockade (CB) thermometry, is below 100 mK. The amplitude and phase response of the resonator is measured, following cryogenic amplification, using a vector network analyser, as shown in Fig. 3.1 (b).

Dispersive gate-sensors (DGS) detect charge-transitions (rather than absolute charge) by sensing small changes in the polarisability or quantum admittance [75] when an electron tunnels in response to the alternating rf gate voltage. Tunnelling modifies the resonator capacitance beyond the geometric contribution (at the position of green symbol in Fig. 3.1 (c)) compared to the regime where tunnelling is suppressed (orange symbol in Fig. 3.1 (c)). Changes in the quantum capacitance alter the resonator frequency, which in turn leads to a shift in the phase and magnitude of the reflected rf carrier. This response of the resonator $\Delta\phi$ is detected by fast sampling of the in-phase and quadrature components of the reflected rf to produce a baseband

---

[1] Using EM simulation software (Ansoft HFSS) we determine the inductor contributes 0.14 pF to the total parasitic capacitance $C_p \sim 0.23$ pF.

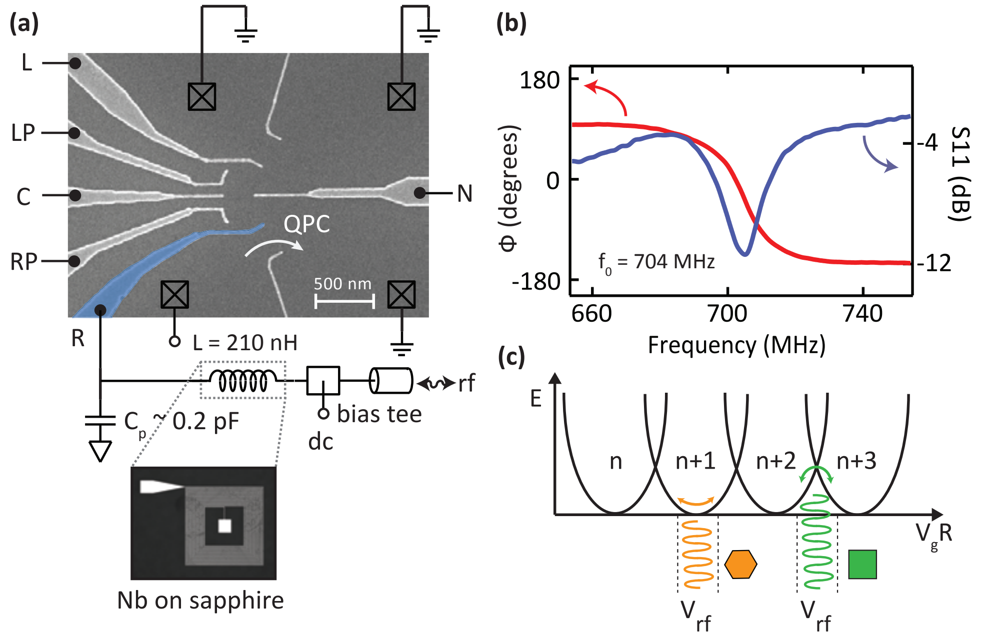

Figure 3.1: Experimental setup for dispersive gate sensing. (a) Micrograph of a similar device to the one measured and circuit schematic. One of the *in situ* dot-defining gates (blue) is coupled via a bondwire to an off-chip Nb/Al_2O_3 superconducting lumped-element resonator to enable dispersive readout. **(b)** Amplitude S_{11} (blue) and phase response (red) of the resonator. **(c)** Illustration of the charging energy spectrum for a quantum dot. The resonant rf gate voltage V_{rf} induces tunnelling at the charge degeneracy point (green oscillation) leading to a dispersive shift that is suppressed for configurations of stable charge (orange oscillation).

signal, V_{DGS}, proportional to the dispersive shift [27].

3.2 Characterisation and benchmarking

Our device integrates a QPC charge sensor together with the DGS and allows simultaneous readout of the quantum dot system using both detectors. A comparison of the relative sensitivity of the QPC and DGS is shown in Fig. 3.2 (a-d) where the response of each detector is measured as a function of the gate voltages V_gL and V_gR used to define a large, single quantum dot in the Coulomb blockade regime. The dispersive signal V_{DGS} from the gate resonator is shown in Fig. 3.2 (a,c), with Fig. 3.2 (b,d) showing the derivative of the conductance G of the QPC with respect to V_gL.

The sensitivity of both sensors is quantified by applying a small modulation voltage to a nearby gate, inducing periodic variation in conductance of the QPC or dispersive response of the DGS. A modulation in the dispersive response by a nearby gate can be understood as the variation in capacitance with depletion of electrons surrounding the DGS. We calibrate the detector signal dG or dV_{DGS} due to this modulation by comparing its amplitude to the signal response from a single electron transition. A measurement of the signal-to-noise ratio (SNR) in a given bandwidth yields the detector sensitivity. For the QPC we measure a typical charge sensitivity at 36 Hz of $\sim 3 \times 10^{-3}$ e/$\sqrt{\text{Hz}}$, corresponding to an integration time τ_{int} of 9 μs required to resolve a change of a single electron charge on the dot. The DGS method yields a $\tau_{int} = 39$ μs to resolve a single electron transition (equivalent to 6.3 $\sim \times 10^{-3}$ e/$\sqrt{\text{Hz}}$). The sensitivity of the DGS compares favourably to Ref. [78], where a τ_{int} of 4 ms is required to resolve a single electron charge using a resonator connected to a lead via an Ohmic contact. In comparison to the rf-QPC ($\tau_{int} \sim 0.5$ μs [27]) and rf-SET ($\tau_{int} \sim 100$ ns [82]) however, there is considerable room for improving the sensitivity of the DGS, for instance, by further decreasing the parasitic capacitance.

To determine the bandwidth of the dispersive gate sensor the SNR of its response is measured with increasing frequency of the small modulation voltage applied to a nearby gate (Fig. 3.3 (a)). This method gives a detection bandwidth of $\sim$ 10 MHz, limited by the Q-factor of the resonator, and consistent with the dependence of SNR with carrier frequency, as in Fig. 3.3 (b). We further characterise the DGS by measuring how the height and width of the electron transition signal (see Fig. 3.2 (c)) depends on applied resonator power, as shown in Fig. 3.3 (c). Optimal SNR is achieved for a power at the resonator of $\sim$ -80 dBm, corresponding to a gate voltage of $\sim$ 1 mV. Finally, we extract the relative geometric capacitive coupling between the sensor gate and the quantum dot. The charging energy of the dot $E_c = e^2/2C_\Sigma$, can be measured by using the DGS to sense Coulomb diamonds as a function of source-drain voltage across the dot $E_c = eV_{sd}$, as shown in Fig. 3.3 (d) (where e is the electron charge and C_Σ is the total dot capacitance). By measuring the period of CB oscillations we estimate that the gate-sensor geometric capacitance $C_g \sim 10$ aF contributes ~ 5 % of C_Σ.

For a single quantum dot biased at the point where electron n and $n+1$ are degenerate, the quantum capacitance is given by $C_Q = (e^2/4k_BT_e)(C_g/C_\Sigma)^2$ [79, 83], when the dot tunnel-rate is much larger than the resonator frequency (k_B is the Boltzmann constant). This quantum capacitance shifts the resonance frequency by an amount $\Delta f \simeq C_Q f_0/2C_p$, ($C_p$ is the resonator parasitic capacitance). This frequency shift results in an observed phase response $\Delta\phi \simeq \alpha C_Q Q/C_p$, ($Q$ is the Q-factor of the resonator). The constant of proportionality α is of order unity at resonance and is related to the transmission coefficient of the resonator. For $T_e \sim 100$ mK and $C_g/C_\Sigma \simeq 0.05$ this formula gives $C_Q \simeq 9$ aF which is broadly consistent with our observed phase shifts of $\Delta\phi \times 180/\pi \simeq 0.2$ degrees.

3.3 Double quantum dot sensing

Having quantified the sensitivity of the gate sensor, we now configure a double dot and show that this gate readout method can operate in the few-electron regime, where these devices are commonly operated as qubits. The double dot charge-stability diagram is detected using the dispersive gate-sensor as shown in Fig. 3.4 (a), where regions of stable electron number are labelled (n,m), corresponding to the number of electrons in the left and right dots. We confirm that the double dot is indeed in the few electron regime by also detecting the charge configuration using the proximal QPC charge sensor, as shown in Fig. 3.4 (b).

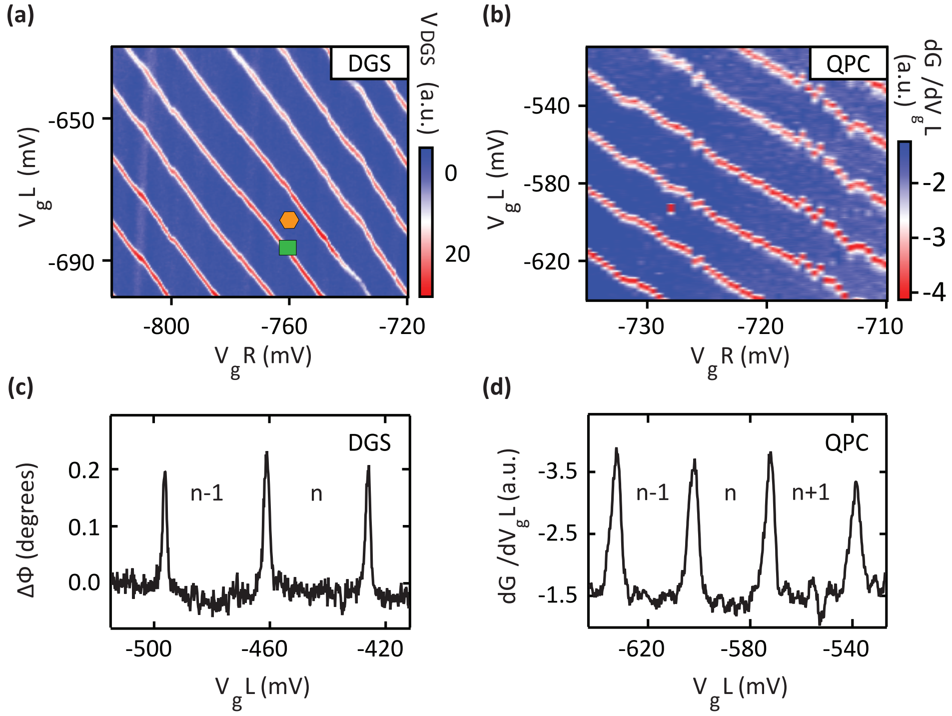

Figure 3.2: Comparison of DGS and QPC charge sensing of a single quantum dot. (a) Dispersive signal from the gate-sensor showing transitions in electron number for a large single quantum dot. Green and orange symbols correspond to positions of symbols in Fig. 1(c). **(b)** Derivative of the QPC conductance signal with gate voltage $V_g L$ in a region of gate-space similar to (a). The slight shift in gate voltage and period of the oscillations in comparison to (a) is due to the presence of the QPC gate bias. **(c)** Phase response of the gate-sensor showing peaks corresponding to single electron transitions. **(d)** Vertical slice through the conductance signal in (b), at $V_g R$ = -723 mV.

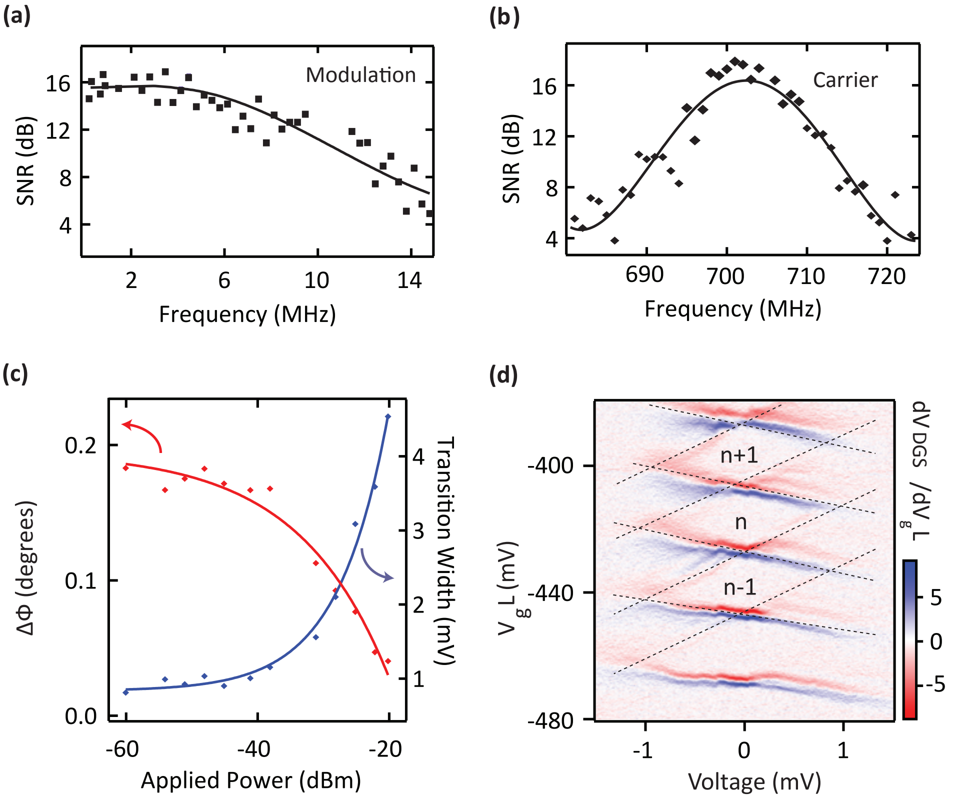

Figure 3.3: Benchmarking the DGS performance. **(a)** SNR of the gate sensor as a function of the modulation frequency of a signal applied to a nearby gate. **(b)** SNR for the gate sensor as a function of carrier frequency. **(c)** Width and height of the DGS response signal with power applied to the resonator (before ∼ 44 dB of attenuation). **(d)** Coulomb charging diamonds for the quantum dot, measured using the gate-sensor in a regime where direct transport is not possible. Colour scale is the derivative of the dispersive signal. Labels indicate number of electrons.

Charge sensing using QPCs or SETs requires that the sensor be kept at a value of conductance where sensitivity is maximised. This is typically achieved by applying additional compensating voltages to gates when acquiring a charge-stability diagram. It is worth noting that gate sensors do not require such offset charge compensation or gate voltage control. Of further practical use, we find that DGSs are robust detectors at elevated temperatures, in contrast to QPC charge sensors which suffer from a thermally broadened conductance profile and suppressed sensitivity with increasing temperature. The single-electron response of both QPC and DGS can be compared in Fig. 3.4 (c) for $T \sim 20$ mK and $T \sim 1100$ mK.

The gate sensor can be made to detect both intra and inter double dot tunnelling transitions, as shown in Fig. 3.5 (a) which depicts a close-up region of the charging diagram. A line-profile of the transitions (Fig. 3.5 (b)) indicates that the DGS is most sensitive to electron transitions from the right reservoir, due to its position, but is capable of distinguishing all transitions. Near an intra-dot transition, the quantum capacitance for the double dot can be shown to be $C_Q^{dd} = (e^2/2t)(C_g/C_\Sigma)^2$ where t is the tunnel coupling energy of the double dot [78]. As for the single dot above, the phase shift (in radians) is $\Delta\phi \simeq \alpha C_Q^{dd} Q/C_p$. The measured phase shift $\Delta\phi \simeq 0.1$ degrees for the intra-dot transition is near half the shift for transitions to the leads, consistent with a tunnelling coupling $t/h \simeq 8$ GHz.

Increasing the tunnel barriers between the double dot and the reservoirs suppresses the gate sensing signal when the tunnel rate drops substantially below the detector resonance frequency ($f_0 \sim 704$ MHz). This regime is reached in Fig. 3.5 (c), where transitions to the reservoirs are suppressed, but intradot transitions remain visible as these occur at a tunnel frequency above f_0. The observation of the intra-dot transition in the few-electron regime is important since it is this signal that forms the basis of spin qubit readout in these devices [14, 78, 80]. Of further note, in contrast to QPC or SET detectors that exhibit a broadband back-action spectrum [84], gate-sensors act-back on the qubit at a single, adjustable frequency.

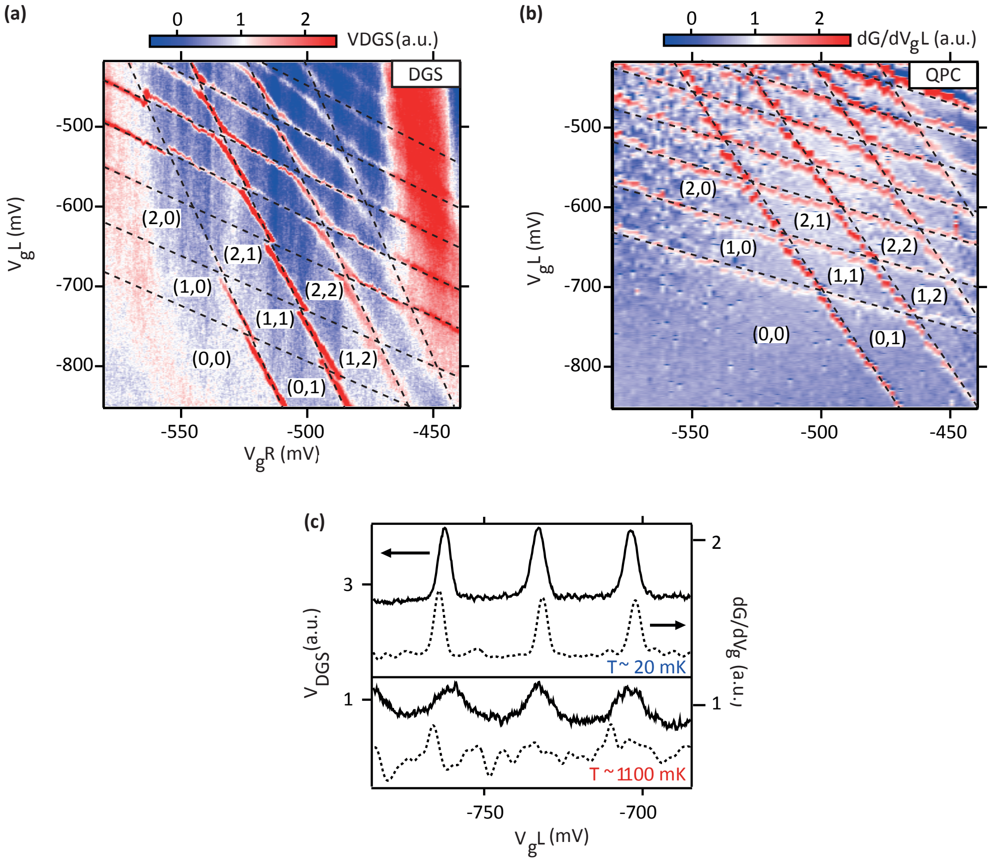

Figure 3.4: Readout of a double quantum dot. **(a)** Dispersive response V_{DGS} from the gate-sensor for a few-electron double quantum dot. Labels indicate number of electrons in the left and right dot. **(b)** Equivalent charge sensing signal from the QPC detector confirming the few-electron regime. The shift in location of the transitions compared to the data in (a) is due to the required QPC gate bias. **(c)** Temperature dependence of the sensing signal for both the DGS (left axis, solid line data) and QPC (right axis, dashed line data). The transitions are taken at a fixed V_gR and offset vertically for clarity. Both detectors resolve clear sensing peaks at $T \sim 20$ mK, with the QPC losing all sensitivity at elevated temperature $T \sim 1100$ mK.

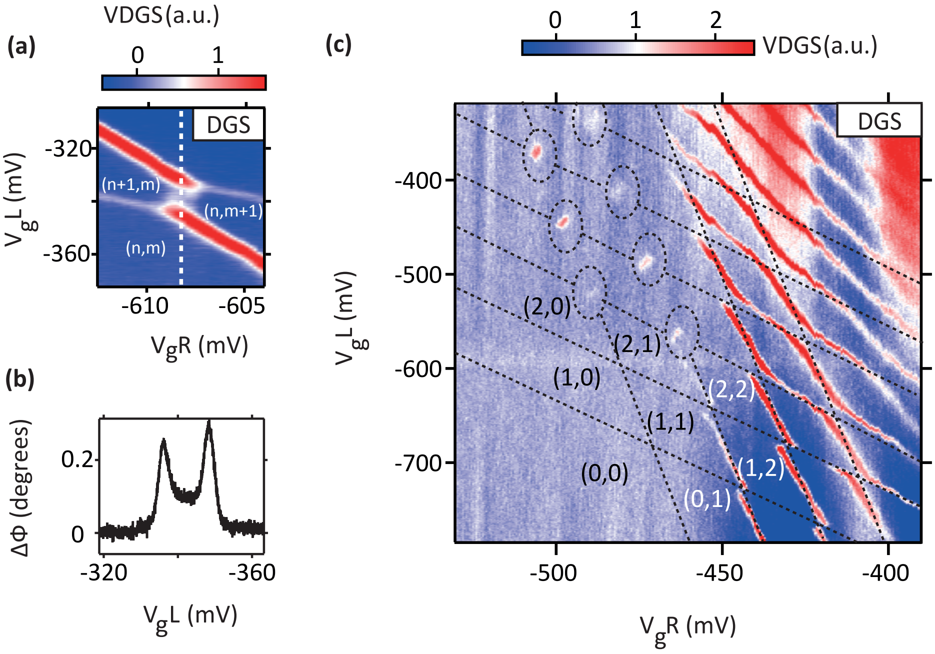

Figure 3.5: DGS readout in different tunnelling regimes. **(a)** DGS signal at a double dot charge transition. **(b)** The calibrated phase response from the DGS for a slice through (a) with $V_g R$ held at -608 mV. **(c)** Dispersive response of the gate-sensor where tunnelling to the reservoirs is suppressed in the few-electron limit. High tunnel rate, intra-dot transitions remain visible.

3.4 Conclusion

The demonstration that *in situ* surface gates also serve as readout detectors with comparable sensitivity to QPCs is perhaps unexpected, given that the geometric gate-to-dot capacitance is only ~ 5 % of the total capacitance. Readout using gate sensors, however, makes use of the quantum capacitance which as we have shown, can be of the same order as the geometric contribution ($C_g \simeq C_Q$). Gate-based readout then, has potential to address the significant challenge of integrating many QPC or SET detectors into large arrays of quantum dots, for instance, in the scale-up of spin qubit devices. The use of wavelength division multiplexing techniques [85, 86] would further allow each gate in an array to be independently and simultaneously read out at a unique frequency. Such an approach will also likely apply to systems without source-drain reservoirs altogether, such as donor qubits [87], or in the readout of Majorana devices [88].

3.5 Acknowledgements

We thank X. Croot and S. D. Bartlett for technical assistance and discussions. J.M.H. acknowledges a CSIRO student scholarship and use of CSIRO facilities for Nb inductor fabrication. We acknowledge funding from the U.S. Intelligence Advanced Research Projects Activity (IARPA), through the U.S. Army Research Office and the Australian Research Council Centre of Excellence Scheme (Grant No. EQuS CE110001013).

3.6 Author contributions

D.J.R. devised the project. J.I.C, A.C.M and J.M.H. carried out the experiments. H.L. and A.C.G. grew the materials. A.C.D. prepared the theory. D.J.R, J.I.C., A.C.M. and A.C.D. wrote the paper.

3.7 Author affiliations

[1]ARC Centre of Excellence for Engineered Quantum Systems, School of Physics, The University of Sydney, Sydney, NSW 2006, Australia.

[2]Materials Department, University of California, Santa Barbara, California 93106, USA.

4

Frequency multiplexing for readout of spin qubits

We demonstrate a low loss, chip-level frequency multiplexing scheme for readout of scaled-up spin qubit devices. By integrating separate bias tees and resonator circuits on-chip for each readout channel, we realise dispersive gate-sensing in combination with charge detection based on two radio frequency quantum point contacts (rf-QPCs). We apply this approach to perform multiplexed readout of a double quantum dot in the few-electron regime, and further demonstrate operation of a 10-channel multiplexing device. Limitations for scaling spin qubit readout to large numbers of multiplexed channels is discussed[*].

---

[*] This Chapter is adapted from J. M. Hornibrook[1], J. I. Colless[1], A. C. Mahoney[1], X. G. Croot[1], S. Blanvillain[1], H. Lu[2], A. C. Gossard[2] and D. J. Reilly[1], "Frequency multiplexing for readout of spin qubits", *Applied Physics Letters*, **104**, 103108 (2014). doi: http://dx.doi.org/10.1063/1.4868107. Used in accordance with the Creative Commons Attribution (CC BY) license.

Scaling-up quantum systems to the extent needed for fault-tolerant operation introduces new challenges not apparent in the operation of single or few-qubit devices. Spin qubits based on gate-defined quantum dots [14] are, in principle, scalable, firstly because of their small (sub-micron) footprint, and secondly, since spins are largely immune to electrical disturbance, they exhibit low crosstalk when densely integrated [89]. At the few-qubit level, readout of spin-states is via quantum point contact (QPC) or single electron transistor (SET) charge sensors, proximal to each quantum dot [27, 55, 56, 58, 60, 63]. These readout sensors however, pose a significant challenge to scale-up, in that they require separate surface gates and large contact leads, crowding the device and tightly constraining the on-chip architecture.

The recently developed technique of dispersive gate-sensing (DGS) overcomes this scaling limitation by making use of the gates, already in place to define the quantum dots, as additional charge sensors [90]. The gates act as readout detectors by sensing small changes in the quantum capacitance associated with the spin-dependent tunnelling of single electrons. In turn, shifts in capacitance are measured by the response of a radio-frequency (rf) *LC* resonator that includes the gate. In principle, all of the quantum dot gates used for electron confinement can also be used as dispersive sensors, simultaneously collecting more of the readout signal that is spread over the total device capacitance and thus increasing the signal to noise ratio. Enabling all-gate readout, as well as multichannel rf-QPC or rf-SET charge sensing, requires the development of multiplexing schemes that scale to large numbers of readout sensors and qubits.

Here we report an on-chip approach to frequency multiplexing for the simultaneous readout of scaled-up spin qubit devices. We demonstrate 3-channel readout of a few-electron double quantum dot, combining two rf-QPCs and a dispersive gate-sensor as well as the operation of a 10-channel planar multiplexing (MUX) circuit. Similar approaches to frequency multiplexing have been demonstrated for distributed resonators in the context of kinetic inductance detectors [91], superconducting qubits [92, 93] and rf-SETs [85, 86, 94]. The present work advances previous demonstrations by lithographically integrating the feed-lines, bias tees, and resonators, which are fabricated on a sapphire chip using low-loss superconducting niobium. By putting these components on-chip, the size of the entire MUX circuit is reduced far below the wavelength of the rf signals, suppressing impedance mismatches from the unintentional formation of stub-networks that otherwise occur in macro-scale multi-channel feed lines. Finally, we briefly discuss the ultimate limitations to scaling frequency multiplexing for spin qubit readout.

4.1 Experimental setup

Our readout scheme (Fig. 4.1 (a)) comprises a multiplexing chip fabricated from a single layer of superconducting niobium film (150 nm, $J_c = 15$ MAcm^{-2}, $T_c = 8.4$ K) on a sapphire substrate (r-cut, 3 mm × 5 mm × 0.5 mm) using optical photo-lithography and argon ion beam milling. The niobium remains superconducting at the moderate magnetic fields needed to operate spin qubits. Each inductor L_i in resonance with the parasitic capacitance C_p defines a unique frequency channel $f_i = 1/(2\pi\sqrt{L_i C_p})$ for addressing each readout detector. This multiplexing chip is mounted proximal to the spin qubit chip, consisting of a GaAs/Al$_{0.3}$Ga$_{0.7}$As heterostructure with two dimensional electron gas (2DEG) 110 nm below the surface (carrier density 2.4×10^{15} m^{-2}, mobility 44 m^2/V s). Ti/Au surface gates define the quantum dots and readout sensors. Bond wires connect the inductors L_i on the multiplex chip to rf-QPCs via an ohmic contact [27] or directly to the gates for the DGS readout [90]. The labels (i) - (iii) in Fig. 4.1 (b) are used to identify frequency channels for the separate readout detectors. Each resonant circuit contains an integrated bias tee for independent dc voltage biasing. Both the multiplexing chip and qubit chip are housed together in a custom printed circuit board platform [81] mounted at the mixing chamber stage of a dilution refrigerator with base temperature 20 mK.

The on-chip bias tees are constructed using interdigitated capacitors (Fig. 4.1 (d)) with critical dimension 3 μm and have size-dependent values between 3 pF and 5 pF, with lower frequency channels requiring a larger capacitance for similar insertion loss. To further increase the coupling capacitance we spin-coat the interdigitated sections with photoresist (AZ6612, $\epsilon \approx 4$) to yield a larger dielectric constant than free space. The inductors (red, Fig. 4.1 (e)), used in both the resonant circuit and bias tees, are spiral shaped with critical dimension 3 μm. The measured inductances (170, 250

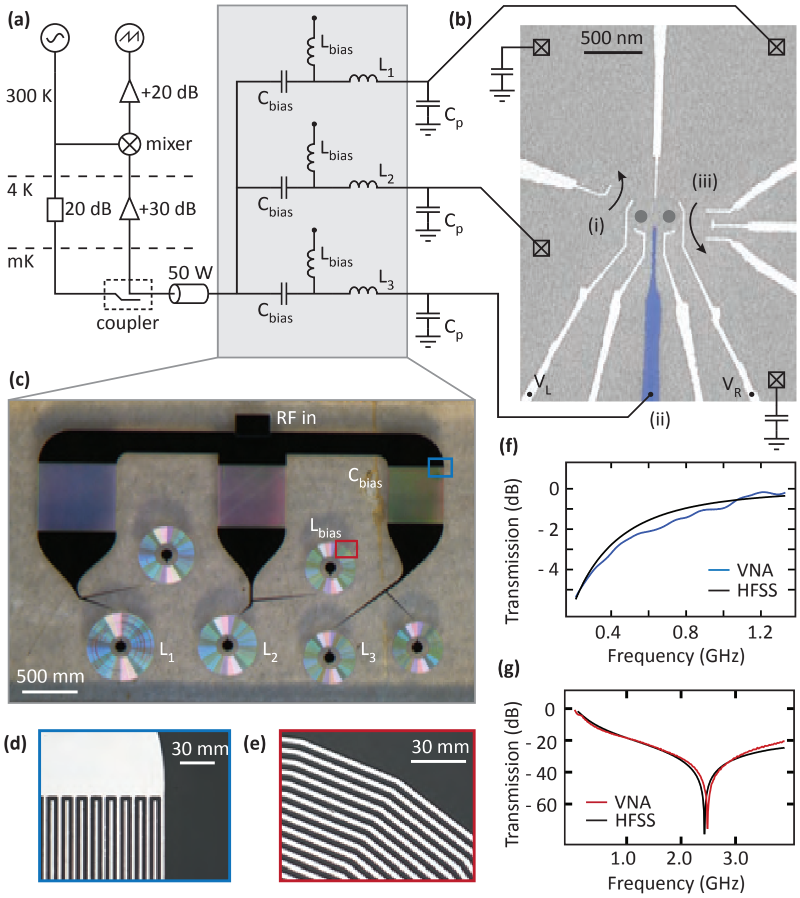

Figure 4.1: Experimental setup and multiplex chip characterisation. **(a)** Three channel frequency multiplexing scheme for spin qubit readout. The individual LC resonator circuits comprise a matching inductor L_i, parasitic capacitance C_p and a bias tee for independent biasing of each gate sensor. **(b)** Micrograph of the GaAs double dot device. Individual channels of the multiplexing chip are connected via bondwires to either a gate sensor (labelled (ii)) or an ohmic contact on one side of a QPC (labelled (i), (iii)). **(c)** Optical micrograph of the multiplexing chip which is patterned using niobium on a sapphire substrate, comprising interdigitated capacitors **(d)** and spiral inductors **(e)**. **(f), (g)** Microwave transmission through bias tee components - measurement via a vector network analyser (VNA) and 3D numerical simulation.

and 400 nH) are in agreement with analytical calculations based on their geometry [95]. The self-resonance frequency of all the inductors is increased by over-etching the sapphire dielectric between adjacent turns, decreasing the effective dielectric constant and reducing the capacitance. Measurements of the transmitted power for the individual planar components are shown in Fig. 4.1 (f,g) (blue, red trace) and yield agreement with numerics based on a 3D electromagnetic field simulation (black trace)[1].

4.2 Quantum dot readout

The multiplexing scheme is implemented using a 3-channel chip to read out the state of a double quantum dot. The frequency response of the chip strongly depends on the state of the readout detectors, as shown in Fig. 4.2 (a). In the absence of gate bias (black trace), the QPCs are far from pinch-off and the corresponding resonances are not apparent since the impedance of the LCR network is well away from the characteristic impedance of the feedline ($Z_0 \sim 50\ \Omega$). The resonances are formed (red trace) with the application of negative gate bias, depleting the electron gas and increasing the resistance of the QPC to bring the combined LCR network towards a matched load. Larger gate bias subsequently pinches-off the rf-QPC, further modulating the amount of reflected rf power at the resonance frequency. The response of the gate-sensor with bias is significantly different to that of the rf-QPC. For the gate-sensor, depleting the 2DEG beneath the gate also increases its resonance frequency, as shown in Fig. 4.2 (c). This frequency dependence arises from the change in parasitic capacitance as the electron gas is depleted. With the gate voltages typically needed for defining quantum dots, the parasitic capacitance C_p is of the order of 0.3 pF. Electromagnetic field simulation suggests contributions to C_p are roughly equal between 2DEG, bondwires and adjacent turns of the planar inductors. Given the large separation in resonance frequencies, crosstalk is negligible in this 3-channel implementation.

---

[1] EM simulation software HFSS Ansoft Corp. and Q3D extractor.

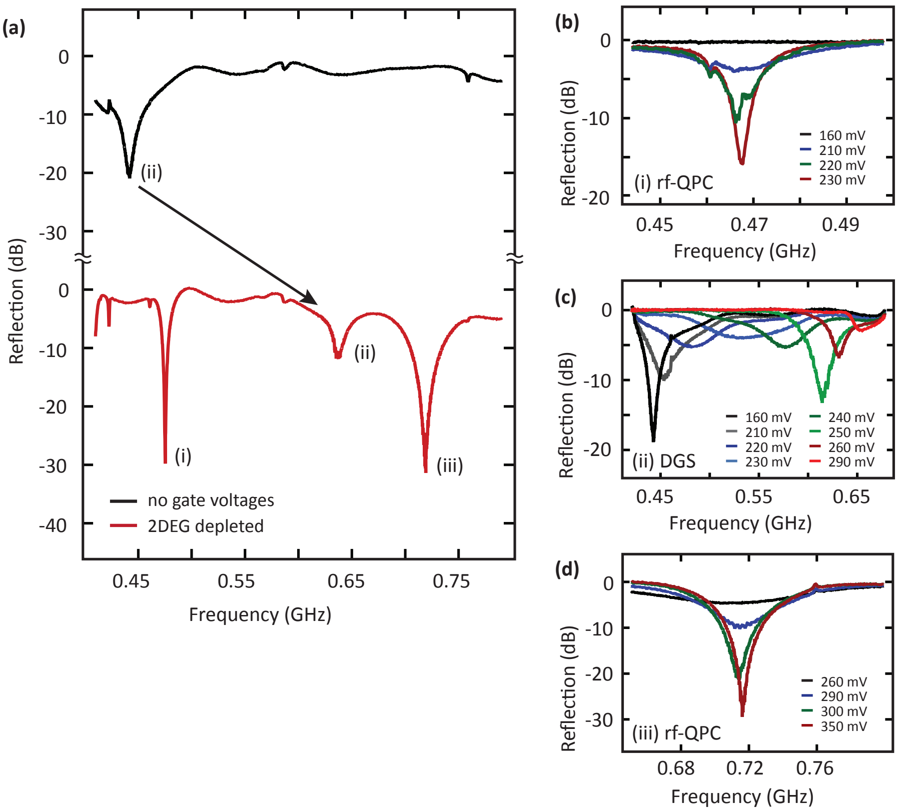

Figure 4.2: Frequency domain response. **(a)** Frequency response of MUX circuit separating left rf-QPCs (i), dispersive gate sensor (ii), and right rf-QPC (iii) into separate frequency channels. With negative voltage applied to the gates, the frequency response (shown in red) exhibits resonances as the impedance of the readout sensors approach the characteristic impedance of the feedline. **(b)** and **(d)** show the frequency response of the left and right rf-QPCs as the gate voltage modulates the conductance. **(c)** shows the frequency response of the dispersive gate sensor with gate bias. Note the significant shift in resonance frequency as the gate capacitance is reduced by depleting the electron gas beneath.

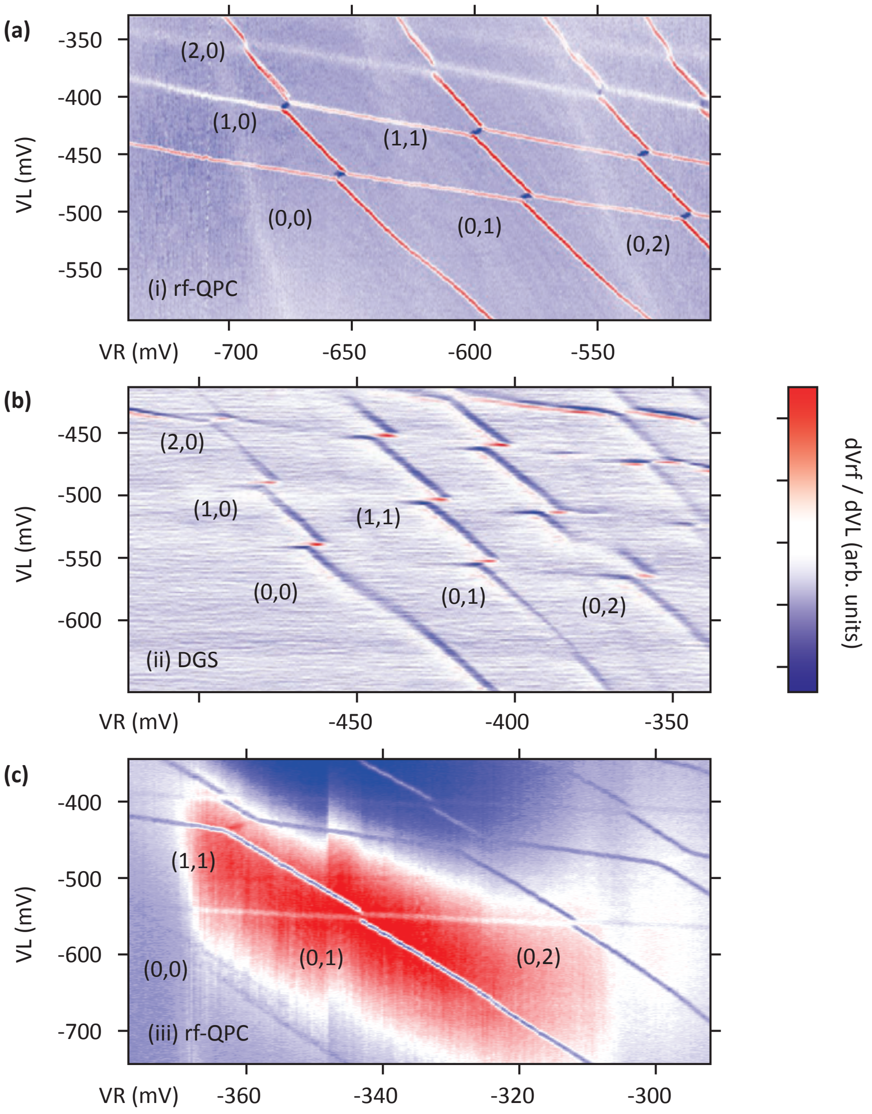

Figure 4.3: Multiplexed readout of double quantum dot in the few-electron regime. The derivative of V_{rf} with respect to V_L, in arbitrary units, is shown as a function of the voltages on the left and right gates, V_L and V_R. Charge stability diagrams **(a), (b), (c)** correspond respectively to readout using the separate channels (i), (ii) and (iii) as indicated in Fig. 2. Electron occupancy in the left and right dots is indicated by the labels (m,n). Note that when biasing the left and right QPC gates (needed for (a) and (c)) a different gate bias V_L and V_R is required for the same electron number.

We now demonstrate charge sensing measurements of a double quantum dot in the few-electron regime using this MUX configuration. The three independent readout channels (i, ii, iii) are separately addressable by selecting the rf carrier to match the respective resonance frequency. We note that direct digital synthesis can be used to create a single waveform that contains all of the separate carrier frequency components for each channel. The rf signal reflected from the MUX chip is first amplified at cryogenic temperatures before demodulation by mixing the generated and reflected rf tones. Low-pass filtering removes the sum component and, after further baseband amplification, yields a voltage V_{rf} proportional to the response of the resonance circuit [27]. Alternatively, high bandwidth analog to digital conversion can dispense with the need for separate mixers for each channel by directly acquiring the reflected waveform and performing demodulation in software.

Readout via the QPCs (i and iii) exhibits a typical charge stability diagram in the few-electron regime as a function of gate bias V_L and V_R as shown in Fig. 4.3(a,c). The label (m,n) denotes the number of electrons in the left and right quantum dot respectively with the colour axis proportional to the derivative of the readout signal with gate bias. In comparison to the rf-QPCs, the dispersive gate readout channel is only sensitive to charge transitions that occur at a tunnel rate that is above the resonator frequency [90]. Note that biasing the gates to tune the QPCs also shifts the voltages V_L and V_R, such that their values are dependent on which sensor is being read out.

4.3 10-Channel device

Having demonstrated our approach to frequency multiplexing, we investigate the scalability of this scheme by operating a 10-channel chip shown in Fig. 4.4 (a). The 10 channels are defined using inductors L_i with values between 60 nH and 250 nH that form a resonant circuit with parasitic capacitance C_p as described above. Each channel again integrates a bias tee, needed for independent biasing of the gate sensors. Operation of the 10-channel chip is tested at 4.2 K using a series of high electron mobility transistors (HEMTs) fabricated from a GaAs/$\mathrm{Al_{0.3}Ga_{0.7}As}$ heterostructure and connected to the MUX chip via bondwires. These HEMTs, shown in Fig. 4.4 (c), act as independent

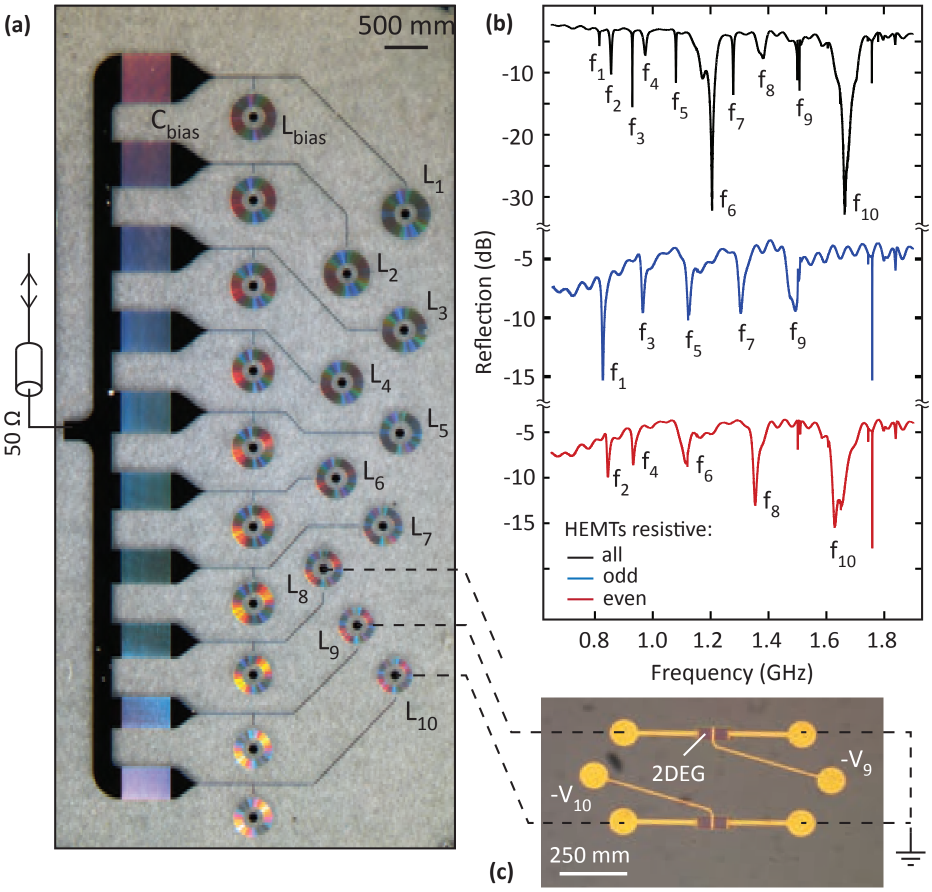

Figure 4.4: 10:1 Multiplex chip response. **(a)** Optical micrograph of a 10:1 MUX chip with integrated bias tees. **(b)** Frequency response of the MUX chip with inductors L_i each connected to GaAs HEMT with a gate-controllable conductance to mimic the response of 10 QPCs. Data shows the response with all HEMTs in the resistive state (black), odd HEMTs resistive (blue) and even HEMTs resistive (red). **(c)** Shows an optical micrograph of a section of the HEMT device with dashed lines indicative of bondwires.

variable resistors and mimic the response of 10 different QPCs for the purpose of testing the MUX scheme. With each HEMT connected to its corresponding resonator, the frequency response of the chip is shown in Fig. 4.4 (b), firstly with all HEMTs in the high resistance state (black trace). Selectivity of each frequency channel is demonstrated by alternatively biasing even-numbered (red trace) and then odd-numbered (blue trace) HEMTs. The exact resonance frequency is set by the contribution to the parasitic capacitance from the HEMT, which depends on the extent to which it is depleted. In this demonstration we have not carefully adjusted the resistance of the HEMTs to optimize the Q-factor of each resonator.

4.4 Conclusion

Frequency multiplexing allows simultaneous readout but requires separate resonator and bias circuits for each readout channel. Although the size of our demonstration devices are large, the use of alternate fabrication methods will likely alleviate any roadblock to scaling based on footprint. For instance, the use of multilayer processing for the capacitors C_{bias} can shrink their footprint to $\sim 15\ \mu\text{m} \times 15\ \mu\text{m}$ for similar capacitance. The space occupied by the bias tee inductors L_{bias} can be suppressed by using resistors instead of inductors to achieve high impedance. Reducing the critical dimension of the resonator inductors to ~ 100 nm results in a $55\ \mu\text{m} \times 55\ \mu\text{m}$ footprint for the largest (400 nH) inductor used here. Taken together, and assuming these superconducting circuits are fabricated on the same GaAs chip as the qubits, these dimensions suggest that thousands of readout channels are feasible in a moderately sized 1 cm × 1 cm area.

A more serious challenge is frequency crowding arising from the limited bandwidth available using planar lumped element inductors. For a maximum resonance frequency of ~ 5 GHz and given the need to separate channels by several linewidths to suppress crosstalk, the total number of independent gate sensors that can be read out simultaneously is ~ 100. Beyond this number several approaches are possible. These include a brute force method, duplicating the reflectometry circuit, including cryogenic amplifiers for every bank of 100 channels. Alternatively, the available bandwidth can be extended by making use of distributed resonators [96], but these typically have larger footprints.

Finally, if the constraint of simultaneous readout is relaxed, time domain multiplexing via cryogenic switching elements would allow readout of banks of frequency multiplexed channels to be interleaved in time. Whether qubit readout via such a time sequenced scheme is possible is likely dependent on the details of the particular quantum algorithm being implemented.

4.5 Acknowledgements

This research was supported by the Office of the Director of National Intelligence, Intelligence Advanced Research Projects Activity (IARPA), through the Army Research Office grant W911NF-12-1-0354 and the Australian Research Council Centre of Excellence Scheme (Grant No. EQuS CE110001013). Device fabrication is made possible through fabrication facilities at CSIRO (Lindfield) and the Australian National Fabrication Facility (ANFF). J. M. H. acknowledges a CSIRO student scholarship.

4.6 Author contributions

D.J.R. devised the project. J.M.H., J.I.C., A.C.M., and X.G.C. performed the experiments. J.I.C. and S.B. fabricated the quantum dot samples, and J.M.H. fabricated the multiplex chip. H.L. and A.C.G grew the materials. J.M.H. and D.J.R wrote the paper.

4.7 Author affiliations

[1]ARC Centre of Excellence for Engineered Quantum Systems, School of Physics, The University of Sydney, Sydney, NSW 2006, Australia.
[2]Materials Department, University of California, Santa Barbara, California 93106, USA.

5

Dispersive gate sensing the local electrostatic environment of a quantum point contact

Quantum point contacts (QPCs) are narrow passages of electron gas with a width defined via surface gates. They are a canonical example of one-dimensional (1D) confinement in quantum systems, and are frequently used as sensitive electrometers of charge in semiconductor-based quantum computing platforms. Here we present preliminary investigations into dispersive readout of a QPC by embedding one of its confining gates in a low loss, lumped-element resonant circuit. We qualitatively compare dispersive gate sensing (DGS) with traditional dc transport measurements during the depopulation of the last few 1D subbands of a QPC. Further, in the case of an asymmetric QPC gate geometry, the DGS response is found to be sensitive to charge rearrangement occurring past the point where dc transport is blocked[*].

---

[*] This Chapter contains preliminary investigations and unpublished experimental data. The relevant authorship is A. C. Mahoney[1], X. G. Croot[1], H. Lu[2], A. C. Gossard[2], J. D. Watson[3,4], G. C. Gardner[4,5], M. J. Manfra[3,4,5], and D. J. Reilly[1,6].

5. DISPERSIVE GATE SENSING THE LOCAL ELECTROSTATIC ENVIRONMENT OF A QUANTUM POINT CONTACT

Quantum point contacts (QPCs) in GaAs-AlGaAs heterostructures represent some of the most widely studied examples of quantum ballistic transport [21, 22]. They are formed by tapering two much larger electron reservoirs into a narrow channel where transport is restricted to a series of equally spaced energy subbands. Transmission through a QPC is commonly understood within a single-particle framework following the Landauer formalism [20, 97, 98]. In this picture, cancelling the electron group velocity with the 1D density of states leads to quantised conduction in the natural units of $2e^2/h$ (where e is the electron charge, h is Planck's constant, and the factor of 2 accounts for spin degeneracy). Correspondingly, transport measurements through QPCs exhibit a characteristic staircase in these units as a channel is electrostatically constricted, and eventually pinched-off using a negative gate bias.

However, despite extensive experimental and theoretical investigations into QPCs over the past decades, there remain a number of open questions in the field regarding transport beyond the last conductance plateau. Particularly striking is the presence a shoulder occurring at $0.7{\times}2e^2/h$ which cannot be explained within a non-interacting picture [26, 99]. A number of mechanisms have been proposed to account for this feature, including spontaneous spin-polarisation [99, 100], and effects related to Kondo physics [101, 102, 103]. Further, recent work has highlighted the role that the QPC geometry may play in hosting quasi-bound states [104, 105, 106]. Nevertheless, consensus is still lacking as to the origin of the 0.7 anomaly and, more broadly, the physics of QPCs near pinch-off.

Here we report non-invasive, fast charge sensing of a QPC via a channel-confining metallic surface gate. Following the dispersive gate sensing (DGS) technique described in Ref. [90], we embed a QPC gate electrode in a lumped-element LC resonant circuit comprising a superconducting, Nb spiral inductor, along with a parasitic capacitance to ground. The total capacitance of the surface gate is given by the series summation of two contributions: the geometric capacitance C_{geo}, and the quantum capacitance C_Q. Small changes in the local electrostatic environment modulate the quantum capacitance and thus admittance of the QPC, leading to a shift in the resonator frequency [78, 90, 107]. The reflected radio-frequency (rf) carrier wave is amplified at 4 K and mixed down to baseband, allowing a voltage signal (V_{DGS}) proportional to the quantum capacitance to be extracted. By comparing dc transport and the DGS response, we show that changes in V_{DGS} can be used to map out the 1D electron subband structure, echoing previous studies of compressibility in 1D systems via capacitive sensing [66, 108, 109]. Importantly, DGS readout does not require any additional on-chip structures, making it amenable to scaling-up towards large sensor networks. In addition, by measuring a range of different QPCs, we find that DGS can be sensitive to charge tunnelling events occurring past the point where direct transport is blocked. We attribute these features to charge pockets supported by an asymmetric QPC potential.

5.1 Experimental setup

Our dispersive gate readout setup is presented in Fig. 1 (a), (b). A split-gate style QPC formed with two symmetric TiAu finger gates is defined within a two-dimensional electron gas (2DEG). The 2DEG is located 110 nm below the sample surface, with an electron density of 2.4×10^{11} cm^{-2} and mobility 0.44×10^{6} cm^{2}/Vs. The QPC has lithographic dimensions of 350 nm (along y) × 400 nm (along x). Annealed ohmic contacts on either side of the channel provide a source and sink for dc current, I. The topmost gate electrode is wire bonded to one arm of a low-loss, planar frequency multiplexing chip (see Ref. [110] for details). A series, matching spiral inductor, $L = 400$ nH, and parasitic capacitance, $C_p \sim 0.2$ pF, form an LC tank circuit with a resonant frequency $f_0 = 1/2\pi\sqrt{LC}$. A secondary inductor and interdigitated capacitor serve as an on-chip bias tee. Varying the dc bias, V_{top} (coloured traces in 5.1 (c)) shifts the resonant dip towards higher frequencies. Black trace shows the response of the circuit at $V_{top} = 0$ mV. All measurements are carried out at the base temperature, $T \sim 20$ mK of a dilution fridge.

5.2 Comparing dc and DGS readout

Dc transport through the QPC is shown in Fig. 5.1 (d). A constant voltage, $V_{top} = -105$ mV is applied to the top finger gate, while V_{bottom} is swept. A two-terminal measurement of the differential conductance, G, is performed using a small excitation voltage

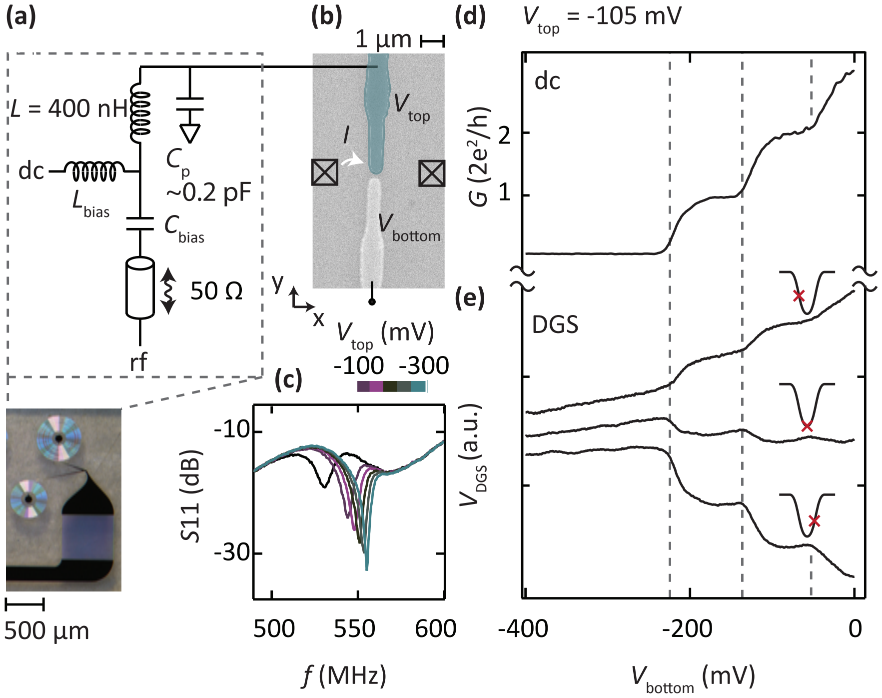

Figure 5.1: Experimental setup. **(a)** DGS readout circuit schematic and photograph of frequency-domain multiplexing chip. The microwave resonator comprises a 400 nH Nb spiral inductor patterned on a sapphire substrate, along with its parasitic capacitance to ground. An integrated on-chip bias tee allows for both rf and dc biasing (see Ref. [110] for details). **(b)** Electron micrograph of a QPC formed within a GaAs-AlGaAs 2-dimensional electron gas (2DEG) between two surface gates. The topmost gate (false coloured in blue) is bonded to a spiral inductor. S-parameter reflection measurements of the QPC and resonator setup are shown in **(c)**. Black trace corresponds to $V_{top} = 0$ mV, while coloured traces track the resonant dip with V_{top} across the range -100 mV to -300 mV. In **(d)**, the differential conductance through the QPC is shown as a function of V_{bottom}. **(e)** presents the demodulated rf signal V_{DGS} at $f_0 = 544$ MHz (middle trace), and to either side of the resonant frequency (indicated schematically with red crosses).

from a lock-in. Accounting for effects of resistor networks in the dc set-up, we calibrate transport through the QPC by linearly fitting the spacing between conductance plateaus to the expected value of $2e^2/h$. Figure 5.1 (e) plots the demodulated DGS response, V_{DGS}, across the same gate voltage range as (d). Measurements are performed at the resonant frequency of 544 MHz (middle trace), and 1 MHz to either side (top and bottom traces). Comparing the transport and rf traces, we observe inflections in the DGS response corresponding to risers in the quantised conductance, indicated by dashed lines. Depending on whether the circuit is probed slightly above or below f_0, these inflections manifest as peaks or dips. Greatest dynamic range is achieved slightly to the higher frequency side of f_0, where the resonant dip is steepest (Fig. 5.1 (c)).

These features are accounted for by considering the DGS as a local probe of quantum capacitance, $C_Q = e^2 dn/d\mu$ where $dn/d\mu$ is the density of states. By embedding a surface gate in a LC circuit, variations in C_Q can adjust the quantum admittance, and pull the resonant frequency by an amount $\Delta f \sim C_Q f_0/2C_p$. Turning again to Fig. 5.1 (e), we suggest the overall slope in the DGS response as the channel is pinched-off is likely related to both $C_{geo.}$ and C_Q. In the regions in transport where G is constant however, for example on plateaus or past pinch-off, changes in V_{DGS} are attributed to charge rearrangement in the 2DEG due to screening of the electric field from the gate. This screening is directly related to the compressibility κ of an electron gas, and therefore C_Q, as $\kappa = 1/n^2\ dn/d\mu$, where n is the charge density.

The differential conductance and DGS response measured with respect to source-drain bias, V_{SD}, are compared in Fig. 5.2. In (a) V_{top} is held at a constant potential of -120 mV and V_{SD} is varied. V_{bottom} is decreased between traces. Around $V_{SD} = 0$, bunched zones indicate flat conductance plateaus at multiples of $2e^2/h$. To the sides, the familiar finite bias half plateaus are observed where the source and drain potentials differ by a subband. The transconductance, dG/dV_g is plotted on the grey-scale axis in (b). Regions of constant conductance are indicated in white text. The DGS response over the same region in gate space is shown in (c) and (d). These 2D graphs are collated by rastering the voltage, V_{bottom}, at finite bias, and reading out the demodulated V_{DGS} signal amplitude on a digital sampling oscilloscope. The grey-scale plots of V_{DGS} and dV_{DGS}/dV_g are found to qualitatively reproduce the main features from the dc

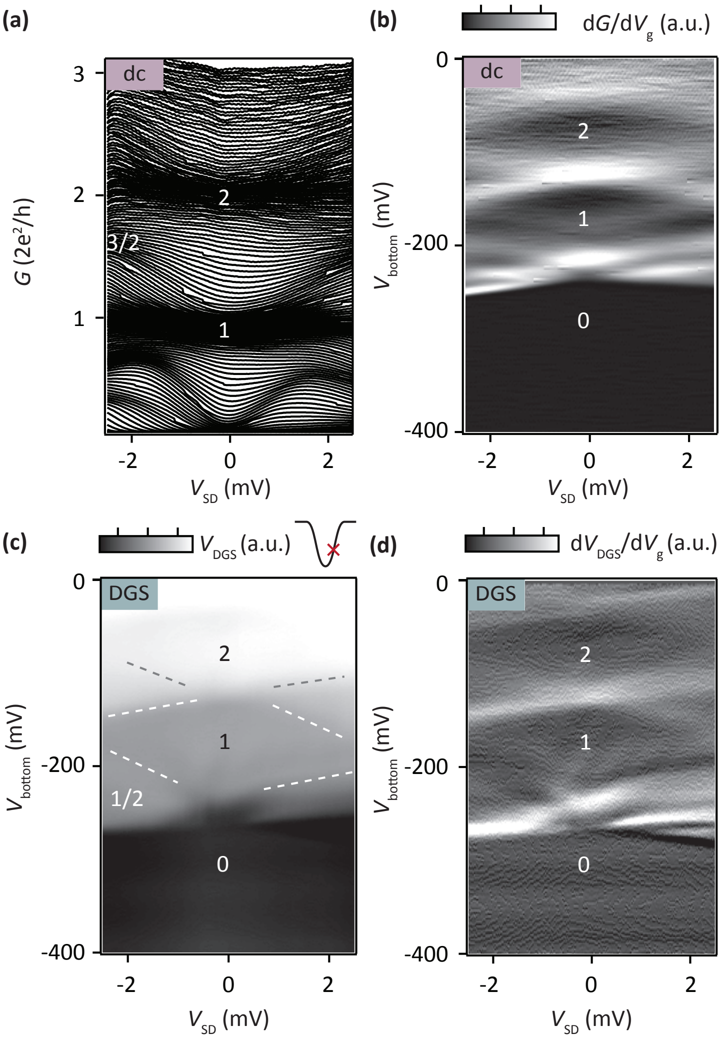

Figure 5.2: Comparison of dc transport and DGS sensing with source-drain bias. **(a)** Differential conductance, G through the symmetric finger-gate QPC in shown Fig. 5.1 (b), as a function of source-drain bias V_{SD}. V_{top} is held at a constant potential of -105 mV. 1D traces in units of $2e^2/h$ accumulate in dense regions, producing steps in G. **(b)** Shows the transconductance dG/dV_g, as V_{bottom} is made increasingly negative. Regions of constant conductance are indicated in white text. **(c)** and **(d)** present the DGS signal and its derivative over the same region in gate-space as the dc traces. Dashed lines are a guide to the eye. These measurements are taken at a frequency of 545.5 MHz.

differential conductance shown in (b).

5.3 Asymmetric QPC geometry

We contrast this symmetric finger-gate QPC with a geometry more commonly used to perform readout of quantum dots (Fig. 5.3 (a)). In such architectures, sensing channels are frequently formed using a gate placed at an angle to a dot-confining 'wall' electrode. When the QPC is biased just below $G = 2e^2/h$, it can be sensitive to charge movement in the proximal quantum dot system. The device shown in Fig. 5.3 (a) has a 2DEG located 91 nm below the surface, with a density of 1.34×10^{11} cm^{-2} and mobility of 3.24×10^6 cm^2/Vs. A QPC can be defined between the right wall gate (RW), and the gates directly below it. The lithographic width of the constriction is $\sim$ 200 nm.

DC transport through a QPC formed between V_{RW} and V_{g1} is shown in Fig. 5.3 (c). V_{RW} is held at a constant voltage of -380 mV, while V_{g1} is made increasingly negative. A constant line resistance is subtracted from the dc traces, setting the step-like feature in (c) to $G_0 = 2e^2/h$. While the conductance does not exhibit flat plateaus expected for transport through individual 1D modes, this behaviour is not uncommon for asymmetric geometry QPCs used as sensors. The DGS response over the same gate range is shown in (d). The LC circuit is probed at a frequency of 554 MHz, corresponding slightly to one side of the resonance dip (Fig. 5.3 (b)). Black arrows indicate the position where the channel is pinched-off, $V_{g1} = -750$ mV. The DGS signal is observed to mirror features in transport, including a pronounced riser just prior to the closing of the channel. In addition, beyond the point where G has gone to zero, a strong peak occurs in the rf response around -1150 mV.

To investigate this unexpected peak further, Fig. 5.3 (e) and (f) present side-by-side bias plots of dG/dV_g and V_{DGS}. Towards the top of both the plots, edges mapping out transmission through the last QPC mode are visible (indicated by dashed lines). Half-plateaus are shown at either side, at high bias. Below this region, the channel is pinched-off and $G = 0$. In (f) however, bright lines are observed starting from the region in gate voltage where the channel is just closed, and continuing with decreasing

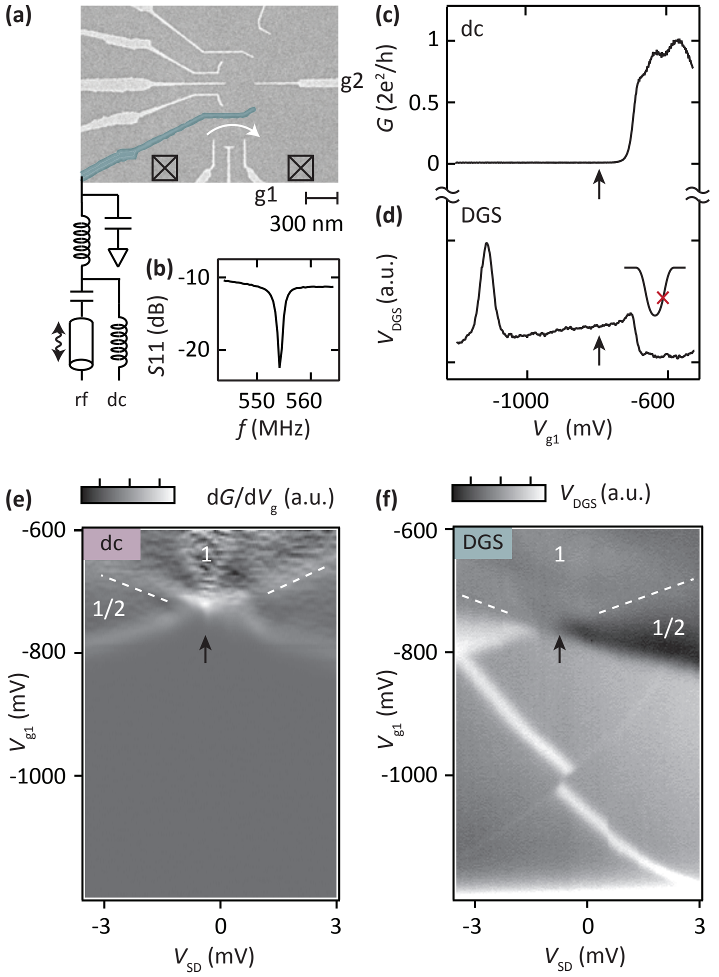

Figure 5.3: Experimental setup for asymmetric QPC gate geometry. **(a)** Electron micrograph of a typical double quantum dot gate pattern with proximal sensing channels. In this geometry, QPCs can be formed between the right wall (RW, false-coloured in blue), and the gates below. RW is bonded to a *LC* resonant circuit, nominally identical to the frequency-multiplexed chip pictured in Fig. 1 (a). S-parameter reflection measurement, $S11$ is shown in **(b)** with V_{RW} = -440 mV. The differential conductance, **(c)**, and DGS signal at 554 MHz, **(d)**, are compared as the QPC channel formed between RW and g1 is narrowed. 1D trace in (c) is taken with a source-drain voltage of -0.5 mV to account for a small offset bias across the device. 2D bias plots as a function of V_{g1} are presented in **(e)** and **(f)**. Here V_{RW} = -380 mV. White numbers label regions of constant conductance in units of $2e^2/h$, and black arrows at V_{g1} = -750 mV point to where the channel is pinched off. Dashed lines are a guide to the eye to indicate the edges of the first 1D subband.

V_{g1}. Lines from both positive and negative high bias regions are found to cross near zero bias, leading to a switch-like jump in the signal.

The evolution of this feature is tracked in Fig. 5.4 as the right wall gate voltage is varied. V_{RW} is indicated at the top of graphs (a) through (f). Changing the voltage on one gate of the QPC increases the depletion zone under that electrode, and corresponds to laterally shifting the channel along the y direction. This displacement has the effect of moving the DGS peaks across the source-drain spectrum in gate-space, and edging the crossing towards the QPC opening. We find qualitatively similar features in another QPC with an asymmetric gate geometry on the same device, highlighting the reproducibility of this phenomena (see Appendix A). At V_{RW} = -390 mV (Fig. 5.4 (e)), the DGS crossing intersects with the closing of the QPC. In this regime, the bright lines appear to cut through the last half subband at high bias. This effect is also visible in the non-linear conductance plot in (g), where bunching of the 1D traces occurs at the same region in gate-space as (e). We do not observe such conductance inflections in the dc transport plots for lower values of $|V_{RW}|$. The 2D transconductance, dG/dV_g is shown in (h), where a stripe is visible at high bias, below the first subband.

5.4 Discussion

The agreement of the peaks occurring in Fig. 5.4 (e), with the charge accumulation signatures in (g) and (f) (indicated by red arrows) suggests that the origin of these unexpected features is not related to the capacitive sensing technique itself. We note that this effect is distinct from the situation in scanning gate microscopy (SGM) experiments, where a charged tip creates a local potential hill [111]. When placed near one-another, a QPC and SGM tip can act as two mirrors of a Fabry-Pérot cavity, and induce interference effects and current branching [106, 112, 113]. In our setup, the LC circuit adds an oscillating voltage to the gate electrode, but does not alter the shape of the QPC confinement potential. As identified in Ref. [90], DGS can however resolve charge tunnelling events occurring on timescales faster than the probe frequency of the resonator. In this way, while both DGS and dc transport measurements show similar features when the QPC is open, only DGS is sensitive as the transmission through the

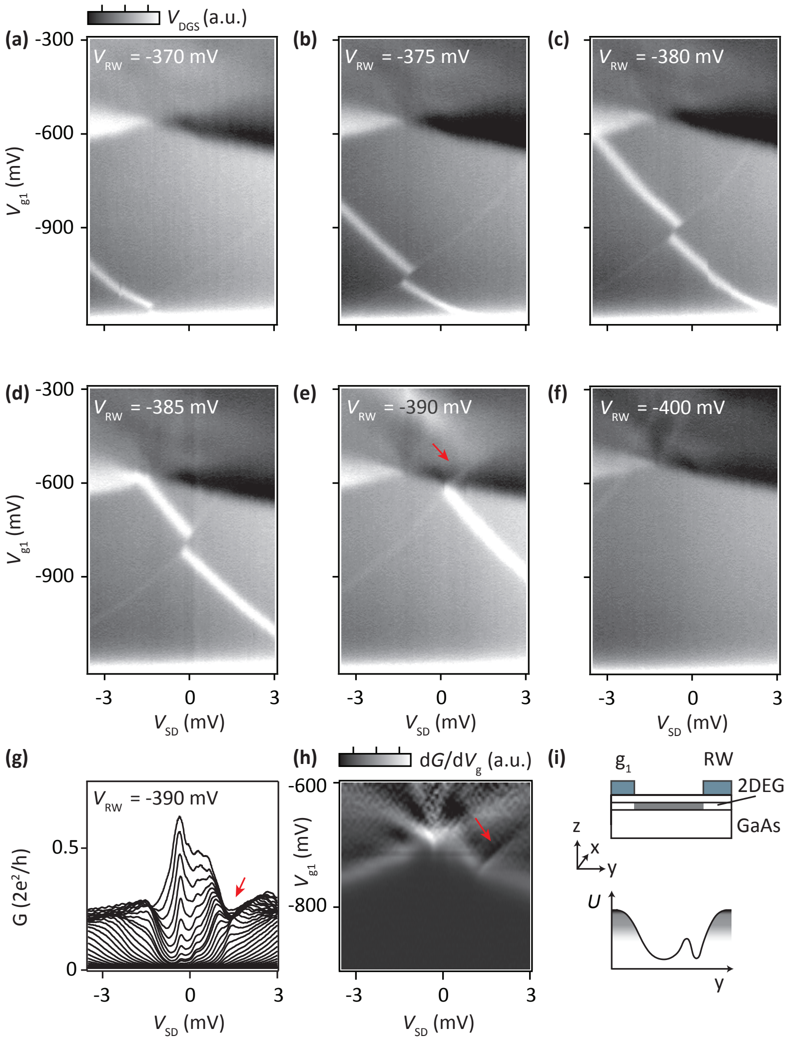

Figure 5.4: Laterally shifting the QPC channel. **(a) - (f)** DGS response (grey-scale) with V_{g1} and source-drain bias. V_{RW} is decreased from -370 mV to -400 mV, corresponding to displacing the QPC channel along y. **(g)** and **(h)** Show the differential conductance, G, and transconductance, dG/dV_g, with V_{SD}, at $V_{RW} = -390$ mV. Red arrow in **(e)** points to bright features in the DGS signal above pinch-off, aligning with the accumulation of 1D traces in the conductance in **(g)**, **(h)**. This feature is attributed to the discharging of a local charge trap forming near the right wall gate, illustrated in **(i)**. Top panel shows a vertical slice through the device, with depletion zones underneath $g1$ and RW. The QPC potential, U, is presented in the cartoon underneath, with an additional charge pocket existing near RW.

channel is reduced.

We attribute the unexpected features in the dc and DGS response to trapped charge in the region of the QPC. This likely stems from a potential well or 'charge pocket' due to the asymmetric gate geometry, which modifies the expected saddle point potential of the QPC (Fig. 5.4 (i)). Tunnelling transitions which affect the quantum capacitance can be detected by the dispersive gate sensor. This picture is consistent with the observation that laterally shifting the QPC channel modulates both G and V_{DGS}. In addition we suggest that the charge pocket exists underneath or proximal to the right wall gate (see Fig. 5.4 (i)), where the resonator is most sensitive to charge movement. Within this picture, increasing V_{RW} raises the potential of the trap, and moves the QPC channel towards g_1. This reduces the voltage required to discharge the local charge pocket, V_{g1}. For sufficiently high V_{RW}, the trapped charge can exit via the QPC subbands and thereby tunes the dc conductance. A similar scenario is invoked in Ref. [114], where extensive experimental studies of transport through p-type QPCs yield unexpected conductance features reminiscent of those presented here. Finally we note that the application of an in-plane magnetic field up to 2.5 T (the limit in our setup) does not lead to the suppression of the DGS bright lines, further distinguishing these local features from other generic conductance anomalies. Likewise, the DGS peaks are found to persist with increased cryostat base temperature up to 1.7 K, albeit with significant broadening (see Appendix A).

5.5 Conclusion

In conclusion, we have used an *in situ* dispersive gate sensor to probe the rf response across different QPC geometries as their width is decreased. By comparing these results to well understood dc conductance measurements, features in the demodulated response of the resonator are mapped to transport through the QPC 1D subbands. In the regime where transmission through the channel is non-zero, we observe inflections in V_{DGS} corresponding to changes in the compressibility of the electron gas. Further, in multiple asymmetric QPC gate geometries, unexpected peaks are apparent in the DGS response. These peaks can be adjusted by laterally shifting the channel, and are attributed to charge rearrangement from a local potential well in the vicinity of the QPC. While these features are not yet fully understood, this non-invasive technique opens a window to previously undocumented processes occurring in the regime where dc transport is no longer sensitive. In this way DGS may shed light on ongoing areas of contention related to QPCs, as well as informing future designs of semiconductor qubit sensors.

5.6 Acknowledgements

We acknowledge J.I. Colless for the fabrication of the quantum dot device, and J. M. Hornibrook for the development and provision of the multiplexed readout chip. We acknowledge funding from the U.S. Intelligence Advanced Research Projects Activity (IARPA), through the U.S. Army Research Office and the Australian Research Council Centre of Excellence Scheme (Grant No. EQuS CE110001013).

5.7 Author contributions

D.J.R. devised the project. A.C.M. carried out the experiments with X.G.C. Materials were grown by J.D.W., G.C.G, M.J.M., H.L. and A.C.G. The paper was written by D.J.R. and A.C.M.

5.8 Author affiliations

[1]ARC Centre of Excellence for Engineered Quantum Systems, School of Physics, The University of Sydney, Sydney, NSW 2006, Australia.
[2]Materials Department, University of California, Santa Barbara, California 93106, USA.
[3]Department of Physics and Astronomy, Purdue University, West Lafayette, Indiana 47907, USA.
[4]Birck Nanotechnology Center, School of Materials Engineering and School of Electrical and Computer Engineering, Purdue University, West Lafayette, Indiana 47907, USA.
[5]Station Q Purdue, Purdue University, West Lafayette, Indiana 47907, USA.
[6]Station Q Sydney, The University of Sydney, Sydney, New South Wales 2006, Australia.

Part III

Quantum Hall plasmonics

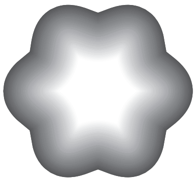

6

On-chip microwave quantum Hall circulator

*Circulators are non-reciprocal circuit elements integral to technologies including radar systems, microwave communication transceivers, and the readout of quantum information devices. Their non-reciprocity arises from the interference of microwaves over the centimetre-scale of the signal wavelength, in the presence of bulky magnetic media that breaks time-reversal symmetry. Here we realise a completely passive on-chip microwave circulator with size 1/1000th the wavelength by exploiting the chiral, 'slow-light' response of a two-dimensional electron gas (2DEG) in the quantum Hall regime. For an integrated GaAs device with 330 μm diameter and $\sim$ 1 GHz centre frequency, a non-reciprocity of 25 dB is observed over a 50 MHz bandwidth. Furthermore, the non-reciprocity can be dynamically tuned by varying the voltage at the port, an aspect that may enable reconfigurable passive routing of microwave signals on-chip**.

---

*This Chapter is adapted from A. C. Mahoney[1,2], J. I. Colless[1,2], S. J. Pauka[1,2], J. M. Hornibrook[1,2], J. D. Watson[3,4], G. C. Gardner[4,5], M. J. Manfra[3,4,5], A. C. Doherty[1], and D. J. Reilly[1,2], "On-Chip Microwave Quantum Hall Circulator", *Physical Review X*, **7**, 011007 . DOI: https://doi.org/10.1103/PhysRevX.7.011007. Used in accordance with the Creative Commons Attribution (CC BY) license.

Miniaturised, non-reciprocal devices are currently of broad interest for enabling new applications in acoustics [115], photonics [116, 117], transceiver technology [118], and in the regime of near quantum-limited measurement [119, 120, 121, 122, 123], where they are needed to isolate qubits from their noisy readout circuits.

Since the 1950s, passive circuit elements exhibiting non-reciprocity at microwave frequencies have been implemented using bulky magnetic devices that are comparable in scale to the centimetre wavelength of signals in their operating band. The footprint of these components poses a major limitation to integrating entire systems on a chip, such as what is required, for instance, to scale-up quantum computing technology.

A seemingly obvious means of realising non-reciprocity on a semiconductor chip is to use the Hall effect, where an external magnetic field breaks the time reversal symmetry of electrical transport [124]. Hall-based devices were ruled out in 1954 however [125], since near the electrical contacts, where the current and voltage are collinear, dissipation is so significant that the usefulness of this approach is greatly limited. This dissipative mechanism has an analog in the quantum Hall regime where the two-terminal resistance of a device is always finite over a scale of the inelastic scattering length as carriers transition from their contacts to the dissipationless, one-dimensional (1D) edge-states that support transport [126]. Recently, Viola and DiVincenzo [123] have proposed a means of addressing the limitation imposed by 2-terminal dissipation, suggesting the possibility of coupling microwave signals to the edge of a quantum Hall device reactively, without using traditional ohmic contacts. In a geometry where the signal ports of the device are positioned orthogonal to an incompressible quantum Hall edge-state, microwave power is coupled capacitively and non-dissipative transport in one-direction appears possible [123].

Here we engineer, on-chip, a chiral microwave interferometer that yields a high degree of non-reciprocity and dynamic range, with the low-dissipation inherent to edge transport in the quantum Hall regime. Configured as a completely passive 3-port circulator, our device demonstrates non-reciprocal operation at frequencies and magnetic fields commonly used for the read out of spin qubits [27, 63, 90, 127], facilitating integration with such semiconductor technologies. In comparison to traditional ferrite-based microwave components, this quantum Hall circulator is reduced in size by a factor of $\sim 1/1000^{\text{th}}$ the wavelength and exhibits a new mode of operation in which circulation can be dynamically reconfigured either by applying a dc voltage to the port electrodes, or by altering the strength of the magnetic field. A simple model based on a Fano-resonance mechanism [128] qualitatively accounts for the observed phenomena.

6.1 Experimental setup and results

6.1.1 Transmission line spectroscopy of EMP modes

Central to the operation of our device are edge magnetoplasmons (EMPs), resonant edge modes first observed classically on the surface of liquid Helium [46, 47]. Such excitations have since been found to propagate along a quantum Hall edge in response to a capacitively coupled microwave excitation [50, 52, 129, 130, 131, 132, 133, 134]. These chiral excitations travel with a velocity $v_{EMP} \sim |\vec{E}|/|\vec{B}|$, set by the ratio of the electric field $\vec{E}$ at the sample boundary and the applied magnetic field $\vec{B}$ [130].

For a high mobility 2DEG formed at the interface of the semiconductors GaAs and AlGaAs (see Appendix B for details), the velocity of the EMP modes is typically $v_{EMP} \sim 10^5$ ms^{-1} [135, 136], some 1000 times slower than the speed of light in the semiconductor dielectric. In order to exploit these EMPs to realise non-reciprocal microwave devices, we first detect their presence in a contactless etched disk of quantum Hall fluid by coupling to a proximal metallic coplanar transmission line (CTL) [137], as shown in Fig. 6.1 (a) and 6.1 (b). By measuring the transmitted microwave power through the CTL as a function of frequency f, a spectrum of discrete features is observed with applied magnetic field B (Fig. 6.1 (c)). We identify EMP modes in the data with frequencies set by the edge velocity and circumference of the disk, following the dependence $f \sim B^{-1}(\log(B^2) + \text{const.})$ [50], and extract the effective dielectric constant $\epsilon^* \approx 8.7$ consistent with the propagation medium [52, 138] (see Appendix B). Comparing the microwave spectrum to transport measurements from a Hall bar on the same chip (Fig. 6.1 (d)), we note that at high field (with only the last few Landau levels occupied) features resolve into discrete, crescent-shaped resonances that coincide with minima in the longitudinal resistance R_{xx}, where dissipation is suppressed.

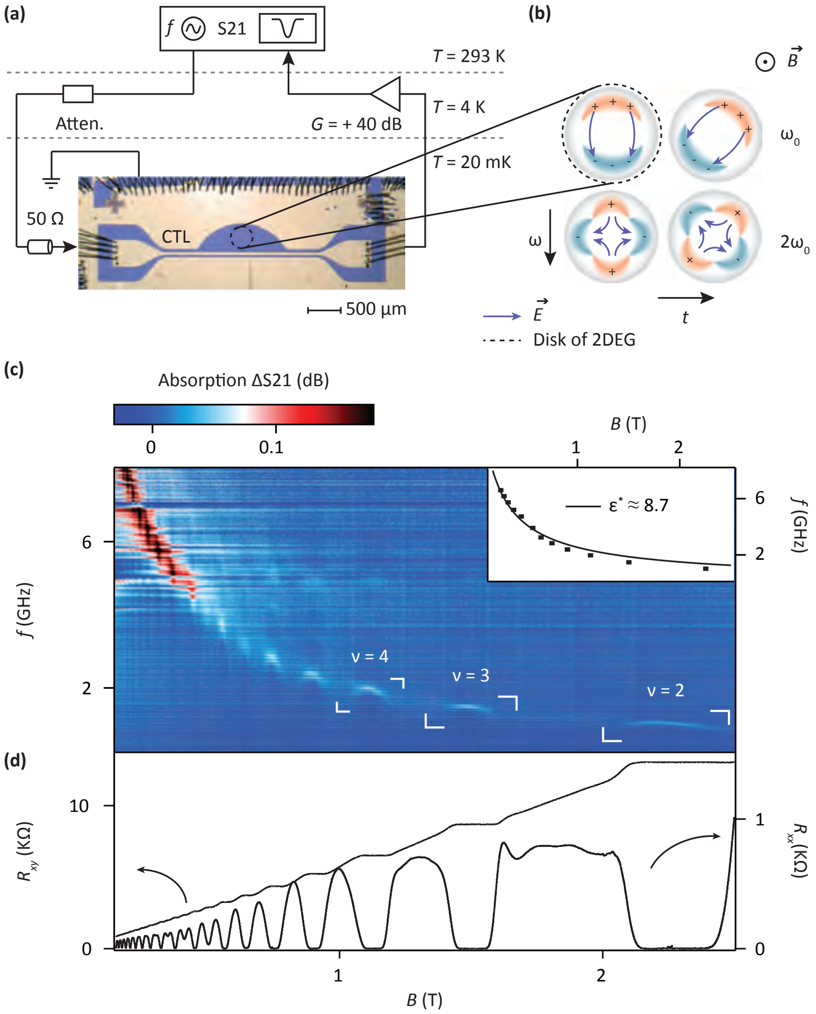

Figure 6.1: Microwave coupling into a quantum Hall disc. **(a)** Experimental setup including photograph of a coplanar transmission line device similar to that used to perform measurements coupled to a 350 μm etched disc of 2DEG (black dashed circle) at fridge temperature $T = 20$ mK. A vector network analyser is used to excite EMP modes across a wide frequency range and microwave absorption is measured as the ratio of the amplified output to input signal (S_{21}) from the CTL. **(b)** Illustration of the fundamental (top row) and first harmonic (bottom row) EMP modes as they evolve with time, where ω_0 is the fundamental mode and $2\omega_0$ the first harmonic (adapted from [50]). Charge distributions and electric fields $\vec{E}$ are indicated schematically. An external magnetic field B applied to the device points out of the page. **(c)** EMP spectrum of the quantum Hall disk showing absorbed microwave power as a function of frequency and magnetic field. Data has had a background, obtained at high field, subtracted. Inset shows the position of absorption dips at integer quantum Hall filling factors. Black line is a fit that allows an average effective dielectric constant of $\epsilon^* \approx 8.7$ to be extracted, consistent with excitations of an edge-state in GaAs (see Appendix B). **(d)** Transverse (R_{xy}) and longitudinal (R_{xx}) Hall resistance measurements taken at $T = 20$ mK on a Hall bar proximal to the microwave disk. The 2DEG is 270 nm below the surface with carrier density n$_s$ = 1.1 x 10^{11} cm^{-2}, and mobility $\mu = 5.2$ x 10^6 cm^2/Vs.

6.1.2 3-Port circulator

To test if these edge magnetoplasmons support the non-reciprocal transmission of microwaves, we implement a standard circulator configuration, with 3 ports arranged at 120-degree intervals around a disk of 2DEG (330 μm diameter), as shown in Fig. 6.2 (a) and 6.2 (b). For a single edge at high magnetic field, a voltage applied to a port capacitance induces an orthogonal current in the edge-state, with an impedance of the order of the inverse conductance quantum ($\sim$ 26 kΩ). Given our present measurement setup uses electronic components with a characteristic impedance of $Z_0 \sim 50~\Omega$, we have added an impedance matching circuit to enhance the response of each port. This network comprises a series chip-inductor $L = 47$ nH in resonance with the stray capacitance C_{stray}. Further reduction in insertion loss can be achieved by engineering the circulator dimensions, material or characteristic line impedance to achieve better matching [139, 140, 141] (see Appendix B for detailed discussion). The circulator is also embedded in a reflectometry configuration (Fig. 6.2 (c)) that enables a measurement of the port reflection as well as port transmission coefficient, from which dissipation can be estimated. As a control we first measure all microwave S-parameters at zero magnetic field, observing that all directions and ports are equivalent, as shown in Fig. 6.2 (d). An overall frequency-dependent, but reciprocal response can be associated with the impedance matching network, with matching frequency set to $1/\sqrt{LC_{\text{stray}}} \sim 1$ GHz. All subsequent measurements are normalised relative to this zero-field transmission response.

Turning to our key result, Fig. 6.3 shows the full transmission response of the 3-port circulator in the presence of a magnetic field that breaks time-reversal symmetry. Similar to the EMP spectrum of Fig. 6.1 (c), we first observe the presence of EMPs which enhance the transmitted power at certain frequencies, broadly following an approximate $f \sim B^{-1}$ dispersion relation, as is seen in Fig. 6.3 (a) (S_{13}) and 6.3 (b) (S_{31}). Strikingly, there are regions of the spectrum where the transmitted power appears to flow in either a forward or reverse direction with respect to the chirality of the edge. Particularly apparent are the crescent-shaped features that switch from forward to reverse transmission at distinct frequencies. This phenomenon, with a peak near the fundamental frequency of the EMP mode and a dip near the first EMP

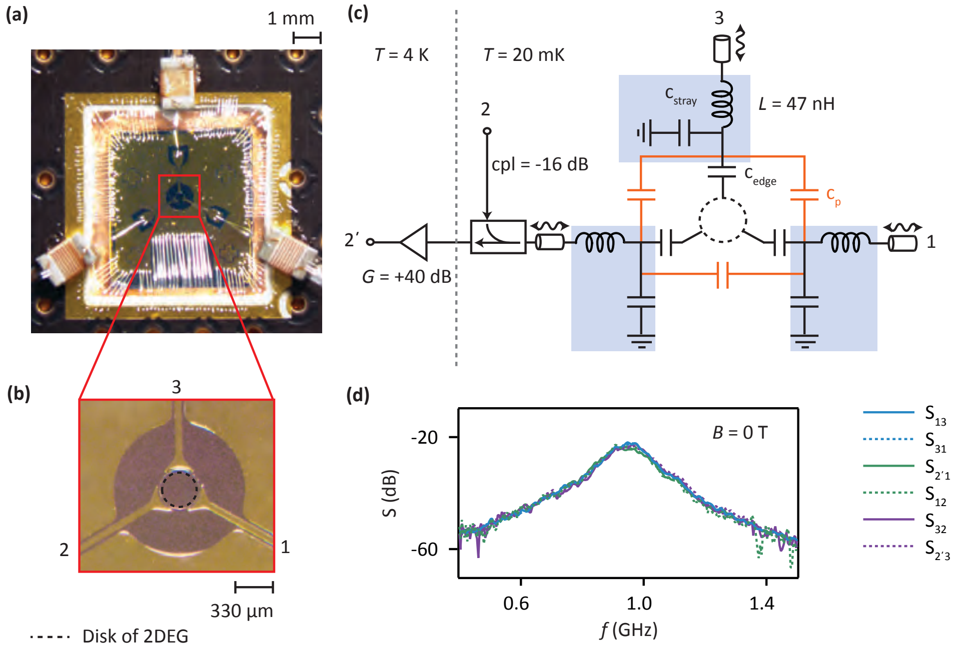

Figure 6.2: 3-Port circulator setup. **(a)** Photograph of circulator device showing the three coplanar transmission lines connected to copper wire-wound chip inductors for impedance matching. **(b)** Close-up of false-coloured photo of the circulator showing 330 μm diameter 2DEG disc with a 20 μm gap to the metal defining the three signal ports. **(c)** Circuit schematic of the experimental setup indicating port-to-edge capacitive coupling $C_{\rm edge}$ and direct parasitic coupling between ports $C_{\rm p}$. Resonant ($LC_{\rm stray}$) matching circuits are indicated with blue boxes. The input of port 2 passes through a directional coupler, with the reflected signal coupled to the output line (denoted $2'$) and amplified at 4 K. **(d)** Full 6-way transmission response of the circulator at zero magnetic field, with S-parameter measurements indicating complete reciprocity and a frequency response that arises from the matching networks. For each port the measured response of the amplifiers, couplers and cold attenuators in the circuit have been subtracted.

harmonic, is seen for all S-parameters in the chiral (clockwise) direction of the 3-port device (see solid lines in Fig. 6.3 (d)).

To measure the extent of non-reciprocity in our circulator, Fig. 6.3 (c) shows the difference between forward and reverse power by subtracting S_{31} from S_{13}. Unlike the $B = 0$ data shown in Fig. 6.2 (d), we now observe a strong directional dependence in the isolation between ports, that approach 40 dB at particular frequencies and magnetic fields (Fig. 6.3 (f)). Alternatively, we can also test for non-reciprocity by comparing the response of signals from two different inputs of the circulator to a common output. Since the device is geometrically symmetric, the response from the separate paths $S_{2'1}$ and $S_{2'3}$ are the same at $B = 0$, (see Fig. 6.2 (d)). In the presence of a magnetic field however, Fig. 6.4 shows that these paths are no longer equivalent, but depend rather on the direction of the field. This is evident in the data since blue and red features are not mirrored about $B = 0$.

Comparing the microwave response of the circulator to independent quantum Hall transport data suggests two distinct regimes. Between integer filling factors, where R_{xx} is maximised in transport, there is a large non-reciprocity in the microwave response, but also likely strong dissipation. Contrasting these broad regions are narrow crescent-shaped features that occur at fields corresponding to integer filling. These narrow features are particularly strong at frequencies near twice the fundamental EMP resonance. Again, overlaying these features with transport measurements indicates they align with minima in R_{xx}, where dissipation is suppressed. A direct and accurate measurement of the microwave dissipation is challenging in the regime where the impedance of the device is mismatched. Nevertheless, by accounting for the transmitted and reflected signal power we find the dissipation to be a few percent, consistent with the value of ~ 1 % given by our model (discussed below).

6.2 Discussion and model

We account for the distinct features in our measurements, as well as the phenomena of forward and reverse circulation via a simple picture of a Fano-like resonance. Figure 6.5 illustrates the phenomenology of the quantum Hall circulator. Similar to the operation

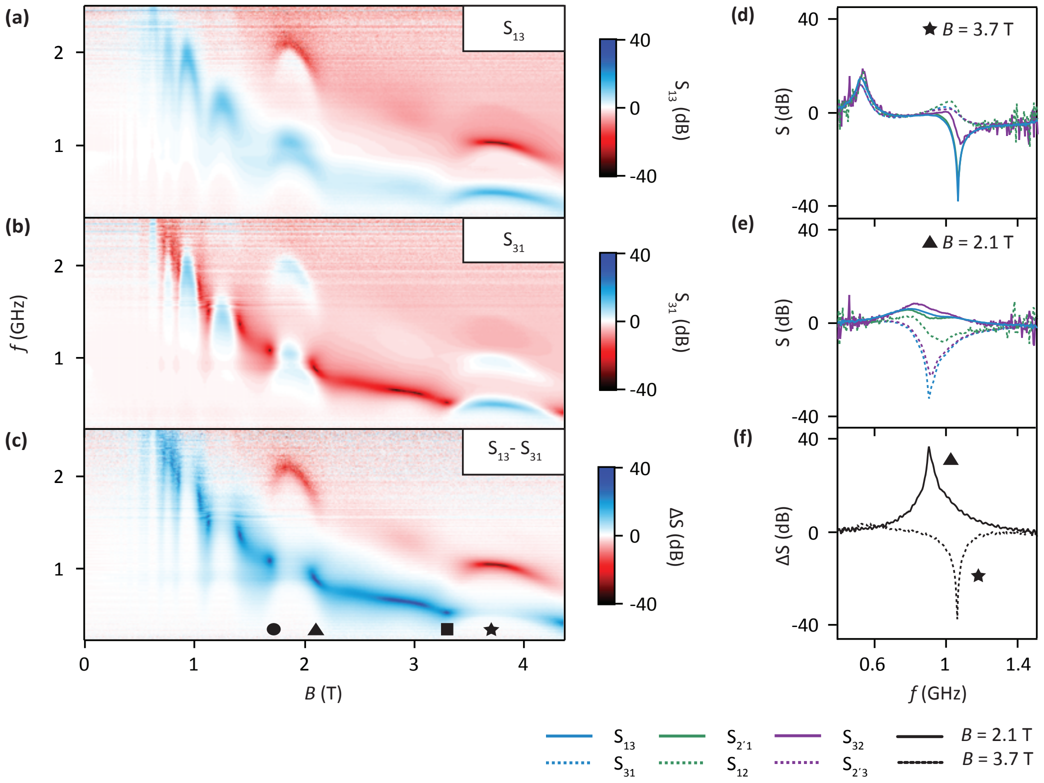

Figure 6.3: S-Parameter response across magnetic field. **(a)** and **(b)** Port transmission S_{13} and S_{31} with frequency and magnetic field. All measurements have been normalised to the gain-corrected background at $B = 0$ (shown in Fig. 6.2 (d)), which defines the 0 dB point on the colour scale. **(c)** Microwave response $S_{13} - S_{31}$ showing strong frequency and B-dependent non-reciprocity. **(d)** and **(e)** Full combination of transmission S-parameters, taken at B-fields indicated by the symbols in **(c)**. **(f)** Cuts through the colour scale data in **(c)**, demonstrating forward and reverse circulation.

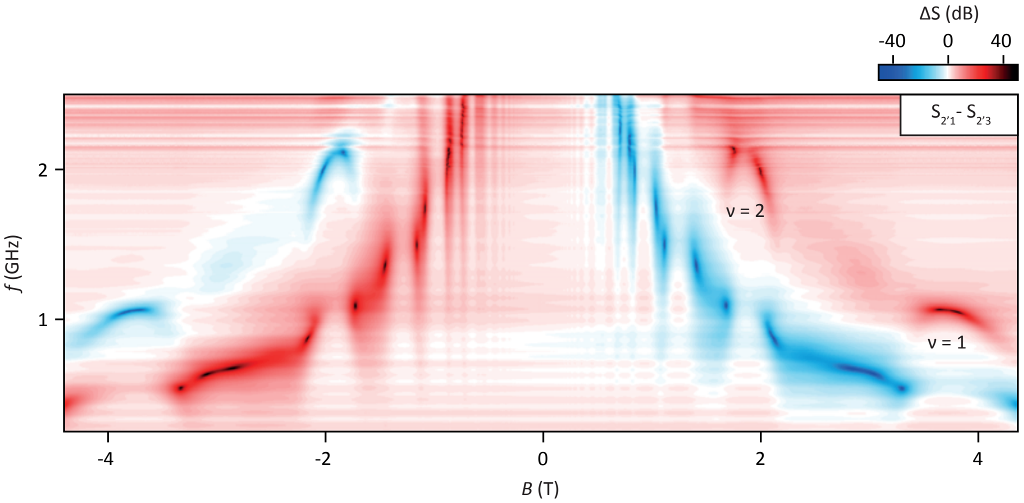

Figure 6.4: Non-reciprocal forward transmission. Isolation, $\Delta S = S_{2'1}$-$S_{2'3}$, measured at positive and negative magnetic fields. Note that the positions of features are symmetric about the $B = 0$ axis, but with opposite sign ΔS.

of a traditional ferrite device, we consider a resonator structure with two interfering paths, as shown in Fig. 6.5 (a). The arms of this interferometer comprise a direct path, supported by the parasitic (geometric) capacitance C_p between ports, and an indirect path C_edge, that capacitively couples ports via the plasmonic excitation of a quantum Hall edge. Key to the operation of our circulator is this 'slow light' response of the EMP modes, which, travelling at velocities 1000-times slower than the microwaves in the direct path, acquire the same phase over a length scale that is 1000-times shorter than the microwave wavelength in the dielectric. Considering these two-paths we note that there will be a frequency near the EMP resonance, at which the phase acquired via the edge leads to complete destructive interference with the signal propagating via the direct path. Given the chirality of the EMP, the condition for destructive interference will be dependent on the direction of microwave transmission, producing a non-reciprocal response between adjacent ports. Take for instance, the case where signals from port 3 to 1 propagate clockwise via the edge capacitance C_edge and acquire a phase of π-radians with respect to the signal travelling via C_p. Interference of these signals isolates port 1, whereas reverse transport, from port 1 back to port 3 must continue in a clockwise direction, past port 2 and acquire a constructive phase of 2π over twice the length. Circulation in the opposite direction to the chirality of the edge can now be understood for frequencies in which a π-phase is acquired in the forward direction, but 2π-phase in reverse.

We construct a simple model based on this Fano-like picture of interfering paths [128], by modifying the standard response of a three-terminal Carlin circulator to account for transport via a quantum Hall edge (see Appendix B). This yields an expression for the non-reciprocal admittance matrix of the edge, Y_{edge}, as was done in Ref. [123]. Extending the model in Ref. [123], we add an additional admittance term Y_{p} to account for a direct parasitic coupling C_{p} between terminals (see Fig. 6.2 (c)). We further include the possibility of dissipation R, either directly in the chiral EMP mode or elsewhere in the circuit. Given an admittance of the edge-state Y_{edge}, the total admittance is then given by:

$$Y_{\mathrm{total}} = (I + RY_{\mathrm{edge}})^{-1} Y_{\mathrm{edge}} + Y_{\mathrm{p}}$$

where I is the identity matrix and where

$$Y_{\mathrm{p}} = \begin{pmatrix} 2c & -c & -c \\ -c & 2c & -c \\ -c & -c & 2c \end{pmatrix}$$

with $c = i\omega C_p$ and ω is the angular frequency of the microwaves. Microwave S-parameters can then be calculated as a function of ω for a given characteristic impedance of the input port (Z_0).

This model qualitatively captures the mechanism of circulation as arising from the interference of the parasitic and quantum Hall edge paths. Despite its simplicity, we find it also accounts for many of the features seen in the experimental data, including forward and reverse circulation that occurs near the fundamental and first harmonic of the EMP mode, as shown in Fig. 6.5 (c) and 6.5 (d). For features that occur at fields corresponding to integer filling, we find good agreement with the data for parameter values that are consistent with the device geometry and independent transport measu-

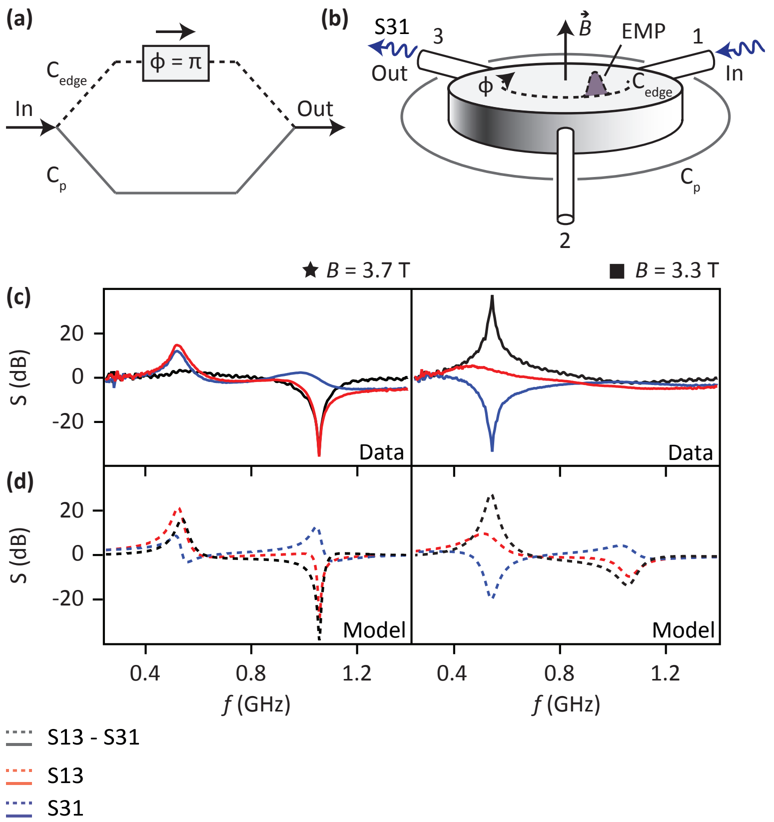

Figure 6.5: Comparison of data and model. **(a)** and **(b)** Proposed interferometric mechanism underlying the operation of the quantum Hall circulator, with a slow plasmonic path, via C_{edge}, and a direct capacitive path, via C_{p}. A non-reciprocal response between ports is produced for frequencies where the two paths are out of phase by $\phi = \pi$ in the forward direction and $\phi = 2\pi$ in the reverse direction. **(c)** and **(d)** Comparison of a simple model that captures this physics (top graphs), with experimental data (bottom graphs), at two different magnetic fields indicated by the symbols (with respect to Fig. 6.3 (c)). The model is described in detail in Appendix B with parameters set to values $Z_0 = 50$ Ω, $C_{\mathrm{p}} = 315$ fF, $C_{\mathrm{edge}} = 127$ fF, $R_{xy} = 5000$ Ω with $R = 80$ Ω in the centre of an EMP resonance (star symbol) and $R = 350$ Ω off resonance (square symbol). Note that the impedance matching network transforms $R_{xy} = 25$ kΩ towards a few kΩ, consistent with the value used in the model.

rements (see Fig. 6.5 caption for details). At magnetic fields slightly away from integer filling, increasing R in the model yields similar results to the observed phenomena.

6.3 Tunable non-reciprocity

Finally, having outlined the mechanism leading to non-reciprocity in our device, we turn to describe a new mode that has no analog in the operation of classical circulators but may enable reconfigurable passive routing of microwave signals on-chip using gate voltages to modulate the velocity of EMPs. To demonstrate this mode we make use of an alternate device (Fig. 6.6 (a)) where, in comparison to the previous device, the port electrodes are positioned to now overlap the edge and a grounded contact is added to the centre of the disk. Sweeping the magnetic field, we find this device exhibits regions of strong non-reciprocity, as shown in Fig. 6.6 (b). Tunable non-reciprocity is demonstrated at fixed negative B-field by sweeping the dc voltage applied to the port-2 gate V_{g2}. This adjusts the response between the source and sink ports 3 and 1 respectively, which tunes the frequency of isolation $\Delta S = S_{13}$-S_{23} as shown in 6.6 (c) and 6.6 (d). Applying a voltage to a gate hardly modifies the total path length of the EMP in this geometry, but can lead to a significant modulation in its velocity by varying the carrier density, electric field, or extent of screening at the disk boundary [132, 142]. As a function of V_{g2}, Fig. 6.6 (c) shows that the non-reciprocal response of the circulator initially drops from $\sim$ 1.2 GHz to $\sim$ 0.8 GHz as the gate voltage is initially applied, followed by a more gradual decrease in the centre frequency as the gate is made increasingly negative. At present we do not understand why a modest gate voltage leads to a significant velocity modulation and therefore frequency response over such a large bandwidth (exceeding 1 GHz and many line-widths in this device). An alternate means of reconfiguring the device can be achieved by adjusting the external magnetic field (as shown in the Appendix B). In this way the circulator can produce forward or reverse circulation, selectively routing microwave packets to alternate ports depending on the value of the magnetic field.

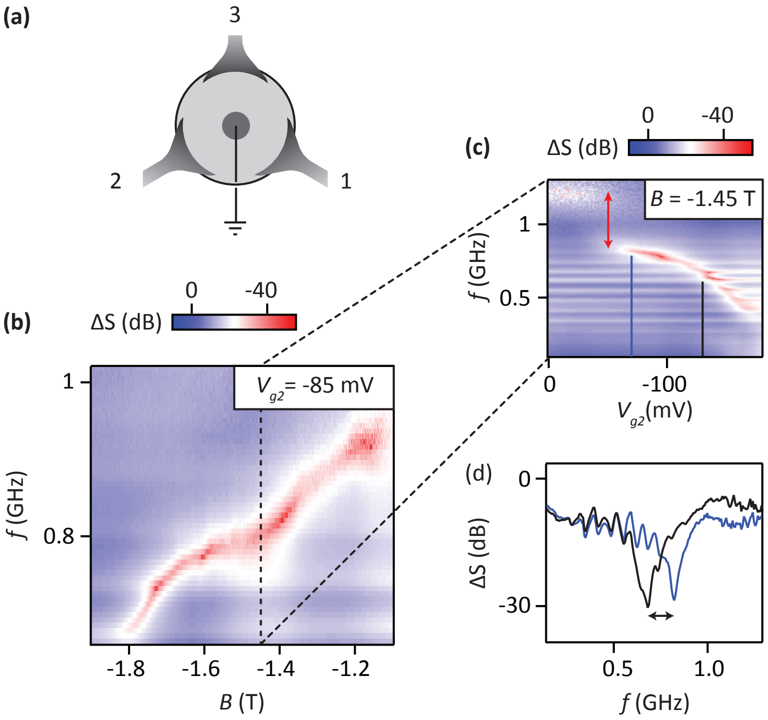

Figure 6.6: Tuning path non-reciprocity with an electrode gate. **(a)** Schematic of the gate-tunable device, with ports overlapping the edge of the disk and a grounded contact on the mesa. Bias tees enable the application of both rf and dc voltages. A large non-reciprocity $\Delta S = S_{13}$-S_{23} is observed as a function of magnetic field, as shown in **(b)** for the case V_{g2} = -85 mV. At fixed negative magnetic field values, varying V_{g2} is found to affect the path from ports 3 to 1 and produces a significant modulation in the frequency response of the circulator (shown in **(c)** and **(d)**). This response is mirrored with a change of sign ΔS at positive magnetic field values, where the direction of EMP propagation is reversed and V_{g1} is varied (see Appendix B). Red arrow in **(c)** indicates a discontinuous jump in frequency as a gate voltage is first applied, while vertical lines show the positions of 1D cuts presented in **(d)**. Horizontal striations in **(c)** are the result of small standing waves associated with an impedance mismatch between the amplifier and device.

6.4 Conclusion

We conclude by noting that in this context, an edge-state can be considered as a mesoscale delay-line with dynamic, and gate-tunable wideband response. Such a dependence opens the prospect of compact, parametric devices such as amplifiers, non-reciprocal filters and mixers based on the plasmonic and chiral response of the quantum Hall effect. Indeed, such modes can also likely be realised at zero magnetic field using topological insulator devices that exhibit the quantum anomalous Hall effect [45].

6.5 Acknowledgements

We thank D. DiVincenzo, C. Nayak, and J. Cano for useful conversations. This research was supported by Microsoft Research, the US Army Research Office grant W911NF-14-1-0097, and the Australian Research Council Centre of Excellence Scheme (Grant No. EQuS CE110001013).

6.6 Author contributions

D.J.R. devised the project. A.C.M., J.I.C, J.M.H. and S.J.P. carried out the experiments. J.D.W. G.C.G. and M.J.M. grew the materials. A.C.D., J.I.C, S.J.P. and A.C.M. worked on the theory and model. D.J.R, A.C.M., A.C.D., and J.I.C. wrote the paper.

6.7 Author affiliations

[1]ARC Centre of Excellence for Engineered Quantum Systems, School of Physics, The University of Sydney, Sydney, NSW 2006, Australia.
[2]Station Q Sydney, The University of Sydney, Sydney, New South Wales 2006, Australia.
[3]Department of Physics and Astronomy, Purdue University, West Lafayette, Indiana 47907, USA.
[4]Birck Nanotechnology Center, School of Materials Engineering and School of Electrical and Computer Engineering, Purdue University, West Lafayette, Indiana 47907, USA.

[5]Station Q Purdue, Purdue University, West Lafayette, Indiana 47907, USA.

7

Zero-field edge magnetoplasmons in a magnetic topological insulator

*Incorporating ferromagnetic dopants, such as chromium [45, 143, 144] or vanadium [145], into thin films of the three-dimensional (3D) topological insulator (TI) (Bi,Sb)$_2$Te$_3$ has recently led to the realisation of the quantum anomalous Hall effect (QAHE), a unique phase of quantum matter. These materials are of great interest [38, 146], since they may support electrical currents that flow without resistance via edge channels, even at zero magnetic field. To date, the QAHE has been investigated using low-frequency transport measurements [45, 143, 144, 145, 147]. However, transport requires contacting the sample and results can be difficult to interpret due to the presence of parallel conductive paths, via either the bulk or surface [45, 147], or because additional non-chiral edge channels may exist [143, 148, 149]. Here, we move beyond transport measurements by probing the microwave response of a magnetised disk of Cr-(Bi,Sb)$_2$Te$_3$. We identify features associated with chiral edge-magnetoplasmons (EMPs), a signature that robust edge-channels are indeed intrinsic to this material system. Our results provide a measure of the velocity of edge excitations without contacting the sample, and pave the way for a new, on-chip circuit element of practical importance: the TI, zero-field microwave circulator.**.

---

*This Chapter is adapted from A. C. Mahoney[1], J. I. Colless[1], L. Peeters[2], S. J. Pauka[1], E. J. Fox[2,3], X. Kou[4], Lei Pan[4], K. L. Wang[4], D. Goldhaber-Gordon[2,3], and D. J. Reilly[1,5], "Zero-field Edge Mag-

7. ZERO-FIELD EDGE MAGNETOPLASMONS IN A MAGNETIC TOPOLOGICAL INSULATOR

It is now understood that ferromagnetism, by lifting spin degeneracy and breaking time reversal symmetry at zero magnetic field, can transform a topological insulator (TI) into a new phase of matter that hosts chiral edge states [43, 44, 150, 151, 152]. The signature of this phase is the quantum anomalous Hall effect (QAHE), in which the transverse conductance of a magnetised Hall bar remains quantised in units of the conductance quantum, even in the absence of an external magnetic field. Given that bulk insulators and ferromagnets are commonplace at room temperature, there is optimism that the QAHE may not be limited to the cryogenic regimes of today's experiments. A room-temperature QAHE in which edge states propagate without dissipation could impact some of the challenges facing current-generation high speed integrated circuits. The presence of robust edge states in these material systems also opens the prospect that they support EMP excitations, resonant drum-modes of the electron gas that are well-known in the context of the quantum Hall effect [50, 52, 153]. These resonant modes typically occur at microwave frequencies, and are distinct from the predicted plasmonic phenomena of TI materials near optical frequencies [154]. Beyond their fundamental interest, the velocity of EMP excitations is typically reduced compared to the speed of light, making them ideal platforms for constructing on-chip delay networks, high-impedance transmission lines, and non-reciprocal devices such as gyrators and circulators needed for quantum information processing [123, 139, 155].

Here we investigate the zero-field magneto-plasmonic response of a magnetised, contactless disk of the ferromagnetic TI Cr-$(Bi,Sb)_2Te_3$. The fabrication of both Hall bars and resonant disk structures enables us to make a one-to-one comparison between transport data and the microwave excitation spectrum of the material. By implementing a three-port circulator configuration, we show that the low frequency plasmon response exhibits non-reciprocal behaviour, consistent with chiral EMPs. The existence of EMPs in the disk and their correspondence with a minimum in the longitudinal resistance of the Hall bar provide further convincing evidence that this system supports a robust edge state. Finally, we examine the dependence of circulation on excitation power and temperature, suggesting that microwave measurements can serve as a sensitive probe of the conditions at the edge.

---

netoplasmons in a Magnetic Topological Insulator", *ArXiv preprint*, arXiv:1703.03122 (2017).

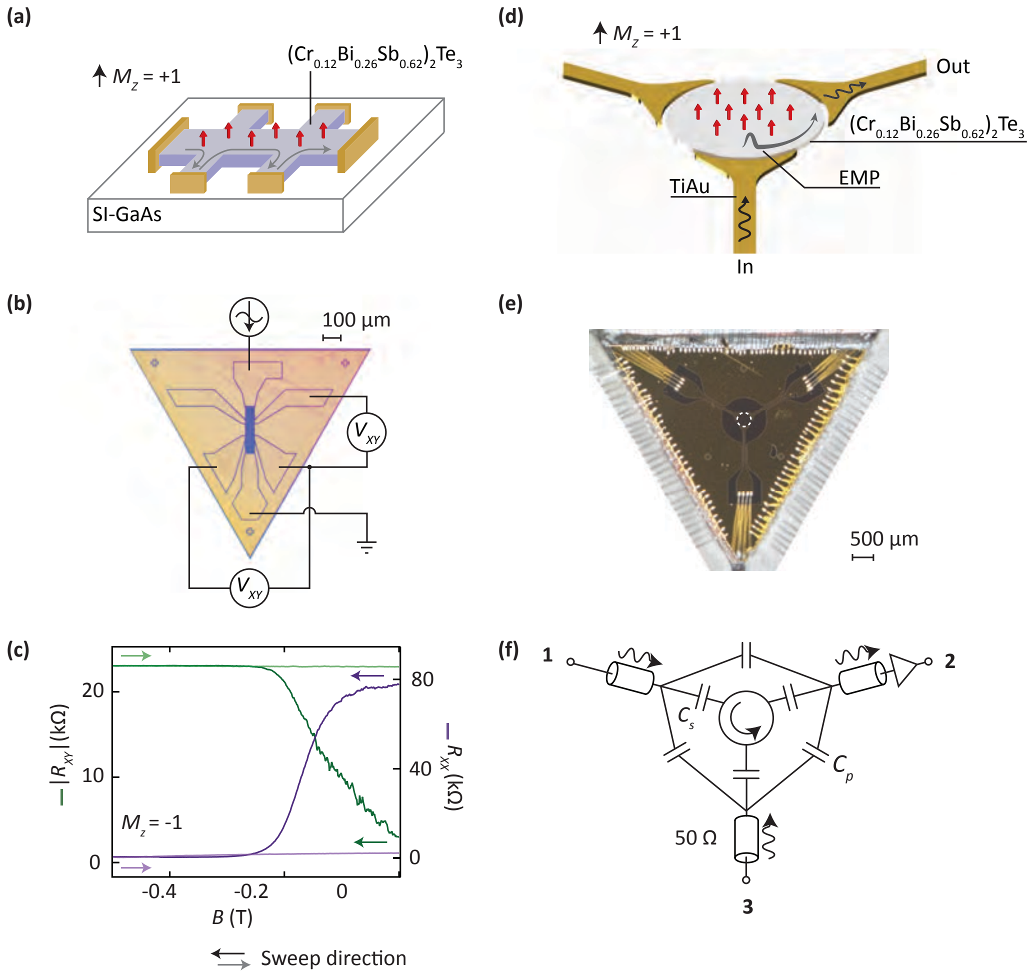

Figure 7.1: Experimental set-up. **(a)** Illustration of the quantum anomalous Hall effect in a three-dimensional topological insulator thin film with ferromagnetic dopants. **(b)** Photograph of a Hall bar fabricated on a device with seven quintuple layers of $(Cr_{0.12}Bi_{0.26}Sb_{0.62})_2Te_3$ grown epitaxially on a GaAs substrate. Standard lock-in techniques are used to measure the transport properties of the material. **(c)** Transverse and longitudinal resistance (R_{xy} and R_{xx}) as the perpendicular magnetic field is swept out to -0.5 T (dark coloured lines), and then back to zero field (light shaded lines). **(d)** Cartoon of a three-port circulator device with a magnetic topological insulator. **(e)** Photograph of the circulator device. **(f)** A circuit schematic for the experimental setup. The parasitic capacitances between port electrodes (C_p) and from the ports to the EMP modes (C_s) are indicated. Port 2 is connected to a low-noise cryo-amp operating at 4 K, allowing measurement of S_{21} and S_{23} through a common output line.

7.1 Experimental Setup

Turning to the experimental setup shown in Fig. 7.1, the magnetic three-dimensional (3D) TI used to make the circulator and corresponding Hall bar is seven quintuple layers of $(\mathrm{Cr}_{0.12}\mathrm{Bi}_{0.26}\mathrm{Sb}_{0.62})_2\mathrm{Te}_3$. The film is grown on a semi-insulating (111)B GaAs substrate by molecular beam epitaxy, then capped with alumina to protect the surface. To define the microwave circulator, we use photolithography to pattern a circular, 330 μm diameter mesa and etch away the remaining film via Ar ion milling (see Appendix C). We next pattern capacitive contacts and a ground plane, depositing 120 nm Au with a Ti sticking layer by e-beam evaporation. The contacts are designed to be 20 μm away from the mesa edge.

7.2 Initial Magnetisation Sequence

Starting at zero field, the transport data in Fig. 7.1 (c) show the longitudinal and transverse resistances of the Hall bar, R_{xx} and R_{xy}, during the initial magnetisation sequence, sweeping the field from zero to -0.5 T at the cryostat base temperature of T = 20 mK (dark purple and green lines). As the field is applied for the first time we observe R_{xx} drop from $\sim$ 80 kΩ to $\sim$ 500 Ω as R_{xy} increases towards the resistance quantum = h/e^2 (h is Planck's constant and e the electron charge). After waiting several hours the field is swept back to zero, with transport data in this direction shown as lightly-shaded lines in Fig. 7.1 (c). Following this initial magnetisation sequence, we observe the signatures of the QAHE, namely that R_{xx} remains near zero and R_{xy} does not vary by more than 1%. An accurate and precise measurement of R_{xy} requires accounting for possible geometric effects of the contacts and calibration using a known resistance standard, as was done in Ref. [147]. In the absence of these corrections, the measured resistance plateau value of 25750 Ω is within the uncertainty expected for the quantum of resistance, 25813 Ω [45, 143, 144].

We compare these transport data with the microwave response of an etched TI disk on the same material, configured as a circulator as shown in Fig. 7.1 (d-f). Similar designs comprising an rf excitation and detection port have been used to probe EMPs in the quantum Hall effect regime in GaAs semiconductors [135, 136, 155] and in graphene [132, 133, 134]. These EMP modes are charge density waves supported by edge channels

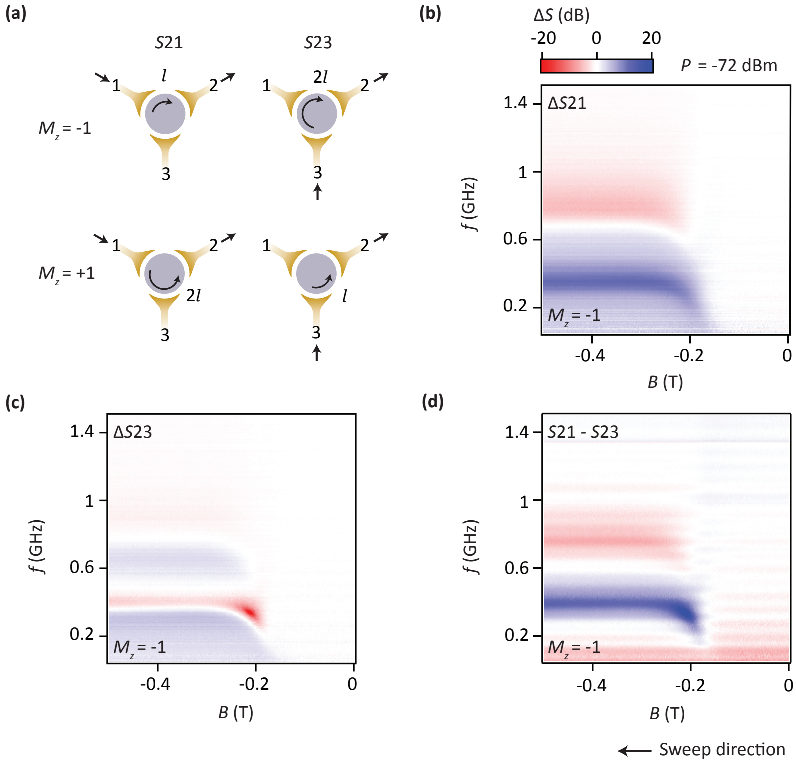

Figure 7.2: Initial magnetisation response. **(a)** Illustration of chiral edge transport in a circulator setup for different magnetisation and port configurations. Arc path lengths are denoted as l and $2l$. **(b)** and **(c)** show the microwave response of signals excited from ports 1 and 3 and amplified out of port 2, as the magnetic field is varied. These traces have been normalised to the reciprocal background prior to sample magnetisation. Isolation $S_{21} - S_{23}$ is shown in **(d)**, where the difference between the bare S-parameter traces is plotted without background normalisation. Past the coercive field of -0.16 T, strong non-reciprocity is observed at two distinct frequency bands, with opposite amplitudes.

at the boundary of the material. For traditional semiconductor samples, such as GaAs, the propagation velocity and therefore microwave frequency response of the EMP is set by the ratio of the electric and magnetic field at the edge. To what extent this picture holds true for TI materials remains an open question motivating our work.

7.3 3-port circulator configuration

In our setup, a 3-port design further allows the non-reciprocal character of the device to be probed by determining whether the signal traverses the TI disk via a left-handed or right-handed path [123, 155]. The experiment comprises S-parameter measurements in which the amount of microwave power transmitted from port 1 to port 2 (S_{21}), or port 3 to port 2 (S_{23}) is detected as a function of external magnetic field and magnetisation state ($M_z = M/|M| = \pm 1$) of the TI disk (see Fig. 7.2 (a)). The two symmetrical paths, port 1 to 2 and port 3 to 2, are designed to be equivalent in the absence of chiral transport.

We note that for any measurement, microwave power can be coupled directly and reciprocally between the ports via the geometric (parasitic) capacitance that shunts the disk (C_p in Fig. 7.1 (f)). In our sample geometry C_p is estimated to be in the vicinity of a few hundred femto-Farads [155]. The combination of a direct capacitive path in parallel with the conductive edge-channels in the disk creates an interferometer in which signals travel at the speed of light in the capacitive arm, and at a velocity in the other arm that is determined by the magnetoplasmonic response [155]. It is primarily the difference in velocities (and, to a lesser extent, path lengths) between the two paths of the interferometer that yields a phase offset between the two signals when they recombine at the receiving port. Further, the amplitude of the signals is set by the impedances of the two paths; if the EMP resonator has a moderate Q-factor, these amplitudes can easily be made comparable by driving the circuit at a frequency slightly detuned from the resonant mode of the EMP. Within this interference picture, the response of the circuit can be interpreted as a Fano resonance that depends on the length of path travelled by the EMP, l or $2l$ depending on the excitation port and magnetisation direction (see Fig. 7.2 (a)). With port 2 always set to be the receiving port, transmitting power from port 1 or port 3 thus configures the edge length to be

l or $2l$. The difference between the two paths' transmission, measured as $S_{21} - S_{23}$, determines the isolation or non-reciprocity of the circuit.

We begin the presentation of the circulator data in a similar fashion to the transport measurements, starting at zero magnetic field and recording S_{21} and S_{23} as the external field is stepped out to -0.5 T. To enable a direct comparison between transport and the microwave response of the disk during the one-off magnetisation sequence, we acquire transport data as well as S_{21} and S_{23} at a fixed magnetic field before stepping the field (i.e., all data in Fig. 7.1 (c) and Fig. 7.2 were obtained concurrently). All individual S_{21} and S_{23} data throughout the paper are normalised (denoted by Δ) by subtracting the initial frequency dependence of the signal in logarithmic units (dB) in the unmagnetised state, $B = 0$ and $M_z = 0$, where the response is reciprocal. This calibration trace is taken at cryostat base temperature ($T \sim 20$ mK) and a port excitation power of -72 dBm. This normalisation alleviates frequency-dependent artefacts, for instance transmission oscillations due to line impedance mismatch that do not evolve with magnetic field (see Appendix C for further details).

Forward transmission ΔS is shown in Fig. 7.2 (b) and 7.2 (c) as a function of frequency and magnetic field for the two paths S_{21} and S_{23}. As the sample begins to magnetise at the coercive field ($\sim$ -0.16 T), we observe resonance-like dips and peaks in the frequency spectrum of the disk, evident as red and blue coloured horizontal bands appearing at the field strength where R_{xy} (Fig. 7.1 (c)) approaches the resistance plateau h/e^2. This is the microwave signature of the QAHE. Compared with EMPs in 2 dimensional electron systems [155] where the frequency ω_{EMP} is proportional to $1/B$, in the TI we observe a flat dispersion as a function of magnetic field, centred at the fundamental mode of the EMP, near 400 MHz. This is consistent with dc transport measurements of the Hall resistance which takes on a constant, quantised value after the sample is magnetised. Measuring the frequency at which these resonances occur in combination with the circumference of the TI disk gives an EMP velocity at the fundamental mode of $\sim 4 \times 10^5$ m/s, similar to what is found in other structures comprising stacks of semiconductors [135, 136, 155].

The microwave response shows that the parameters S_{21} and S_{23} deviate from each

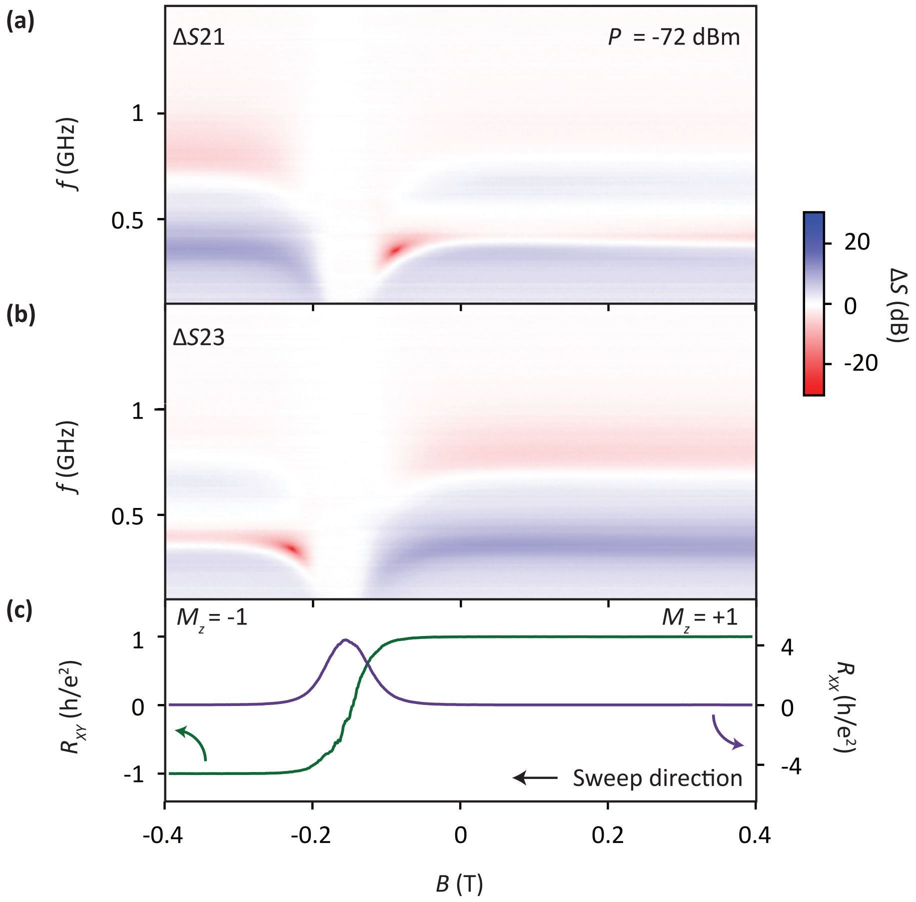

Figure 7.3: RF transmission parameters across positive and negative magnetisation directions. **(a, b)** Normalised ΔS_{21} and ΔS_{23} responses measured at the same time as transport data in **(c)**. A pre-magnetisation frequency-dependent background has been subtracted from each of the traces in **(a,b)**. **(c)** Transverse (green) and longitudinal (purple) dc resistances measured on a Hall bar as the magnetisation direction is swept from positive to negative. Away from the coercive field, raw R_{xy} approaches the resistance quantum while R_{xx} measures $\sim 500\ \Omega$.

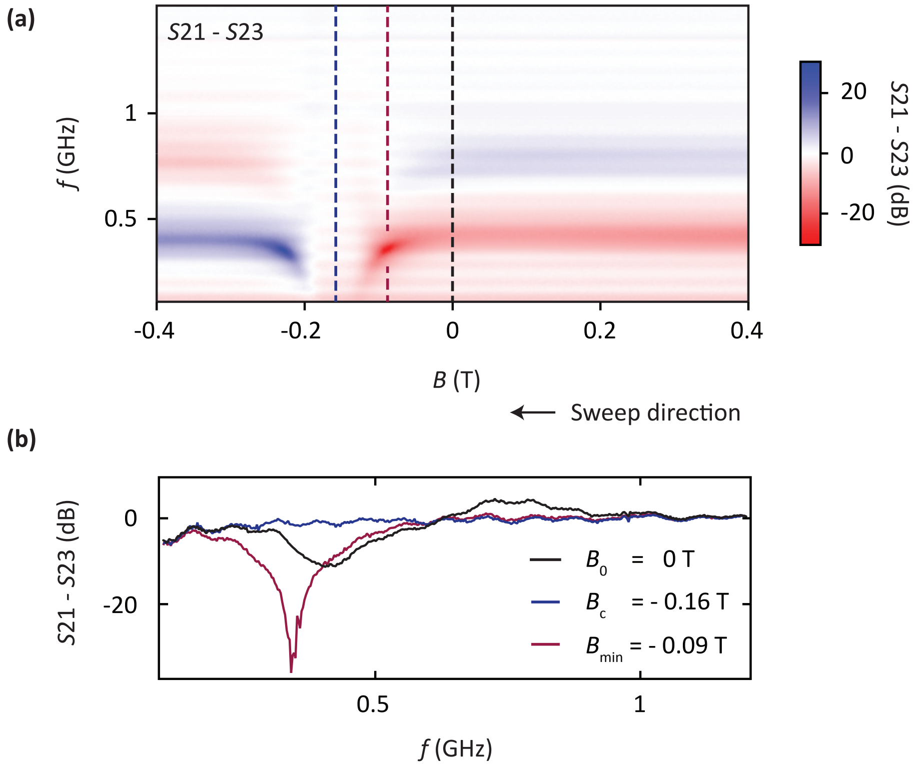

Figure 7.4: Microwave isolation at zero applied magnetic field. **(a)** Compares the difference between the bare S_{21} and S_{23} paths from Fig. 7.3, providing a measure of isolation in the system. **(b)** Shows cuts through **(a)** at zero applied magnetic field (B_0, black line), the coercive field (B_c, blue) and at the point where a power minimum is observed ($B_{\mathrm{m}in}$, mauve).

other as the disk becomes magnetised. This is a result of the non-reciprocity of the system, evident in Fig. 7.2 (d) where we have subtracted the bare S-parameters ($S_{21} - S_{23}$) from each other to show the difference between the two configurations of the circulator. Again, we interpret these measurements of S_{21} and S_{23} as characterising paths around the edge of the disk in the same (chiral) direction with arc length l and $2l$ (Fig. 7.2 (a)). Considering the measurement in Fig. 7.2 (d), it is apparent that microwave power can both circulate near the fundamental EMP frequency (blue frequency band) and ‘counter circulate’ in an opposite direction near the first harmonic (red frequency band). This behaviour is also observed for GaAs devices in the quantum Hall regime [155] and is understood to arise from a Fano-like interference between the slow-velocity resonantly circulating edge mode and the less frequency-sensitive parallel capacitive path [140]. We remark that the observation of circulation and counter-circulation is a further signature of the plasmonic response of the chiral edge state.

7.4 Zero-field response

The quantum anomalous Hall effect is unique in that it supports a robust chiral edge state at zero applied field [147]. To examine the zero-field response of the magnetised TI system, we continue to take transport measurements on the Hall-bar concurrent with S-parameter data on the circulator, as the system is swept from positive to negative field through zero, as shown in Fig 7.3 (a) and 7.3 (b). The transport data in Fig. 7.3 (c) show the familiar signature of the QAHE with R_{xx} peaking and R_{xy} switching sign at the coercive field indicated by the blue dashed line ($\sim$ -0.16 T). At $B = 0$, the system remains magnetised with R_{xy} reaching a maximum value of 25.75 kΩ.

In comparison to the transport measurements, the microwave response of the TI reveals new information. The response of the disk for each of the signal configurations, characterised by ΔS_{21} in the top panel and ΔS_{23} in the middle panel, is strongly asymmetric about the coercive field. Symmetry is restored, however, if in addition to the sign of the magnetic field the ports are also interchanged, so that the red band in ΔS_{21} on the left of the coercive field mirrors the red band in ΔS_{23} on the right, and vice versa for blue features. This strong non-reciprocity is most evident in the differential form of the data $S_{21} - S_{23}$, as shown in Fig. 7.4 (a). At zero field the circulator continues to exhibit non-reciprocity $\sim$ 10 dB (Fig. 7.4 (b)). Intriguingly, the device is maximally non-reciprocal at a field approaching the coercive field, producing a 'hot-spot' feature in the S-parameter response (mauve dashed-line Fig. 7.4 (a)). As described below, we suggest these features are linked to enhanced dissipation.

Finally, we investigate the temperature and microwave power dependence of the EMP spectra in an effort to better understand the details of the zero-field edge state. At $B = 0$ and with the TI magnetised ($M_z = -1$), ΔS_{21} and ΔS_{23} are measured as a function of applied microwave power P, as shown in Fig. 7.5 (a) and (b). In addition to the usual non-reciprocity at constant power, we observe an evolution in the non-reciprocal features with increasing P that is dependent on the length of the edge segment. While the response of ΔS_{21} (characterized by arc length l) begins to fade out at high powers, the amplitude of ΔS_{23} ($2l$) changes sign near the fundamental frequency and exhibits a pronounced minimum or hot-spot near P = -60 dBm. Interchanging the ports and repeating the measurement at $M_z = +1$ and $B = 0$ produces similar features in accordance with a reversal of chirality (see Appendix C). Mirroring the dependence with power, increasing the cryostat temperature also produces a change of sign relative to the pre-magnetised state for the longer edge path ($2l$): Raising T as in Fig. 7.5 (c) and (d) leads to ΔS_{21} becoming gradually washed out, while ΔS_{23} produces a hot-spot around T = 85 mK. This effect is further illustrated in Fig. 7.5 (e), where 1D cuts at constant power (top panel) or temperature (bottom panel) are shown for ΔS_{23}.

7.5 Power and temperature dependence

So-called hot-spots – strong decrease in the microwave power transmitted between ports – occur at particular magnetic fields, powers, or temperatures. Appealing to the phenomenology of the interferometer pictured in Fig. 7.1 (f), we note that the direction of power transmission between ports, either circulation or counter-circulation, is set by the relative phase and amplitude of the signals in the edge-state arm compared to the direct capacitive arm of the interferometer. In general, this picture accounts for the constructive interference of signals for the shorter edge path (l) and destructive interference for the longer ($2l$), when driving near resonance of the EMP fundamental. Extending this picture to include dissipation, we suggest that losses in either arm of

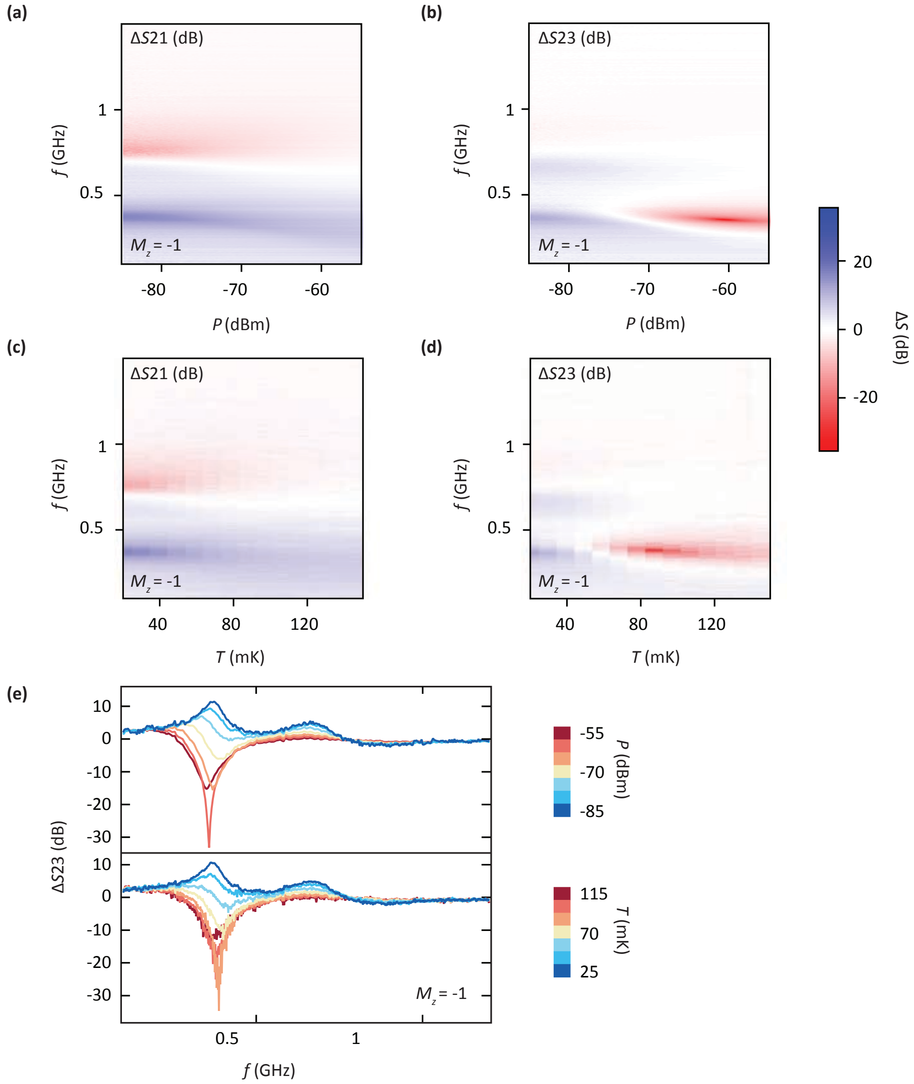

Figure 7.5: Effect of temperature and microwave power. **(a,b)** Show the frequency response ΔS_{21} and ΔS_{23} with increasing microwave power applied to the excitation port. For these measurements $T \sim 20$ mK. In **(c)** and **(d)** the dependence of ΔS_{21} and ΔS_{23} is measured as a function of cryostat temperature while the applied port power is kept low at -87 dBm. In **(a-e)** all data are taken at zero applied magnetic field after the sample has been magnetised with $M_z = -1$. Akin to Figures 7.2 & 7.3, the same pre-magnetisation background taken at constant power and cryostat base temperature is subtracted from each of the 2D plots. **(e)** Presents 1D cuts through the colour plots of ΔS_{23} in **(b)** and **(d)**. The top (bottom) panel depicts traces at constant power (temperature), showing the evolution of the Fano-like lineshape.

the interferometer can adjust the relative amplitudes. As noted above, the relative phase of the two paths is naturally tuned by π upon crossing the EMP resonance. At a frequency where the relative phase is π we might expect a sign change in the relevant S parameter response. In this way the hot-spots can be understood as regions where almost perfect cancellation between the two arms occurs. The appearance of dissipation in either path with increasing temperature, microwave power, or near the coercive field is perhaps not unexpected. Accounting for the microscopic mechanisms underlying such dissipation remains an open challenge [147, 148, 149, 156, 157, 158, 159], given that all measurements are well below both the Curie temperature of these ferromagnetic TIs (of order 10 to 20 K) and the energy scale of the exchange gap as measured by ARPES (of order 10 meV).

7.6 Conclusion

To conclude, we have probed the EMP spectrum of a magnetic topological insulator, comparing its microwave response to transport data. The measurement setup can be understood as an interferometer with the disk of TI in one arm of the interferometer and a parasitic capacitance in the other. Within this picture, the response of the system exhibits resonances that can be explained by accounting for the slow velocity of EMPs as they traverse an arc-length of the TI disk's edge rather than the bulk. In addition to the device examined, we have examined a second circulator, fabricated from a separately-grown wafer, and found it to exhibit strikingly similar behaviour in all aspects (see Appendix C). We suggest that this similarity between devices is related to the robust properties of the edge state, set by the non-trivial topology of the material system rather than, for instance, the specific configuration of microscopic disorder. Taken together, our microwave measurements provide strong evidence that this material system indeed supports robust, chiral edge states at zero magnetic field, opening the prospect of compact microwave components based on magnetic topological insulators.

7.7 Acknowledgements

We thank Andrew Doherty and David DiVincenzo for useful conversations. Device fabrication and preliminary characterisation was supported by the Department of Energy, Office of Science, Basic Energy Sciences, Materials Sciences and Engineering Division, under Contract DE-AC02-76SF00515. Microwave and transport measurements presented in the main text were supported by Microsoft Research, the Army Research Office grant W911NF-14-1-0097, the Australian Research Council Centre of Excellence Scheme (Grant No. EQuS CE110001013). Materials growth was supported by the DARPA MESO program under Contracts No. N66001-12-1-4034 and No. N66001-11-1-4105. Infrastructure and cryostat support were funded in part by the Gordon and Betty Moore Foundation through Grant GBMF3429. E. J. F. acknowledges support from a DOE Office of Science Graduate Fellowship. L. Peeters. was supported by a Stanford Graduate Fellowship.

7.8 Author contributions

D.J.R. and D.G.G devised the project jointly. J.I.C., A.C.M., L.Peeters, and S.J.P. carried out the experiments. Samples were fabricated by E.J.F. Materials were grown by X. K., Lei Pan, and K.W. The paper was written by D.J.R., A.C.M., and D.G.G, with input from all co-authors.

7.9 Author affiliations

[1]ARC Centre of Excellence for Engineered Quantum Systems, School of Physics, The University of Sydney, Sydney, NSW 2006, Australia.
[2]Department of Physics, Stanford University, Stanford, California 94305, USA.
[3]Stanford Institute for Materials and Energy Sciences, SLAC National Accelerator Laboratory, 2575 Sand Hill Road, Menlo Park, California 94025, USA.
[4]Department of Electrical Engineering, University of California, Los Angeles, California 90095, USA.
[5]Microsoft Station Q Sydney, Sydney, NSW 2006, Australia.

8

Conclusion and outlook

This Chapter reflects on the work presented in this thesis as a whole, and seeks to place the results within the context of the wider field. In particular, improvements in quantum Hall and quantum anomalous Hall circulator performance are first addressed with respect to recent theoretical proposals. Extensions of on-chip frequency multiplexing and dispersive gate sensing techniques are then discussed in relation to scalable quantum computing architectures across semiconductor-based and hybrid qubit platforms.

Recent years have witnessed accelerated progress within the condensed matter community towards realising semiconductor-based quantum machines. In constructing these systems, qubits are formed from the quantum mechanical degrees of freedom of isolated particles, and are manipulated via electric fields, or a combination of electric and magnetic fields. In particular, group IV (eg. Si and SiGe) or III-V (eg. GaAs and InAs) materials present an attractive route towards quantum computing due to the clean structures that can be grown, relative ease of qubit confinement, and the potential to leverage fabrication techniques from the semiconductor industry.

A key requirement for building a quantum computer is the ability to perform two-qubit operations with low error rates. In order to do this, qubit manipulation must be performed on timescales faster than the quantum state can lose information to the environment- known as decoherence. Maintaining quantum coherence while also allowing for qubit control and readout presents a serious challenge, as qubits must be sufficiently decoupled from environmental noise while also able to interact with one-another and classical control hardware. Quantum error correction schemes have been proposed to tackle this problem, where multiple imperfect physical qubits are encoded in a single logical qubit which is protected against noise. However, even with these schemes, improvements in current qubit lifetimes will be needed, and it is not yet clear which system will provide the most robust semiconductor platform. Towards this end, present efforts underway include spin qubits in GaAs [57, 64, 160], Si [161, 162] and Si/SiGe [163, 164], donor-based qubits in Si [165, 166, 167], as well as topological qubits based on Majorana fermions in proximitised InAs or InSb nanowires [88, 168, 169, 170].

In conjunction with reducing noise and improving qubit operation fidelities, a further hurdle towards quantum computing will be scaling-up the control and readout architecture needed to address more complex quantum systems. This effort is two-pronged: Firstly, scalable qubit-level geometries are required for confinement, coupling and high-fidelity readout in large arrays; secondly, a concerted effort is needed to streamline the hardware and electronics implemented at deep-cryogenic temperatures, which interface between quantum systems and the outside world. To the first point, taking the example of two-dimensional electron gases (2DEGs), the use of sensing channels placed proximal to charge islands has evolved from single up to quadruple quantum dots [14, 171]. These designs however, lack the modularity and extensibility needed to scale to much more than 10 or so dots. Approaches to increase the number of workable qubits much past the current state-of-the-art will soon be hampered by the inflexible gate geometries, as well as the requirement of separate readout sensors. To the second point, present setups for performing fast readout within dilution refrigerators require long chains of active and passive components, as well as high-bandwidth coaxial lines between temperature stages. Simply duplicating these components as the number of qubits is increased will present significant crowding issues. This is true both in the physical domain, as parallel readout chains will require increased density of bulky components and take up a prohibitive amount of space in cryostats, as well as in the frequency domain if unique resonances are required to target each individual qubit [172].

With these issues of scaling in mind, the experiments in this thesis focus on improving readout technologies in order to address the anticipated requirements of future quantum processors. While this work uses quantum dots in GaAs-AlGaAs as a test bed, the methods devised and demonstrated within are broadly translatable to a range of other semiconductor-based qubit systems. In this final Chapter we review these tools and techniques, including quantum Hall and quantum anomalous Hall effect circulators (*Chapters 6 & 7*), dispersive gate sensors (*Chapters 3 & 5)*, and low-loss frequency multiplexed readout chips (*Chapter 4*). In addition, we comment on areas for improvement and future directions. This Chapter is divided into the following sections:

8.1 Quantum Hall plasmonics

Reducing the footprint of components placed close to, or on-chip is a key challenge when scaling-up qubit control and readout systems. The experiments presented in Chapters 6 and 7 of this work focus on the miniaturisation of one such device- the microwave circulator. Circulators are widely used in qubit readout chains to both directionally route high frequency signals, as well as to prevent downstream noise from reaching fragile quantum systems. These components are commonly mounted near qubit platforms at the milli-Kelvin stage of dilution refrigerators, thereby reducing the effects of both thermal noise and amplifier back-action. However, as the physical size of commercial circulators is tied to the signal wavelength, they can take up a significant amount of space, making scaling difficult. This is particularly problematic for the GaAs systems presented in this thesis where the qubit operating band is around 1 GHz, corresponding to a wavelength of almost 30 cm in free space.

Chapter 6 presents results towards a new breed of circulator, fabricated using a high mobility GaAs-AlGaAs heterostructure. In this design, three microwave ports surround a 350 μm wide disc of 2DEG. A magnetic field normal to the plane of electrons breaks time reversal symmetry and leads to the quantisation of the electron motion into orbitals. Applying microwave signals to the ports excites resonant modes which are supported by the one-directional edge channels around the disc. Non-reciprocity of over 25 dB is achieved over a 50 MHz bandwidth, at a centre frequency of $\sim$ 1 GHz corresponding to the quantum Hall (QH) filling factor $\nu = 1$. These results can be understood within an interferometric picture: slow travelling edge magnetoplasmons (EMPs) in one arm interfere with a parallel path given by the parasitic capacitance between ports. This interference occurs at a frequency set by the EMP modes over a length scale that is $1/1000th$ the signal wavelength in free space.

This feature alone presents a significant advantage over commercial, off-the-shelf components. In conventional circulators, a non-reciprocal phase shift is acquired by signals traversing a magnetically-biased ferrite. The key difference between these systems and the circulator devices in Chapters 6 and 7, is that the velocity of the gapless edge excitations in a QH disc is set by the ratio of the electric to the magnetic field at the edge[1]. This gives rise to a slow-light effect where a phase is picked up by the edge mode as it travels between ports in a disc, over a distance of only a few hundred microns. Exploiting the reduced velocity of microwave EMPs thus opens up the prospect of creating a range of compact circuit components including high-impedance transmission and tunable delay lines.

8.1.1 Improving the performance of QH circulators

However, in order for microwave circulator devices based on QH plasmonics to be competitive with other passive approaches, two main aspects need to be addressed. For one, the large magnetic fields required for time-reversal symmetry breaking are a significant barrier to on-chip integration with field-sensitive quantum devices. Secondly, the impedance mismatch between characteristic 50 Ω transmission lines and the QH edge leads to, at present, an unacceptably high insertion loss.

The first issue has, to a large extent, been addressed by the work presented in Chapter 7. In that experiment, microwaves are coupled into an isolated, etched disc of the 3D magnetic topological insulator (TI) $(\mathrm{CrBiSb})_2\mathrm{Te}_3$ on a GaAs substrate. Using a 3-port Carlin configuration, non-reciprocal transmission from two input feeds to a common output is produced at the fundamental EMP mode with frequency $\sim$ 400 MHz. A ‘reverse circulation’ effect is observed at roughly twice this frequency, in line with a Fano-like interference mechanism. Further, after sample magnetisation, non-reciprocity of $>$ 10 dB is maintained at $B = 0$, after ramping down the external magnetic field. In terms of future prospects, while the QAHE in TIs has typically required ultra-low operating temperatures of order tens of mK, new doping methods with vanadium rather than chromium show promise for extending the use of these components up to 100s of mK with a near-ideal Hall angle, and with stability across wider magnetic field ranges [145]. In addition, recent proposals have outlined the possibility of realising the QAHE at much higher temperatures, in different material systems [173, 174, 175].

The second issue regarding impedance mismatch presents a considerable, although not insurmountable, engineering challenge that has inspired recent theoretical work.

---

[1] The minimum energy for velocity v is given by the relation $2\pi\hbar v/L$ for droplet perimeter L [137].

This problem stems from the convention that standard transmission lines are designed to have an impedance of 50 Ω. Ballistic transport, however, in spin-resolved 1D channels is characterised by resistances of ~ 25 kΩ, corresponding to the natural units h/e^2. The resulting impedance mismatch when probing 1D quantum devices at microwave frequencies has been previously addressed in the context of semiconductor quantum dots and QPCs. In these systems, rf reflectometry is performed via LC matching circuits, where a lumped-element inductor is used to cancel the parasitic capacitance and transform a large series resistance towards 50 Ω. While a similar approach can be employed in quantum Hall-based circulators to provide a modest reduction in the insertion loss, the signal loss is still significant. One reason for this is that the effective coupling circuit for the QH circulators described in this work places capacitors at either side of a large series resistance. Relaxing the operational frequency constraints, one option for improved impedance matching in QH circulator devices might be to operate at higher frequencies (a few GHz, say). The benefit of this approach is that the complex impedance due to the capacitive coupling is reduced as $Z_C = 1/j\omega C$. In addition, for the case of GaAs-AlGaAs materials, operating at higher frequencies for the same sized discs enables measurements to be performed at lower magnetic fields. In this regime, more Landau levels are able to contribute to conduction, leading to a reduction in R_{xy}.

A complementary approach to overcome this challenge, as proposed in Ref [139], involves re-engineering a 3-port Carlin circulator geometry into a two-port gyrator device. In this proposal the third electrode is connected as a common ground between the two operational ports. The ratio of coupling capacitances between the ports and the ground to the conductive Hall disk, can then, in principle, be configured for a given impedance mismatch to achieve perfect gyration. This effect stems from the fact that gyrators have the ability to convert a load capacitance into an inductance, thereby acting to 'self-match' at certain frequencies. Near the Hall angle of $\pi/2$, the coupling of the ports to the mesa might also be modelled as a stub network, where varying the length of the stubs (corresponding to the arcs surrounding the disc) can tune the load matching in a similar way [176].

Fig. 8.1 **(b)** shows a design for such a gyrator based on the devices outlined in Chapters 6 and 7 and the considerations listed above. In this geometry, two ports (1

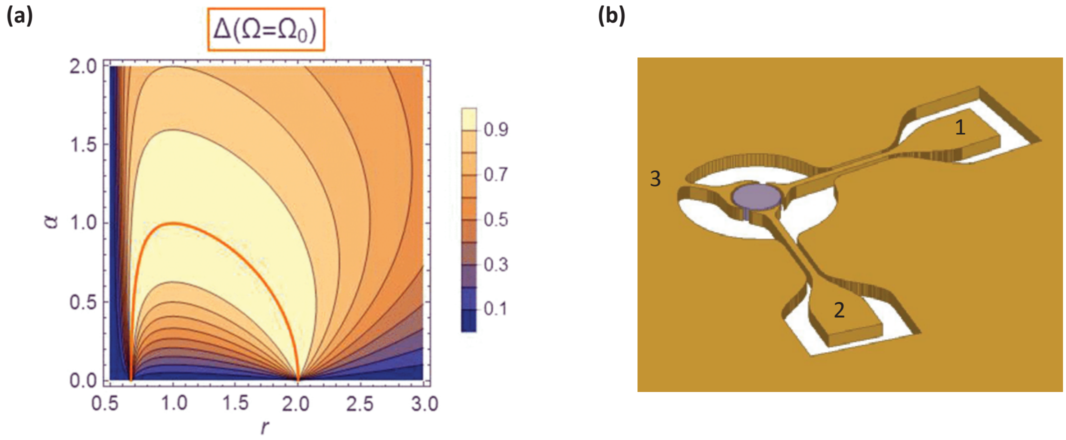

Figure 8.1: The self-impedance matched gyrator. **a** Theoretical calculation of gyration for a two-port device with a common capacitive ground, characterised by Δ, at the fundamental frequency $\Omega = \Omega_0$. The impedance mismatch parameter, α, and the ratio of coupling capacitances, r, are varied. Perfect gyration of $\Delta = 1$ is found to occur along the orange line when $r = 2$, see Ref. [139]. This figure is reprinted with permission, from Ref. S. Bosco, F. Haupt, and D.P. DiVincenzo, Phys. Rev. Applied **7**, 024030, Copyright 2017 by the American Physical Society. **b** Design of a 2-port quantum Hall gyrator with the third port configured as a common ground. The ratio of the capacitances from each of the ports to the Hall droplet, and from the droplet to ground, is set in the ratio of 1:2.

and 2) are configured as 50 Ω coplanar transmission lines, while a third port (3) is grounded. The combined arc lengths of the ports (L_1, L_2, L_3) surround $> 90\%$ of the disc perimeter, such that the EMP mode velocity can be considered uniformly. The length of each of the two signal port arcs is equal to half that of the ground, giving

$$\frac{c_3 L_3}{c_1 L_1} = \frac{c_3 L_3}{c_2 L_2} = 2 \tag{8.1}$$

where c_i denotes the capacitance per unit length of each of the i ports. This fulfils the conditions outlined in Ref. [139] for good gyration (characterised by the term Δ) at the fundamental frequency Ω_0.

8.1.2 QH coupling schemes for quantum dots

Apart from non-reciprocal electronics, the prospect of transporting information using QH edge states opens up a host of other practical applications, including coupling spatially separated quantum systems. As mentioned previously, reliably coupling and performing entangling gate operations between qubits are core requirements of any quantum computing architecture. In the context of spin or charge qubits, long-range coupling approaches involving floating metallic gates [177, 178], microwave cavity resonators [73, 179, 180, 181], ferromagnets [182], and indirect exchange through many-electron quantum dots [183] have all been investigated.

Using QH edge states to mediate the interactions between quantum dot systems presents two key benefits. Firstly, QH edge states can be formed in the same materials as the confined dots and defined via standard chemical etching or gating techniques. Secondly, chiral edge states are robust against disorder due to their topologically-protected character. In the proposal in Ref. [184], the long-range magnetic RKKY[1] interaction in a QH edge facilitates coupling between individual electron spins. A second approach, outlined in Ref. [185], suggests an electrostatic coupling mechanism between singlet-triplet (ST) qubits with distinct charge states, and EMP modes. In that case, an oscillating frequency can be used to drive the state-dependent qubit dipole which, in turn, modulates the confining potential at the EMP.

The extent to which varying a local electric field can affect the frequency of EMP modes is explored in Chapter 6 of this work. In that geometry, RF port electrodes are positioned to overlap the mesa edge by 10 μm, while static dc voltages apply a negative bias relative to an annealed, Au/Ge grounded contact. After an initial renormalisation of the EMP frequency with gate voltage, tunability across many linewidths is observed with a modest change in V_G (with a maximum slope of 5 MHz/mV). This degree of sensitivity gives cause for optimism for the coupling approach described in Ref. [185], although physically implementing such a setup on-chip is not without its challenges.

8.1.3 Quasiparticle detection

As a final remark on QH plasmonics, we note that extensions of the devices in Chapters 6 and 7 of this thesis may find use in quasiparticle-detection schemes based on the fractional quantum Hall effect (FQHE). Excitations in the FQHE are proposed to arise from fractionally-charged quasiparticles, and are expected to obey unusual statistics

---

[1] Ruderman-Kittel-Kasuya-Yosidathe

upon the exchange of particles (braiding). Harnessing these exotic properties to create 1D helical channels, or to host Majorana modes, would have profound implications for topological quantum computing. However, measuring quasiparticle excitations is difficult in dc transport experiments, where QH edges equilibrate at the current and voltage leads. In Ref. [137], Cano *et al* suggest employing microwaves as noninvasive, spectroscopic probes of QH liquids. By coupling a transmission line to a 2DEG droplet, signatures of individual edge states are predicted to manifest as peaks in the absorption spectrum. Further, by forming a beamsplitter with a QPC, modulations of the peak amplitudes can be mapped to quasiparticle tunnelling events. In this way spectroscopic measurements can shine a light on fractional excitations without perturbing the QH edge modes.

A first iteration of such a setup is realised in Chapter 6 of this work, wherein a disc of QH fluid is embedded between the signal and ground plane of a coplanar waveguide. An overall frequency dispersion curve is observed and attributed to the EMP fundamental mode, while peaks in the spectrum are found to align with integer filling factors in dc transport. At present however, the small relative absorption ($\sim$ 0.2 dB) limits the degree to which more exotic phenomena can be resolved in this setup. In future experiments, improvements in the dynamic range of the signal could be attained by increasing the capacitive coupling of the edge to the transmission line, similar to the curved-port QH circulator designs in Chapters 6 and 7. In addition, reducing the electron temperature should enable fractional states to be accessed- a crucial first step for realising the approach in Ref. [137]. One such techniques to achieve this is using fence gates to isolate ohmic contacts. This would create a tunable channel for electrons in the otherwise isolated 2DEG to be brought into thermal equilibrium with the lattice.

8.2 High-bandwidth qubit readout

Turning again to the challenges of scaling, a key consideration for building up quantum technologies is how to interface engineered quantum systems with the outside world. Working within extreme environmental conditions, this effort requires at once maximising the number of physical qubits, while minimising the footprint and power consumption of control and readout hardware. This is a particularly demanding task in the case of readout where fragile quantum information must be translated into measurable outputs via chains of classical electronics.

Since the mid-2000s, high-frequency reflectometry has represented the state-of-the-art for readout of semiconductor qubits. These setups have typically comprised proximal sensors in the form of single-electron transistors [86, 186], auxillary quantum dots [187] or separate quasi-1D channels of 2DEG [27, 63]. By measuring changes in the amplitude of the reflected carrier wave, the state of a multi-dot configuration can be rapidly measured at higher frequencies which are less affected by $1/f$ noise. However, while these schemes have allowed measurements to be performed with integration times as low as a few hundred nanoseconds, they have also necessitated the introduction of numerous bulky components within the experimental setup. This includes high-bandwidth coaxial lines, directional couplers, wideband circulators, and low-noise amplifiers to boost signals. Duplicating these components, along with on-chip sensors and contacts, is not a feasible approach moving forward. As future experiments mature from a handful of quantum dots to larger arrays, it is likely that the tools and techniques outlined in Part II of this work will become increasingly commonplace. With regards to Chapters 3, 4, and 5, the approach towards improving current readout techniques is twofold: firstly, reducing the number of on-chip structures needed for sensing, and secondly, integrating multiple high-bandwidth channels into a common readout chain.

8.2.1 Dispersive gate sensing

The experiment in Chapter 3 involves probing the fast tunnelling dynamics of single and double quantum dots formed in GaAs-AlGaAs 2DEGs. Fast charge readout is performed by embedding an existing dot-defining gate electrode within a chip-level resonant circuit. A crucial advantage of this dispersive gate sensing (DGS) technique is that no additional structures are required on-chip for readout. Unlike an rf-QPC where variations in the conductance of a channel within the 2DEG are mapped to changes in the reflected signal, DGS makes use of the capacitance between a metallic gate and its environment, C_g, to sense charge oscillations. Near the intra-dot charge transition point, these oscillations give rise to a quantum capacitance $C_Q = (e^2/2t)(C_g/C_\Sigma)^2$ where t denotes the tunnelling energy and C_Σ parametrises the total double dot capacitance. Changes in C_Q then adjust the admittance of the resonator, leading to shifts in the frequency f_0 by an amount $\delta f = C_Q f_0/2C$ where C is the geometric capacitance. Importantly the setup filters out low frequency noise as the resonator response is only sensitive to tunnelling events occurring on timescales faster than or comparable to f_0. More subtly, an additional advantage of DGS is that a qubit can be directly probed and measured at well-defined frequencies without out-of-band noise perturbing the system. This is contrasted with traditional QPC reflectometry, where broadband shot noise from tunnel junctions can lead to qubit decoherence. Looking forward, the demonstrated ability of dispersive sensing to distinguish the symmetric and anti-symmetric basis states of double quantum dots [78, 188], makes it a promising technique for performing readout of semiconductor-based two-level systems with differing energy band curvatures. For example, the joint parity ground state of Majorana zero modes formed at the ends of hybrid quantum dots in 1D nanowires [170].

Dispersive gate sensing is extended in Chapter 5 as a tool to probe the local electrostatic environment of a QPC. When these channels are electrostatically constricted, the depopulation of each sequential 1D mode leads to a change in the compressibility, κ, and reduction in the channel's ability to screen the electric field from its confining gates. These variations in κ are related to the quantum capacitance, $C_Q \propto e^2\kappa$. By connecting one gate of a QPC to an LC circuit, changes in the demodulated resonator response can be used to map out the 1D electron subband structure. In addition, Chapter 5 presents somewhat unexpected features observed in the dispersive response of an asymmetric QPC below the last conductance plateau. These features are affected by laterally shifting the QPC, and are attributed to the presence of local pockets of trapped charge.

Beyond this body of work, the next steps will involve improving the sensitivity of DGS in order to demonstrate single-shot readout of a singlet-triplet qubit. In the experiment in Chapter 3, a sensitivity of $\sim 6.3 \times 10^{-3}\ e/\sqrt{Hz}$ is extracted over a bandwidth of 10 MHz corresponding to an integration time of 39 μs. This is currently trailing behind the standard for an rf-QPC (arguably the next most scalable method) where sensitivities of $\sim 10^{-6}\ (e^2/h)/\sqrt{Hz}$ [27] have been extracted, and singlet-shot readout with 98% fidelity in $\sim 1\ \mu$s [64] has been performed. At the level of the device,

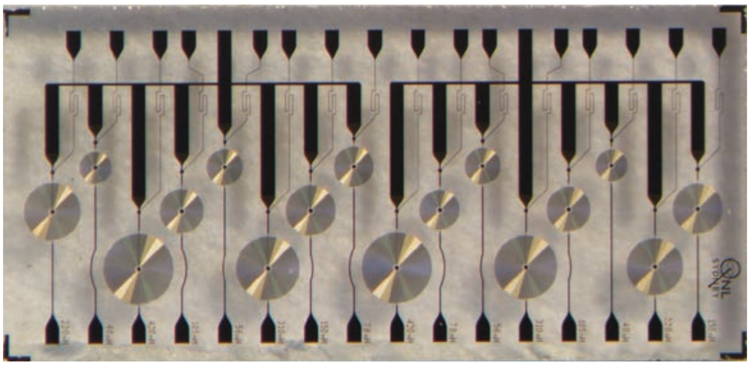

Figure 8.2: New generation of QNL multiplexing chips. 16:1 frequency multiplexing chip fabricated and designed by J. M. Hornibrook. Features are defined using NbTi on a polished saphire substrate. This chip is 5.2 mm x 2.46 mm, and has 16 matching inductors in the range 40 nH - 420 nH. *RC* bias tees are implemented with parallel plate capacitors using NbTi and a SiO2 insulating layer, and an AuPd layer to form resistors.

this effort will require redesigning gate geometries for increased C_Q. Further up the readout chain, improved signal-to-noise ratio (SNR) could be achieved by replacing traditional cryogenic HEMT[1] amplifiers with quantum limited versions that have been invaluable within the superconducting community. For example, the implementation of Josephson parametric amplifiers (JPAs) [189, 190, 191] combined with fast readout of quantum dots, as demonstrated in [192].

8.2.2 Frequency multiplexed readout

Coupling dispersive gate sensing (DGS) with frequency-multiplexing schemes further streamlines the circuitry required for rf readout. Chapter 4 details the design and implementation of a 3-channel matching network fed from a single rf input. The device is fabricated with superconducting Nb film on a low-loss sapphire substrate. Each channel is equipped with an *LC* bias tee comprising a spiral inductor and interdigitated capacitor, to allow for the dual application of static offset voltages and oscillating electric fields. In addition, discrete 'matching' inductors are added to each parallel line and wire-bonded to ohmic contacts or metallic gates on the device. The resonant circuit formed with this inductance and parasitic capacitance on the device can be identified and addressed via the common feedline. Crucially, by integrating these circuit elements on

---

[1] High-electron-mobility transistor

a single multiplexing chip, the size of the setup is made less than the signal wavelength and thereby eliminates unwanted impedance-mismatch effects that can arise from stub resonances.

In the experiment in Chapter 4, this frequency-multiplexed readout technique is demonstrated for the case of two rf-QPCs and a DGS in the few-electron regime of a double quantum dot. In addition, a proof-of-concept solution for 10-channel readout is presented using HEMT switches. In terms of scaling-up these chips it is not difficult to imagine that by introducing state-of-the-art fabrication techniques, the amount of LC resonators could be increased by at least a factor of ten. For instance, by incorporating multi-layer processes and electron-beam lithography. The bias tee inductors could also be replaced by patterned resistors for a further reduction in footprint (as well as bypassing size limitations related to the reduced self resonance frequency). A current version multiplexed chip designed in the QNL in Sydney is shown in Fig. 8.2, incorporating 16 channels over a 5.2 mm $\times$ 2.46 mm chip with inductors in the range from 40 - 420 nH, designed for the operating band of spin qubits.

8.2.3 Final remarks

Employing both DGS and multiplexed readout could feasibly allow tens or possibly even a hundred qubits to be probed with a single high-bandwidth addressing chain. By lifting the spatial requirement and associated electronics of distinct sensing channels, more complex confinement arrays can be explored without the overhead of auxiliary SETs or QPCs. This would be particularly useful in long arrays of quantum dots where it is not physically practical to use electrometers. Moreover, these techniques not only increase the amount of quantum dots that can be probed, but also the number of sensors available per dot without having to scale any of the on-chip structures. For example, multiplexed tank circuits could be bonded both to wall gates and ohmics to sense different charge transitions, making use of the capacitive contributions of a quantum dot to its environment. In this way, fluctuations in the local charge density under a gate, or preferential tunnelling to a lead, could be combined to build up a more complete description of the potential landscape. Finally, the addition of chip-level circulators, once optimised for low insertion loss, would also alleviate the burden of adding bulky,

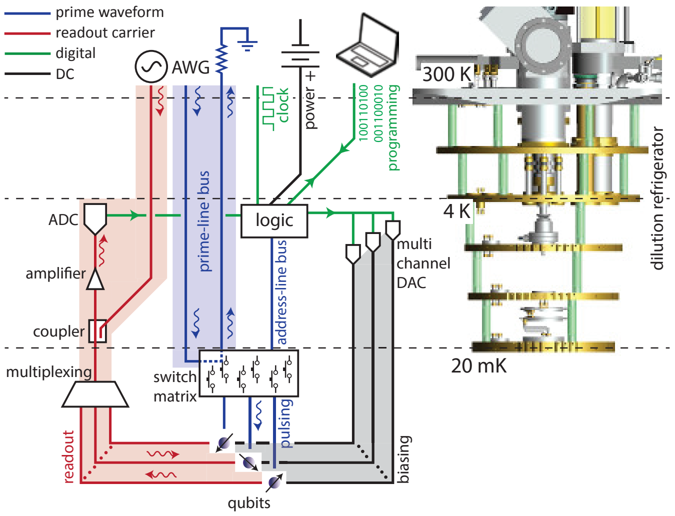

Figure 8.3: Qubit control microarchitecutre in a dilution fridge. Schematic illustration of a qubit control architecture within a dilution fridge comprising a chip-level semiconductor switching matrix for rf signal routing, cryogenic logic platform using a commercial field programmable gate array (FPGA) at the 4 K stage, and cold digital-to-analog (DAC) converters. This figure is reprinted with permission, from Ref. J. M. Hornibrook et al, Phys. Rev. Applied **3**, 024010, Copyright 2015 by the American Physical Society, DOI: 10.1103/PhysRevApplied.3.024010.

non-reciprocal components to the rf output line when performing operations on multi-qubit arrays.

Beyond this target, a new wave of challenges will be faced when scaling beyond ∼100 readout lines or so. Here, approaches to increase the number of channels will likely be hindered by the limited bandwidth and noise added by commercial amplifiers operating at 4 K, and the mounting room-temperature resources required. As flagged in Chapter 4, at this juncture more creative approaches will be necessary to increase the amount of qubits that can be addressed. For example, interleaving rf frequencies in the time-domain, exploring multi-layer fabrication at the qubit level, and making use of cryogenic switching technologies [193] (see Fig. 8.3). Looking towards qubit numbers in the hundreds, there are growing motivations for transplanting much of the suite of room-temperature control electronics down to deep cryogenic temperatures, close to the device [172, 193, 194]. These reasons include the latency associated with implementing feedback, the sheer number of lines in a cryostat and their associated size and thermal gradient, and the infeasibility of cloning existing room temperature setups. The implementation of such architectures, while also managing qubit coherence times and large-scale coupling, will crucially require a multi-disciplinary effort between fundamental physics and cutting-edge engineering, in order to realise future quantum machines.

Appendix

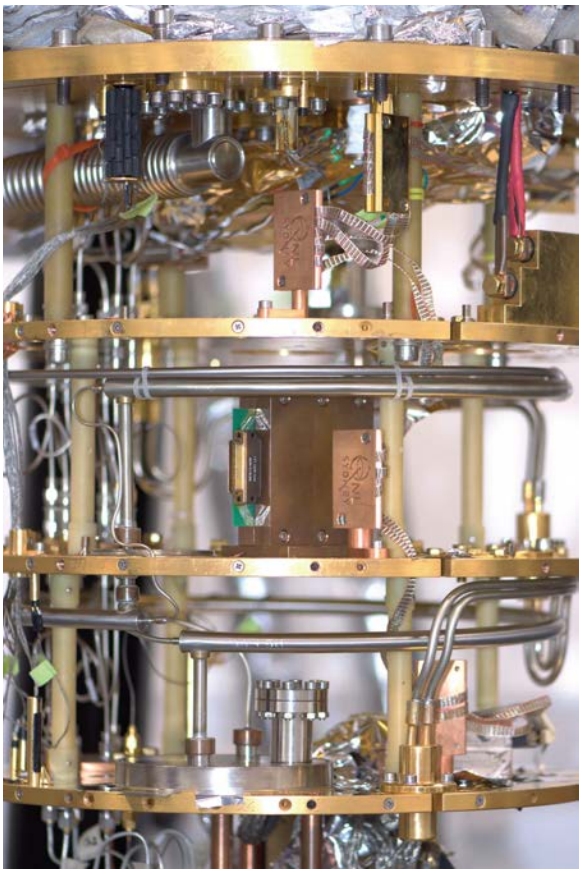

A

Additional materials for Chapter 5: "Dispersive gate sensing the local electrostatic environment of a quantum point contact"

This section provides additional figures for the experiment presented in Chapter 5. In particular, the effects of increased cryostat base temperature and in-plane magnetic field are presented. A second asymmetric-potential QPC is also shown, and the dc and DGS responses are compared.

A.1 Effect of in-plane magnetic field and increased temperature on DGS response

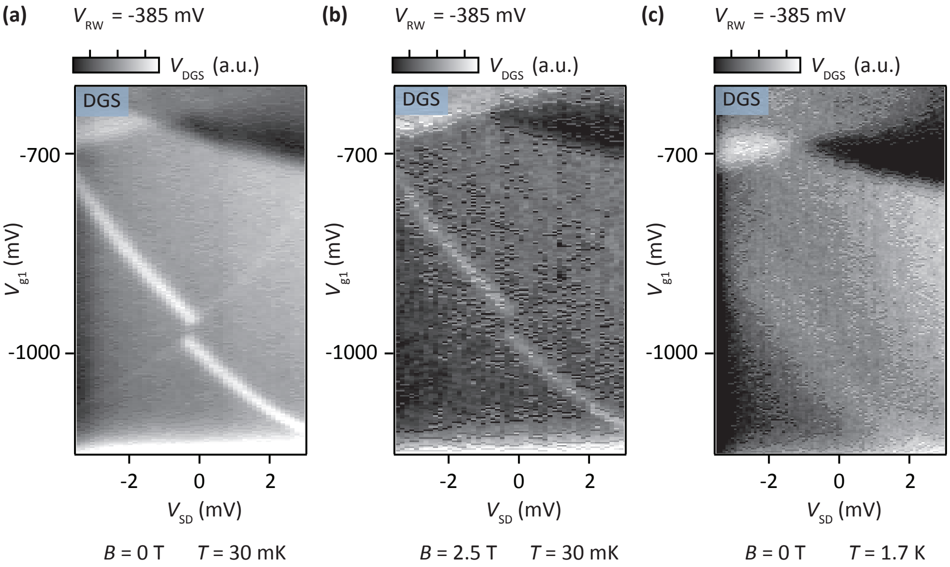

Figure A.1: Increasing in-plane magnetic field and temperature. Asymmetric QPC potential formed with V_{RW} = -385 mV and sweeping V_{g1} and V_{SD}. DGS measurements performed at $f = 554$ MHz. **(a)** V_{DGS} response with zero applied magnetic field and dilution fridge base temperature of T = 30 mK. **(b)** Shows the same region in gate space as (a), with an in-plane field of B = 2.5 T. In **(c)**, B = 0 mT and the mixing chamber temperature is increased to T = 1.7 mK. The bright features are found to persist in both of these regimes, in the same region in gate space. Signal degradation across the whole spectrum in (b) is attributed to reduced performance of the Nb matching inductor setup. Thermal broadening of the signal is observed in (c).

A.2 Response of second asymmetric QPC

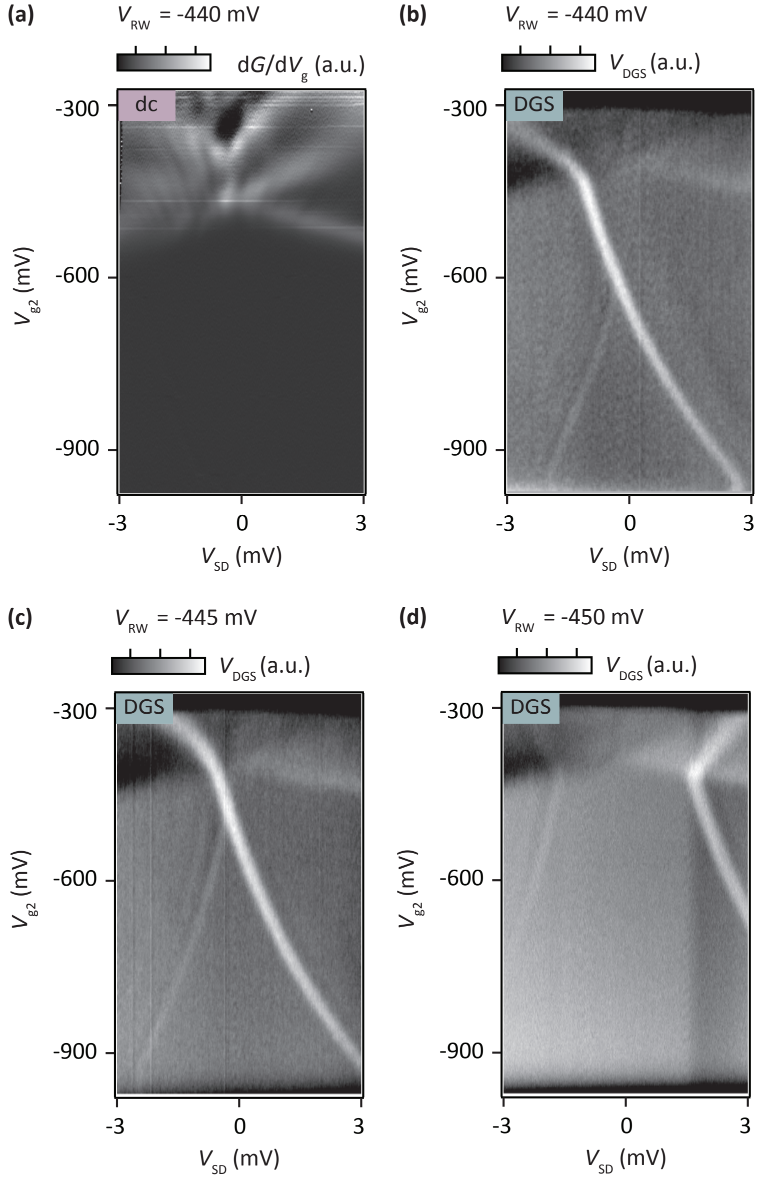

Figure A.2: dc and DGS measurements of second QPC. Non-linear differential conductance, G and DGS measurements, V_{DGS}, with source drain bias, V_{SD} and V_{g2} (see labels on electron micrograph, Fig. 5.3(a)). **(a)** Shows the derivative dG/dV_g through an asymmetric QPC potential created by keeping V_{RW} at a constant voltage of -440 mV and making V_{g2} increasingly negative. **(b)** presents the dispersive response measured at a frequency of 554 MHz, while V_{g2} is rastered about -600 mV. Bright lines are observed in the gate space region past pinch-off. V_{RW} is varied in **(c)** and **(d)** to probe the effect of laterally shifting the channel.

A. ADDITIONAL MATERIALS FOR CHAPTER 5: "DISPERSIVE GATE SENSING THE LOCAL ELECTROSTATIC ENVIRONMENT OF A QUANTUM POINT CONTACT"

B

Additional materials for Chapter 6: "On-Chip Microwave Quantum Hall Circulator"

This section provides additional information for the results outlined in Chapter 6. This includes descriptions of the devices and experimental setup, time-domain investigations of edge magnetoplasmons, a discussion of insertion loss, and details of the model.

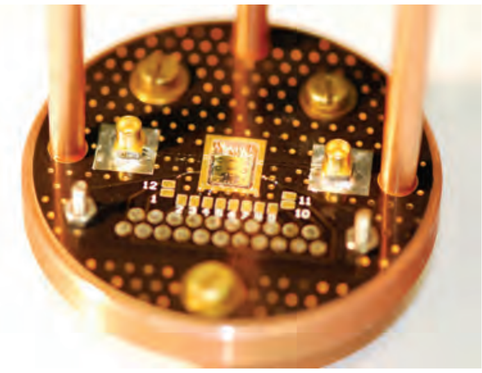

Figure B.1: Sample setup. Photograph of a 2-port transmission line device, wire-bonded to a PCB. The PCB is in thermal contact with a copper stage that is mounted to the mixing chamber of a dilution refrigerator.

B.1 Devices and circuit details

All devices are fabricated on GaAs-AlGaAs heterostructure with a 2-dimensional electron gas (2DEG) located 270 nm below the surface. From dc Hall transport measurements on the chip shown in 6.1, an electron density of $n_s = 1.1 \times 10^{11}$ cm^{-2} is extracted, along with carrier mobility of $\mu = 5.2 \times 10^6$ cm^2/Vs. Small variation in these values are observed for the different devices measured, likely due to density variations across the wafer and effects of chemical processing. Circular mesa disks are etched using a $H_2O/H_2O_2/H_2SO_4$ solution to a depth of $\sim$ 320 nm.

Metallic Ti/Au is evaporated on top of the devices to form the waveguide and circulator port structures. For the transmission-line device shown in Fig. 6.1, a coplanar transmission line geometry is employed using a 50 μm wide signal track with ground planes on either side. The distance to these ground planes measures 30 μm, ensuring a coupling impedance of $\sim$ 50 Ω within the frequency range of operation. The 350 μm diameter disc is situated equidistant between the signal line and ground plane, with a gap of 20 μm at either side. The data in Fig. 6.1 (c) is taken on a device with an additional 100 μm diameter ohmic contact placed in the centre of the mesa to assist in thermalization of the isolated disk of electron gas. This contact does not intersect the edge and as such we find that the overall dispersion spectrum (Fig. 6.1 (c)) is qualitatively the same for devices without a centre ohmic contact.

For the three-port device introduced in Fig. 6.2, a 330 μm diameter disk is placed at the centre of the structure, with metallic ports separated by 20 μm from the mesa. The edges of the ports form 250 μm long curved arcs, and a surrounding ground plane is separated back from the disc by 385 μm. The device in Fig. 6.6 comprises a 400 μm diameter mesa, along with three Ti/Au ports with 250 μm long curved arcs that overlap the disc by 10 μm. An Au/Ge contact with 100 μm diameter is annealed in the centre of the mesa. As the droplet is otherwise floating, we are unable to measure the resistance to the 2DEG. The contact is bonded to the ground plane of the PCB.

Chip-inductors (47 nH copper wire-wound, Coilcraft 0805HT series) are bonded to each of the three ports of the circulator to form an impedance matching network. The inductors are found to resonate with the stray parasitic capacitance in the setup C_{stray}, at a frequency of $\sim$ 1 GHz in the absence of a magnetic field. All measurements are performed at the base temperature $T \sim 20$ mK of a cryo-free dilution refrigerator (Leiden Cryogenics CF500).

Devices are connected to two layer copper printed circuit boards (PCBs) constructed from Rogers 6006 high frequency laminate. These are mounted flat on a copper stage, which is thermally anchored to the mixing chamber plate of the dilution refrigerator (Fig. B.1). A cut-out in the PCBs enables devices to be silver pasted directly onto the copper beneath, ensuring good thermal contact. The ground planes of the devices are electrically connected to the ground of the PCB using numerous aluminum bondwires.

B.2 Extracting the dielectric permittivity:

The overall dispersion curve of the fundamental edge magnetoplasmon (EMP) mode is extracted from the position of the features in the 2D data, as shown in the inset of Fig. 6.1 (c). Black markers plot the center frequency for which the features occur, measured at magnetic field values corresponding to integer filling factors ν, down to $\nu = 2$, (errors are within the square marker bounds). The black solid line shows a fit to the resulting 1D data using the nonlinear dispersion relation for the fundamental mode:

$$\omega = \frac{\sigma_{\text{edge}} q}{2\pi\varepsilon^* \varepsilon_0} \left[\ln \frac{2}{ql} + c \right] \tag{B.1}$$

Here $\omega = 2\pi f$, σ_{edge} is the transverse conductivity of the edge, ε^* and ε_0 are the dielectric constant and permittivity of free space respectively, $c = 1$ for a sharp (etched) edge, and $q = 2\pi/p$, where p is the sample perimeter (see Ref [49] for details of this expression, and also Refs. [52, 129, 130, 131, 132, 133, 134, 135, 136, 138]). The parameter l gives the physical extent of the EMP away from the etched edge of the mesa and is approximated by:

$$l = \frac{n_s m^*}{2\varepsilon^* \varepsilon_0 B^2} \tag{B.2}$$

where $n_s = 1.1 \times 10^{11}$ cm^{-2} is the carrier density, and m^* is the effective electron mass in GaAs of 0.067 m_e. We extract the free parameter $\varepsilon^* \approx 8.7$ from the fit, consistent with Ref. [138]. This value of ε^* corresponds to an average of the dielectric constant of GaAs and the vacuum, since the capacitive response of the system includes the edge-state, etched trench, and metallic structure that defines the microwave port.

B.3 Further experimental details

For the circulator shown in Fig. 6.2, the return line $2'$ is amplified at the 4 K stage of the fridge with a low-noise, resistive-feedback, cryogenic amplifier (CITLF1, Weinreb group, Caltech) with a noise temperature of $\sim$ 5 K and Gain of 40 dB. The return signals are further amplified at room temperature. The applied microwave power at the device is in the range -90 dBm to -60 dBm. Features appear sharper at lower microwave power, but with a decrease in signal to noise. S-parameter measurements are taken with a Keysight N5245A PNA-X network analyzer.

In Fig. 6.6 and Fig. B.5. of the supplementary material, each of the three circulator arms are connected to bias tees, while directional couplers are used on the rf sides of ports 1 and 2 to allow for amplification of the return signal at 4 K. This enables us to compare the signal outputs from a common input port. As in Fig. 6.3, the isolation plot in Fig. B.5 is normalized relative to the transmission background at $B = 0$, and in the absence of dc gate biasing. Striations in the data are attributed to standing waves arising from an impedance mismatch between the device, cryo-amp, and passive components in the rf setup.

B.4 Time domain measurements

Time domain measurements are performed on the circulator in Fig. 6.2 as a function of magnetic field. An AWG 5014C arbitrary waveform generator is used to generate a voltage step, which is directed to lines 1 and 3 of the device. The rising edge of the signal acts as an 'injector', generating a charge density oscillation that propagates around the edge of the mesa. The output signal from Port 2 is amplified before being measured with a digital sampling oscilloscope. As the signal travels close to the speed of light through the coax lines (which are nominally identical inside the fridge for lines 1 and 3), delays between $S2'1$ and $S2'3$ are attributed to the difference in path lengths around the disc. Within the GaAs droplet, the pulse is significantly slowed down by the low frequency EMP modes. In Fig. B.2 (a) at a fixed magnetic field of 3.75 T, periodic decay oscillations are visible in both $S2'1$ and $S2'3$ at $\sim$ 525 MHz. This corresponds to the frequency measured for the $\nu = 1$ filling factor on the fundamental EMP mode. Setting $t = 0$ to be where the signal is first observed, $S2'1$ is found to arrive before $S2'3$ by approximately a quarter of a wavelength, in line with the expected expected $2\pi/3$ path length distance between the ports.

Fig. B.2 (b) depicts transmission $S2'3$ as a function of magnetic field for the same measured time interval as B.2 (a). The zero B field response is subtracted from the 2D data and the red (blue) stripes correspond to minima (maxima) in the received signal. At $t = 0$ a signal is measured for all values of magnetic field, indicating transmission of the voltage pulse. This wave is quickly damped however, for all but two regions of magnetic field corresponding to the first and second integer filling factors. We extract the frequency of the two extended oscillations at $B = 1.9$ T and $B = 3.8$ T ($\sim$ 960 MHz and 525 MHz respectively) and find them to be in good agreement with the frequency dispersion of the fundamental mode. No higher frequency components associated with coupling to the first harmonic mode is visible in the time of flight data.

In a separate experimental cool-down, we demonstrate reconfigurable routing of a 1 GHz wavepacket by changing the value (but not the polarity) of the external magnetic field (Fig. B.3). An E8267D vector signal generator is used to output a 1 GHz continuous wave which is then modulated with a Gaussian envelope via an AWG before being directed to port-1 of the device. In this particular setup, a mechanical switch (Radiall DPDT series) is installed and mounted on the mixing chamber stage of the fridge, enabling the output lines 2 and 3 to be selectively directed through a common return line. The response is then amplified by a cryogenic amplifier. We measure the resultant signal with an oscilloscope, and a fast Fourier transform (FFT) is performed in post-processing.

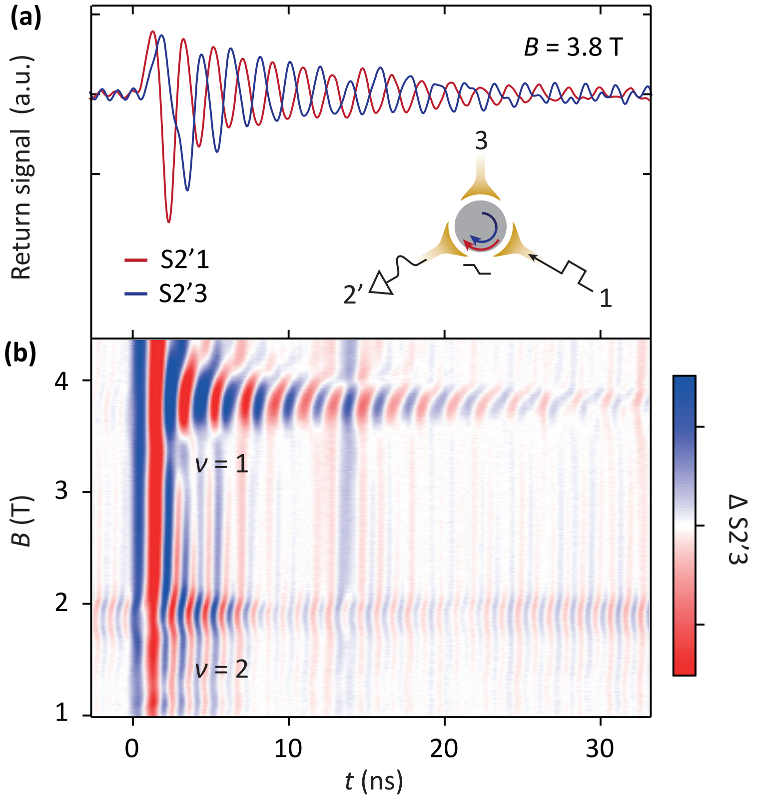

Figure B.2: Time domain measurement with magnetic field. **(a)** Amplified transmission signals S2′1 (red) and S2′3 (green) as a function of time at $B = 3.8$ T. Fits to the data yield oscillations of 525 MHz, corresponding to the frequency-domain measurements at filling factor $\nu = 1$. **(b)** 2D time of flight measurements as a function of magnetic field. Oscillations are visible at two distinct B fields, which we attribute to $\nu = 1$ and $\nu = 2$.

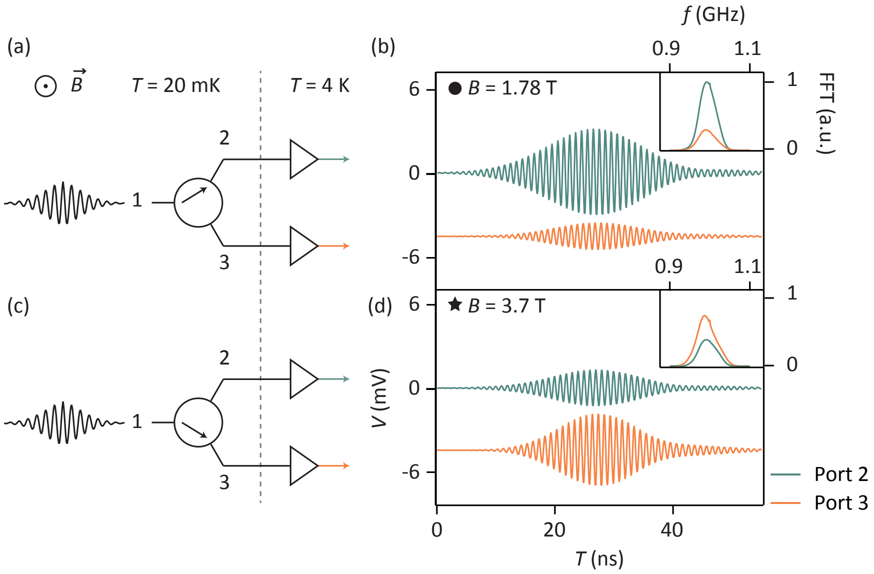

Figure B.3: Re-configurable microwave routing. **(a)** and **(c)** Schematic showing the experimental configuration for on-chip routing of microwave signals with varying magnetic field. A wavepacket is directed to port 1 of the circulator, and the resultant signals are measured after amplification at ports 2 and 3. **(b)** and **(d)** Output signal, as configured by adjusting the amplitude of the magnetic field to direct wave packets to the required port. Insets show normalised fast Fourier transform (FFT) amplitudes.

B.5 Lowering the insertion loss

In the current configuration of our circulator, while the edge-states are essentially dissipationless, the device presents an insertion loss due to the impedance mismatch between the Hall edge and the conventional 50 Ω impedance electrical circuit. This is in no way an intrinsic limitation. For the demonstration reported in the paper, we show the full response of the circulator with B-field, measuring across several GHz. With the general response of the circulator characterized, it is then possible to make use of standard microwave engineering approaches to impedance match the circulator to the arbitrary impedance of a transmission line over a narrow band. This is commonly done with devices such as the rf-SET or rf-QPC (see Refs. [27, 63, 90]) where an “L-match” is used to transform the $\sim$ 100 kΩ device impedance towards the 50 Ω impedance of a transmission line over 10 MHz.

Given that the circulator impedance acts like a load of order 25 kΩ (for $\nu = 1$) in series with the port capacitance, additional approaches to engineer a better match include:

1. Decreasing the size of the Hall droplet, thereby increasing the frequency of the resonant EMP modes and lowering the complex impedance from the ports to the edge.
2. Operating at a higher (quantum Hall) filling factors and lower magnetic fields where the impedance of the edge is closer to $Z_0 = 50$ Ω, see Ref. [140].
3. Altering the characteristic impedance of on-chip transmission lines, alleviating the constraint of working with $Z_0 = 50$ Ω.

Working with layered 3D semiconductor stacks may also produce a similar reduction in the impedance [34]. We emphasise that the insertion loss of our device stems from the choice of coupling to cables with a characteristic impedance of 50 Ω, leading to a reflection of power rather than dissipation. In addition, a recent theoretical proposal by Bosco, Haupt and DiVincenzo [139] suggests a new configuration whereby a self-matched three-terminal gyrator can be achieved by grounding one of the port electrodes. Once incorporated into an interferometric setup, this design should also facilitate operation as a circulator [139].

B.6 Description of model

We begin with the admittance matrix Y_{edge} for a three-port quantum Hall circulator using a Carlin type device, exactly as described in Ref. [123]:

$$Y_{\mathrm{edge}}(\omega) = \begin{pmatrix} ia & b & -b^* \\ -b^* & ia & b \\ b & -b^* & ia \end{pmatrix}$$

Where, as in Ref. [123],

$$a = \frac{2\sigma_{\mathrm{edge}} \sin \frac{\omega C_{\mathrm{edge}}}{\sigma_{\mathrm{edge}}}}{1 + 2\cos \frac{\omega C_{\mathrm{edge}}}{\sigma_{\mathrm{edge}}}}$$

$$b = \sigma_{\mathrm{edge}} \frac{-1 + e^{\frac{-i\omega C_{\mathrm{edge}}}{\sigma_{\mathrm{edge}}}}}{1 + 2\cos \frac{\omega C_{\mathrm{edge}}}{\sigma_{\mathrm{edge}}}}$$

with ω the angular frequency, σ_{edge} is the conductance of the edge ($1/\sigma_{\mathrm{edge}} = R_{xy}$) and C_{edge} the contact capacitance between each of the port terminals and the edge. Note this 3 x 3 matrix is not symmetric and so captures the non-reciprocal response of the chiral edge magnetoplasmons.

We now modify the circuit with respect to Ref. [123], by adding terms to account for dissipation R, either along the quantum Hall edge or elsewhere in the circuit, as well as a direct parasitic capacitive path C_{p}, between port terminals. We derive an admittance matrix Y_{total} which captures these additional terms as a function of Y_{edge}, R, and C_{p}.

Referring to the circuit diagram shown in supplementary Fig. B.4, and given Ohm's

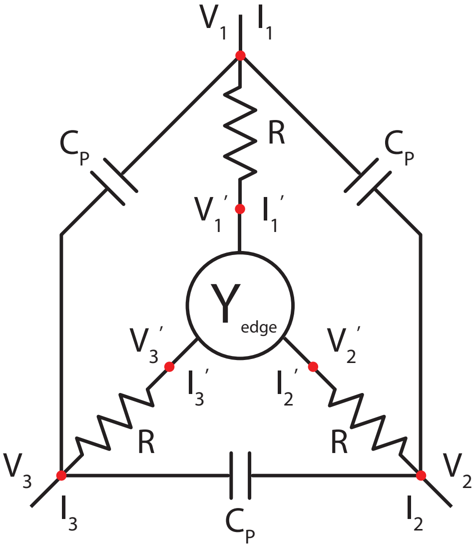

Figure B.4: Theoretical circuit model. Circuit diagram of a three port circulator including dissipation R and direct parasitic capacitive coupling C_p between port terminals. Nodes where I/I′ and V/V′ are calculated are shown in red.

law we write:

$$\vec{I'} = Y_\mathrm{edge}\vec{V}' \text{ and } \vec{V} = \vec{V}' + R\vec{I'},$$

where $\vec{I'}$ ($\vec{V}'$) are the vectors of currents (voltages) of Y_edge and $\vec{I}$ ($\vec{V}$) are the vectors of currents (voltages) of Y_total. Rearranging and substituting we find,

$$\vec{I'} = Y_\mathrm{res}\vec{V}$$

where

$$Y_\mathrm{res} = (\mathrm{I} + RY_\mathrm{edge})^{-1}Y_\mathrm{edge}\vec{V}$$

and I is the identity matrix.

We can then write out the individual components of $\vec{I}$ by summing the net flows in and out of each port of the circulator:

$$\begin{array}{l} I_1 = I'_1 + (I_{12} - I_{31}) = (Y^{11}_{\text{res}} V_1 + Y^{12}_{\text{res}} V_2 + Y^{13}_{\text{res}} V_3) + i\omega C_{\text{p}} (2V_1 - V_2 - V_3) \\ I_2 = I'_2 + (I_{23} - I_{12}) = (Y^{21}_{\text{res}} V_1 + Y^{22}_{\text{res}} V_2 + Y^{23}_{\text{res}} V_3) + i\omega C_{\text{p}} (2V_2 - V_3 - V_1) \\ I_3 = I'_3 + (I_{31} - I_{23}) = (Y^{31}_{\text{res}} V_1 + Y^{32}_{\text{res}} V_2 + Y^{33}_{\text{res}} V_3) + i\omega C_{\text{p}} (2V_3 - V_1 - V_2) \end{array}$$

and thus,

$$\vec{I} = Y_{\text{res}} \vec{V} + \begin{pmatrix} 2i\omega C_{\text{p}} & -i\omega C_{\text{p}} & -i\omega C_{\text{p}} \\ -i\omega C_{\text{p}} & 2i\omega C_{\text{p}} & -i\omega C_{\text{p}} \\ -i\omega C_{\text{p}} & -i\omega C_{\text{p}} & 2i\omega C_{\text{p}} \end{pmatrix} \vec{V},$$

such that we can write

$$\vec{I} = Y_{\text{total}} \vec{V}$$

where

$$Y_{\text{total}} = (\mathrm{I} + R Y_{\text{edge}})^{-1} Y_{\text{edge}} + \begin{pmatrix} 2i\omega C_{\text{p}} & -i\omega C_{\text{p}} & -i\omega C_{\text{p}} \\ -i\omega C_{\text{p}} & 2i\omega C_{\text{p}} & -i\omega C_{\text{p}} \\ -i\omega C_{\text{p}} & -i\omega C_{\text{p}} & 2i\omega C_{\text{p}} \end{pmatrix}.$$

Finally we calculate the scattering parameters of the system as a function of the angular frequency ω via the transformation:

$$S(\omega) = \left(Z^{-1} + Y_{\text{total}} \right)^{-1} \left(Z^{-1} - Y_{\text{total}} \right)$$

where $Z = Z_0 \mathrm{I}$. This expression is used to calculate S_{31} and S_{13} and their difference as shown in Fig. 6.5 (d). To compare our model to experimental data in Fig. 6.5 (c), where the background response at zero magnetic field has been subtracted, we normalize the results of the model by setting to $S = 0$ dB the response via just the parasitic path C_{p}. Thus a value of $S = 0$ dB in Fig. 6.5 (c) and 6.5 (d) represents the response of the system when no quantum Hall edge is present, similar to the experimental situation at zero field.

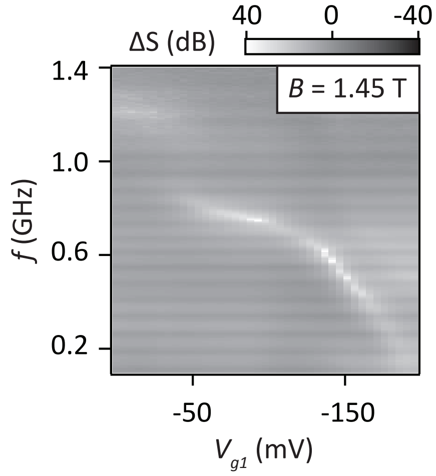

Figure B.5: Frequency response at positive magnetic field. ΔS = S_{13} - S_{23} frequency response with port-1 gate voltage V_{g1}. Data is taken at constant magnetic field B = 1.45 T

To qualitatively compare our model to the experimental data, we account for the 5 variables: the characteristic impedance Z_0, the parasitic capacitance C_p, the effective capacitance of the quantum Hall edge C_edge, the conductance of the edge $\sigma_\mathrm{edge} = 1/R_{xy}$, and the total dissipation R. To produce qualitative fits to the data, we fix Z_0 and vary R_{xy} and C_edge to align the peaks and dips to correspond to the EMP frequencies. Finally, we adjust C_p and R to vary the amplitude and width of the features in our model to fit the corresponding data. Although qualitative, the values of C_p and R chosen in the model are consistent with typical values for the parasitic capacitance and total dissipation estimated via transport measurements and geometric considerations.

B.7 Tuning non-reciprocity with gate voltage:

In Fig. B.5, isolation ΔS = S_{13}-S_{23} is measured at B = 1.45 T while the dc bias V_{g1} is varied. The direction of magnetic field is reversed with respect to Fig. 6.6 (c). Varying the dc bias on port 1 tunes the response between source and sink ports 3 and 2 respectively (as observed by a peak in ΔS), producing a qualitatively similar isolation frequency response to that shown in Fig. 6.6 (c).

C

Additional materials for Chapter 7: “Zero-field Edge Magnetoplasmons in a Magnetic Topological Insulator”

This section provides additional information and figures for the results outlined in Chapter 7. Materials and fabrication details are given, as well as bare transmission parameters. The power and temperature dependence for the device measured in Chapter 7 is presented at positive magnetisation, and the dc and rf response of a second sample are provided for comparison.

C.1 Fabrication details

The film used to make the circulator and corresponding Hall bar in Chapter 7 is seven quintuple layers of $(\mathrm{Cr_{0.12}Bi_{0.26}Sb_{0.62}})_2\mathrm{Te_3}$. The device shown in Fig. C.3 comprises eight quintuple layers of $(\mathrm{Cr_{0.12}Bi_{0.26}Sb_{0.62}})_2\mathrm{Te_3}$. In both cases, the film is grown on a semi-insulating GaAs substrate by molecular beam epitaxy and capped with alumina to protect the surface. We use photolithography to pattern a circular mesa with a diameter of 330 μm. We bake the Megaposit SPR 3612 photoresist at 80° C (to avoid possible damage to the film from overheating), and develop with MF CD-30 after exposure. To define the mesa, we etch the surrounding film via Ar ion milling. After patterning the contacts and ground plane with the same photolithographic procedure, we deposit a 5 nm Ti sticking layer followed by 120 nm Au using e-beam evaporation. The capacitive contacts are designed to be 20 μm from the edge of the circular mesa. For the primary device discussed in this work, the relative misalignment of the mesa and contacts is approximately 5 μm.

C.2 Transmission parameters prior to sample magnetisation

Fig. C.1 presents the transmission parameters, S_{21} and S_{23}, obtained as a function of microwave frequency prior to the application of a perpendicular magnetic field. These traces have been corrected here for amplification and attenuation added to the setup in order to provide a measure of insertion loss at the level of the device. Subtracting the bare S-parameter responses S_{23} from S_{21} (as shown in Fig. 7.2(d) of Chapter 7) yields a small residual response at $B = 0$ about 0 dB, attributed to slight differences in the line impedances of the two rf setups.

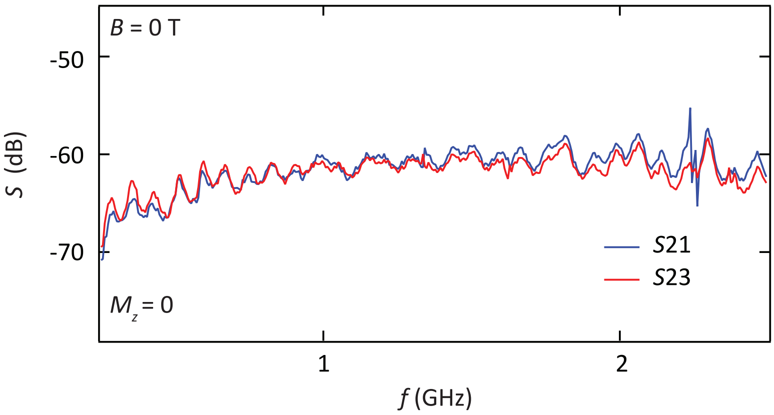

Figure C.1: S-parameter pre-magnetisation response. S-parameter transmission measurements taken prior to device magnetisation at cryostat base temperature of $\sim$ 20 mK, and applied port power of - 72 dBm.

C.3 Power and temperature dependence at $M_z = +1$

Figure C.2 depicts the effects of temperature and applied microwave port power on S_{21} and S_{23} at $B = 0$ once the sample has been magnetised in the positive direction, $M_z = +1$. The direction of magnetisation has been reversed with respect to the data in Figure 4 of the main manuscript. In accordance with a reversal of chirality, hot-spots are observed in the normalised $\Delta S21$ plots with both power and cryostat base temperature, corresponding to the $2l$ path in this configuration.

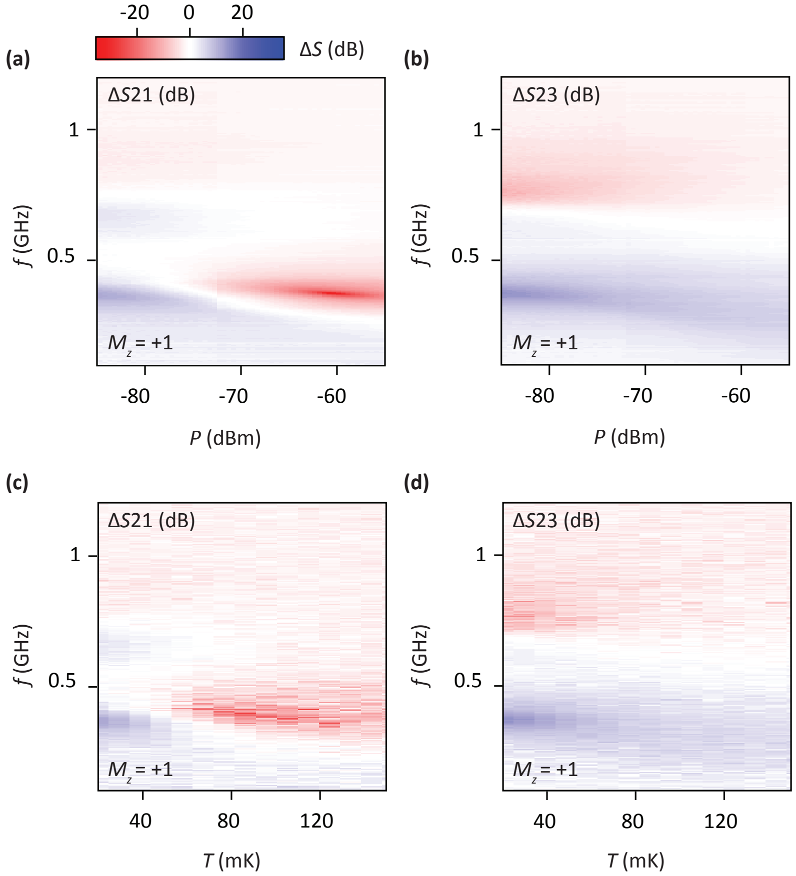

Figure C.2: Power and temperature dependence at $M_z = +1$. **(a)** and **(b)** Show the normalised S parameters in frequency as the applied microwave port power is stepped, while in **(c)** and **(d)** the cryostat temperature is increased. All measurements are taken at an applied magnetic field $B = 0$ after the sample has been magnetised in the positive direction.

C.4 Device B

Concurrent transport and S-parameter measurements as a function of external magnetic field are shown in Fig. C.3 for an alternate sample, denoted 'Device B'. Qualitatively similar behaviour is observed in this material (8 quintuple layers of $(\mathrm{Cr}_{0.12}\mathrm{Bi}_{0.26}\mathrm{Sb}_{0.62})_2\mathrm{Te}_3$), with fabrication methods and circulator geometry nominally identical to the device outlined in Chapter 7.

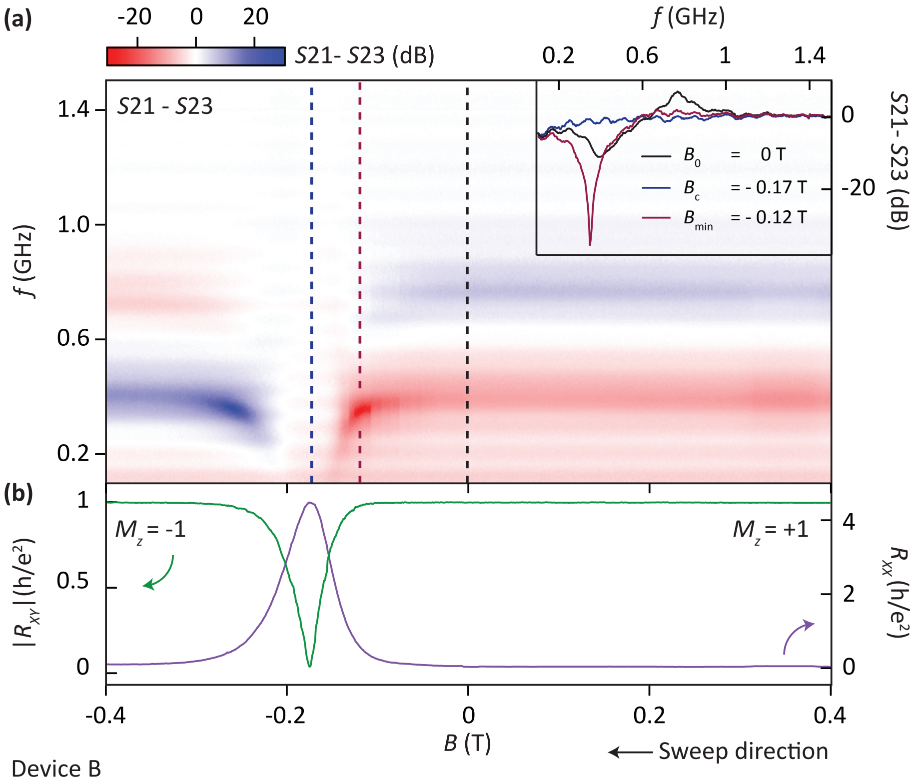

Figure C.3: Comparison of rf and dc response. $S21$-$S23$ microwave isolation spectrum **(a)** and Hall bar transport measurements **(b)** for Device B. Inset shows cuts taken at constant magnetic field values corresponding to dashed lines in (a).

D

Dilution fridge wiring

My arrival in the QNL coincided with that of 'Red Fridge', and, as such, much of my PhD has been spent wiring, designing components for and performing experiments in this particular cryogen-free dilution refrigerator (Leiden Cryogenics, CF-DR 500). The system has been configured for both quantum Hall and quantum dot measurements, with the aims of minimising noise and lowering the electron temperature. The electrical setup includes 8 rf and 74 dc lines, 2 full rf reflectometry set-ups, multiple filters, shields and a superconducting magnet mounted at 4K. This section provides a brief overview of the fridge configuration and components used for the experiments presented in this thesis, implemented by myself and others in the QNL.

D.1 rf setup

Radio frequency (rf) signals are commonly used for performing control and readout sequences on quantum dots, away from low-frequency noise. High bandwidth lines are required in order to direct these signals from room temperature to a device at the coldest stage of a dilution refrigerator. In our system, coaxial cable (coax) are fed into the outer vacuum chamber (OVC) of the cryostat from room temperature, via a custom-made KF-40 Al flange. Hermetically-sealed SMA bulkhead connectors are mounted to the flange, and are suitable for frequencies up to 18 GHz (Pasternack PE9184). Long, single lengths of stainless steel coax (inner/outer = SS/SS, 0.085” diameter) are attached to the connectors inside the cryostat.

In order to route the rf lines to the 4 K plate, a 3-stage probe designed by Leiden Cryogenics is passed through a clear-shot tube directly into the inner vacuum chamber (IVC) of the fridge. Gold press-plates on the probe make contact with the walls of the clear-shot. High conductivity copper braid is used to thermalise the outer casing of the coax to the probe stages. Multiple layers of aluminised mylar superinsulation are placed on the probe stages to reduce thermal radiation from reaching the lower temperature plates. Superinsulation is also used on the 4 K and 50 K plates within the fridge, with the bottom-most layer secured with conductive tape (Ruag BR-50).

Within the IVC, attenuators comprising parallel resistor networks are used at each temperature stage to thermalise the inner of the coax. These attenuators are connected directly to SMA feed-through connectors, which are tightened to copper baffles on each plate. The outer casings of the attenuators are wrapped with oxygen-free copper braid which is secured to the plates. Around 30 dB of attenuation is typically added to the rf lines down the fridge. 0 dB thin-film attenuators from XMA corp are also used on the lowest temperature stages.

A directional coupler (e.g. Mini Circuits ZFDC 15-5S) on the ~ 20 mK stage enables rf-reflectometry measurements to be performed. A custom-designed copper coldfinger and shield are mounted to the mixing chamber, and sealed with Al Mylar tape. Superconducting NbTi coax is used to transport the reflected signal from the device towards

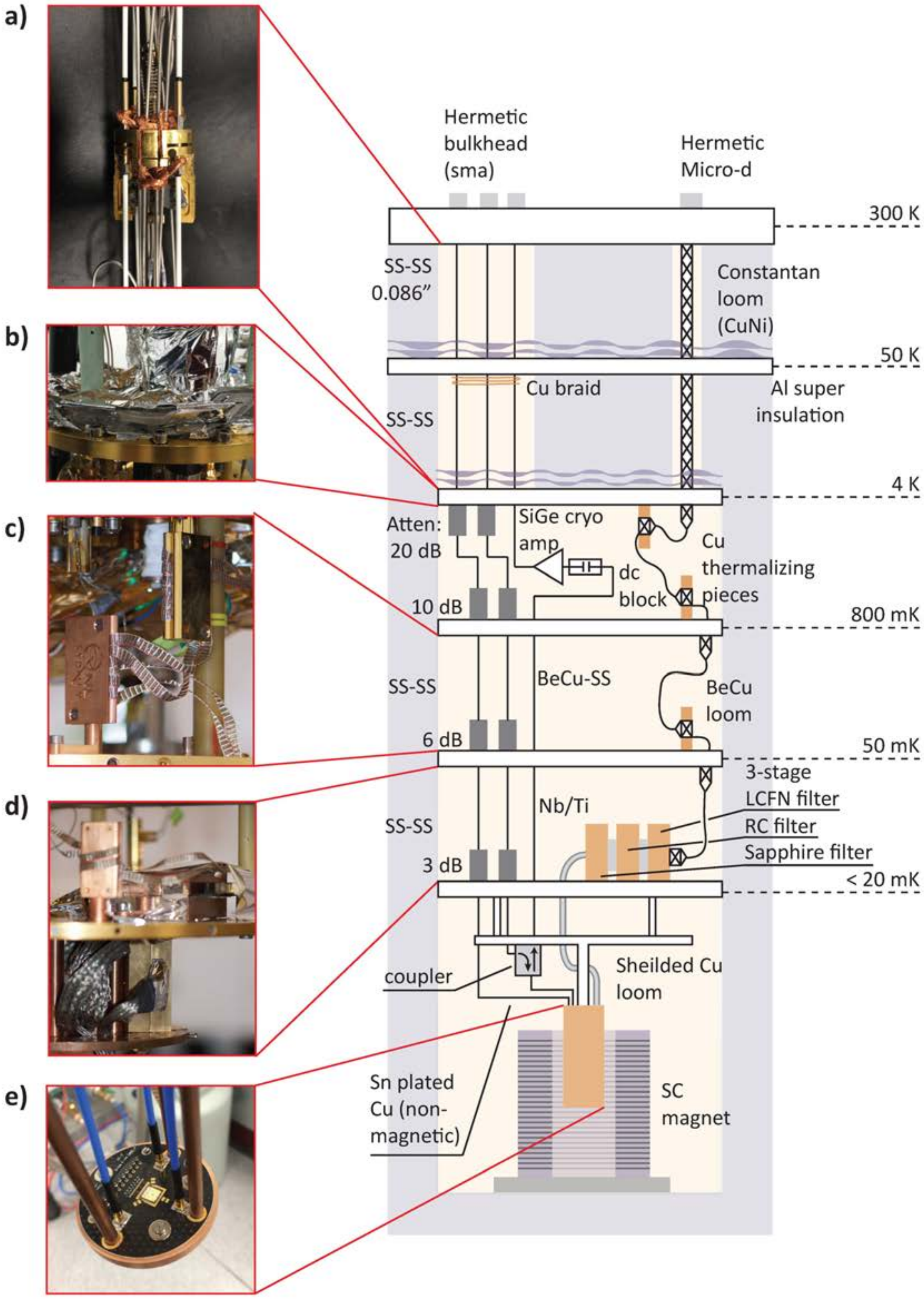

Figure D.1: Dilution fridge wiring. Standard dc and rf wiring set-up used in the QNL ‘Red Fridge’ (Leiden Cryogenics CF-DR 500, with Cryomech PT415 compressor).

the 50 mK plate. Between the 50 mK and 4 K plates, BeCu coax is used[1].

For frequencies up to 2.5 GHz, we typically use a CITLF1 series amplifier from the Weinreb group at Caltech[2] to boost the reflected rf wave. This is a SiGe low noise amp, with a resistive feedback mechanism providing good input match and high gain stability ($\sim$ 40 dB gain) and a noise temperature of around 7 K at 1 GHz. The amp casing is mounted onto a custom made copper bracket which is thermally anchored to the the 4 K plate. A dc block is placed on the input of the amp (Pasternack PE8225). Tin-plated copper coax is used to connect the output of the cryo-amp to stainless steel coax on the 4 K rf bank, which then connects to coax on the rf probe and back up to room temperature.

D.2 dc setup

Constant bias voltages are required to isolate quantum dot systems in semiconductors. Applying negative dc voltages on electrode gates depletes regions of electron gas, creating small residual puddles of charge. Ohmics annealed from the sample surface make resistive contact with the 2-dimensional electron gas (2DEG), and can be used to source and sink current. These contacts also enable a ground potential to be defined, and for the electrons to be thermalised to the coldfinger of the fridge.

Constantan (55% copper, 45% nickel) loom wire is used to feed dc signals from room temperature to the 4 K plate due to its high electrical and low thermal conductivity. The loom wire is tightly wrapped around copper thermalising plates at the 4 K, 800 mK, and 50 mK stages. The thermalising plates are plated with gold to prevent oxidation and improve the solid-solid interface for heat transfer. 3-stage Mini Circuits LCFN filters with sequential frequency cut-offs (5000 MHz, 1450 MHz, 80 MHz) are used to low-pass the signals. The signals then passed through a 1 kHz cut-off *RC* filter bank. Thin-film resistors are used in the filters as they are not found to vary significantly at low temperatures. Likewise we use NP0 ceramic capacitors which have

---

[1] BeCu has a lower thermal conductivity than copper but comparable electrical properties.

[2] Now Cosmic Microwave Technology.

a low effective series resistance and stable capacitance when cooled. The final stage of filtering comprises a sapphire heat sink, with meandering, annealed Au tracks for improved thermalisation. These components were engineered based on designs from the Marcus Lab at Harvard[1]. All three filter stages are mounted in radiation-tight copper boxes and are connected to each other via shielded cables to ensure a continued ground connection. The boxes are then anchored to the mixing chamber plate in the fridge using stainless steel screws. Inside the coldfinger shield, dc lines are connected to a printed circuit board (PCB) via tightly wound copper loom to minimise inductive coupling.

In quantum Hall plasmonics experiments, a two-layer PCB with a gold underside is mounted to a copper stage with non-magnetic stainless steel screws, and directly connected to the mixing chamber plate. Copper is chosen both because of the high thermal conductivity and because it is non-magnetic. This configuration serves to thermalise the PCB and electrically ground the lines to the fridge. The chip is silver pasted directly onto the copper mount in a recess in the middle of the PCB. Ground planes on the PCB are connected to the chip via high density Al bond wires.

---

[1] Now QDev at the University of Copenhagen.

E

Schematics for mesaurement setups

This section includes measurement schematics alongside brief descriptions of the experimental setups used for the quantum dot, and quantum Hall plasmonics experiments presented in this thesis.

E.1 Quantum Hall plasmonics experimental setup

Dc transport measurements are performed on a standard Hall bar structure using a series of 3 lock-in analysers (Stanford Research Systems, SR 830). A low frequency excitation is applied to a source ohmic ($\sim$ 17 Hz) via a 10 MΩ resistor to ensure a constant current through the device. This frequency also provides a phase-locked reference signal for the two lock-ins used to measure the voltage difference in the transverse or longitudinal directions across another set of ohmics. Differential voltage and current pre-amps are used prior to feeding the voltage and current signals back into the lock-ins. A superconducting solenoid magnet mounted at 4 K (American Magnetics Inc.) is ramped slowly at $\sim$ 0.005 A/s with an Oxford MercuryiPS system power source (high current stability, bi-polar) during data sweeps in order to minimise eddy current heating.

A vector network analyser (VNA) is used to perform rf transmission measurements across coplanar tracks on circulator structures. Low powers are used ($\sim$ 80 dBm at the level of the device) and components are chosen in the set-up (including cryo amps and couplers) to optimise measurements in the operating band from $\sim$ 100 MHz - 2.5 GHz.

The printed circuit boards (PCBs) used for the quantum Hall (QH) plasmonics experiments throughout this work were designed in the QNL. Each PCB is fabricated from Rogers 6006 high-frequency laminate and comprises three 50 Ω coplanar transmission line ports for rf probing, along with 12 dc lines. Plated fencing vias join the ground connections on the top layer to the exposed ground plane on the underside. The PCB is mounted to a copper platform which is bolted to the mixing chamber stage of the dilution refrigerator. High-density Al bondwires provide a near-continuous ground from the PCB to the QH chip to reduce spurious modes. A recess in the centre of the PCB enables the QH chip to be silver-pasted directly to the copper underneath, for improved thermalisation of the lattice.

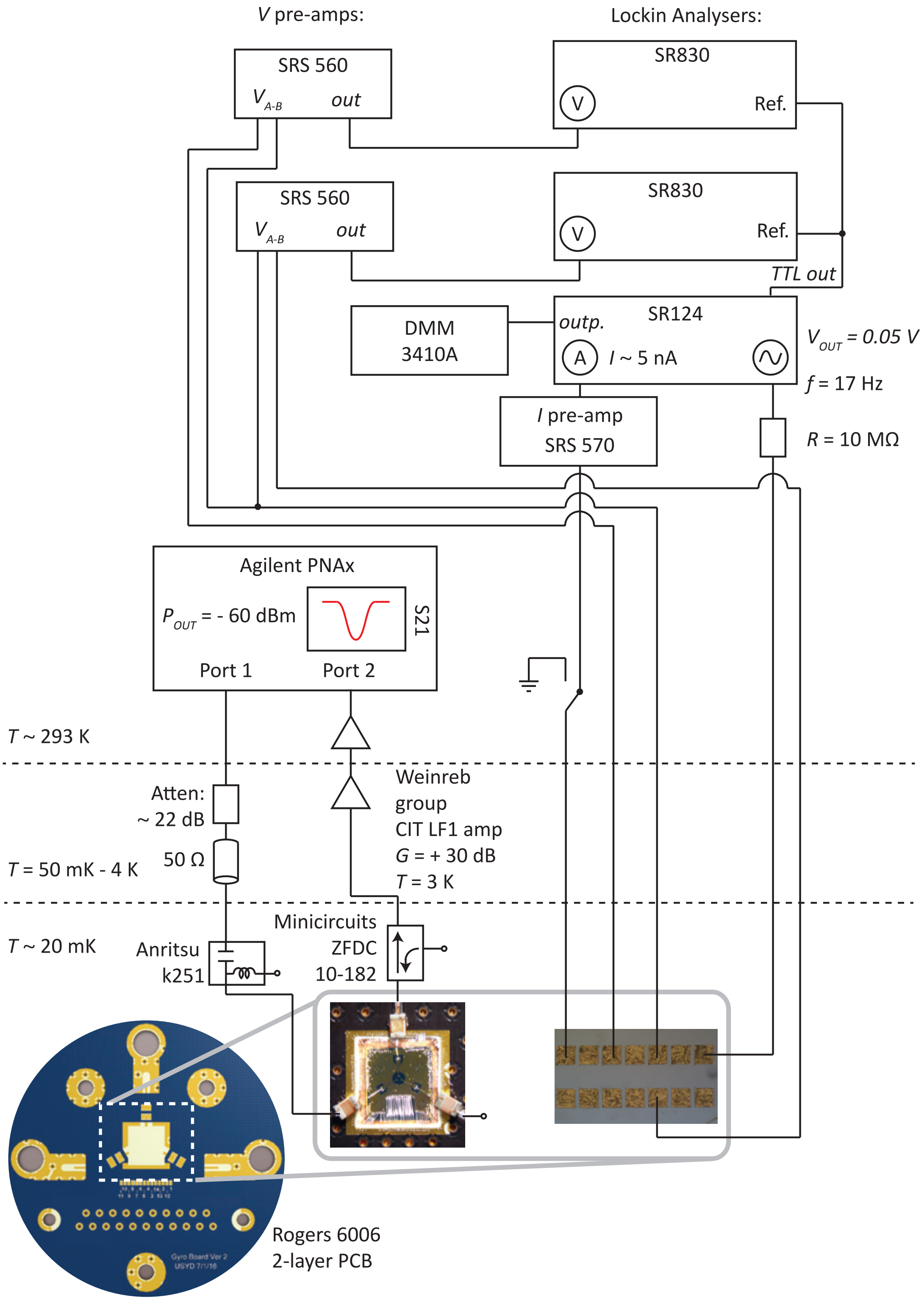

Figure E.1: Quantum Hall measurement schematic. Standard measurement setup for quantum Hall plasmonics experiments in the QNL.

E.2 Quantum dots readout experimental setup

The rf-readout set-up for dispersive gate sensing can effectively be divided into two sections, which are later combined - the rastering part and the readout part. A 66 Hz raster is applied with an arbitrary waveform generator (AWG) and combined with a static dc offset voltage from a digital-to-analog converter DAC[1], using a home-made adder box with integrated filters on the dc side. This signal is then connected through a break-out box to an electrode gate on the quantum dot device-under-test.

For the readout setup, the resonant frequency of the relevant LC tank circuit, f_0, is first measured with a network analyser at a sensitive gate potential configuration. The readout input line to the device is then connected to a signal generator, which outputs a frequency equal to f_0. A low power, typically $\sim$ -100 dBm at the level of the device, is used. The reflected signal from the resonant circuit travels through a coupler and low-noise cryo-amp to boost the signal, and is directed into a home-made, shielded demodulation box. After filtering, the signal is further amplified at room temperature, and then mixed with a local oscillator (LO) frequency. This LO signal can either be split from the original f_0, or output from a second, phase-locked source. The advantage of this is that the high powers required to drive the components in the demodulation setup can be set separately from the low power applied to the device, and a phase difference can be adjusted digitally between the two sources in order to tune the resultant IF signal amplitude.

The demodulated signal is then low-pass filtered to remove high frequency $(2f)$ components and passed through a voltage pre-amp before being directed (via a shielded cable) into a sampling oscilloscope. The oscilloscope is triggered off the same 66 Hz signal applied to the rastered gate, and sampled at a rate of 1 divided by this frequency such that the time scale of the oscilloscope canvasses the full raster range in voltage space.

The PCBs used for the quantum dot measurements throughout this work were designed in the QNL, and incorporate a high density of signal interconnects, along with

---

[1] We use a multi channel decaDAC from the Electronic Instrument Design Lab at Harvard University

integrated dc line filters in a modular platform (see Refs. [81, 195] for detailed specifications and characterisation). Each PCB includes a motherboard comprising 7 layers of Rogers 3003 laminate, an rf ‘fuzz button’ interposer and an FR4 chip-holder daughterboard. The motherboard includes 74 dc connections, 32 high-bandwidth feed lines and 4 microwave lines suitable for fast pulsing.

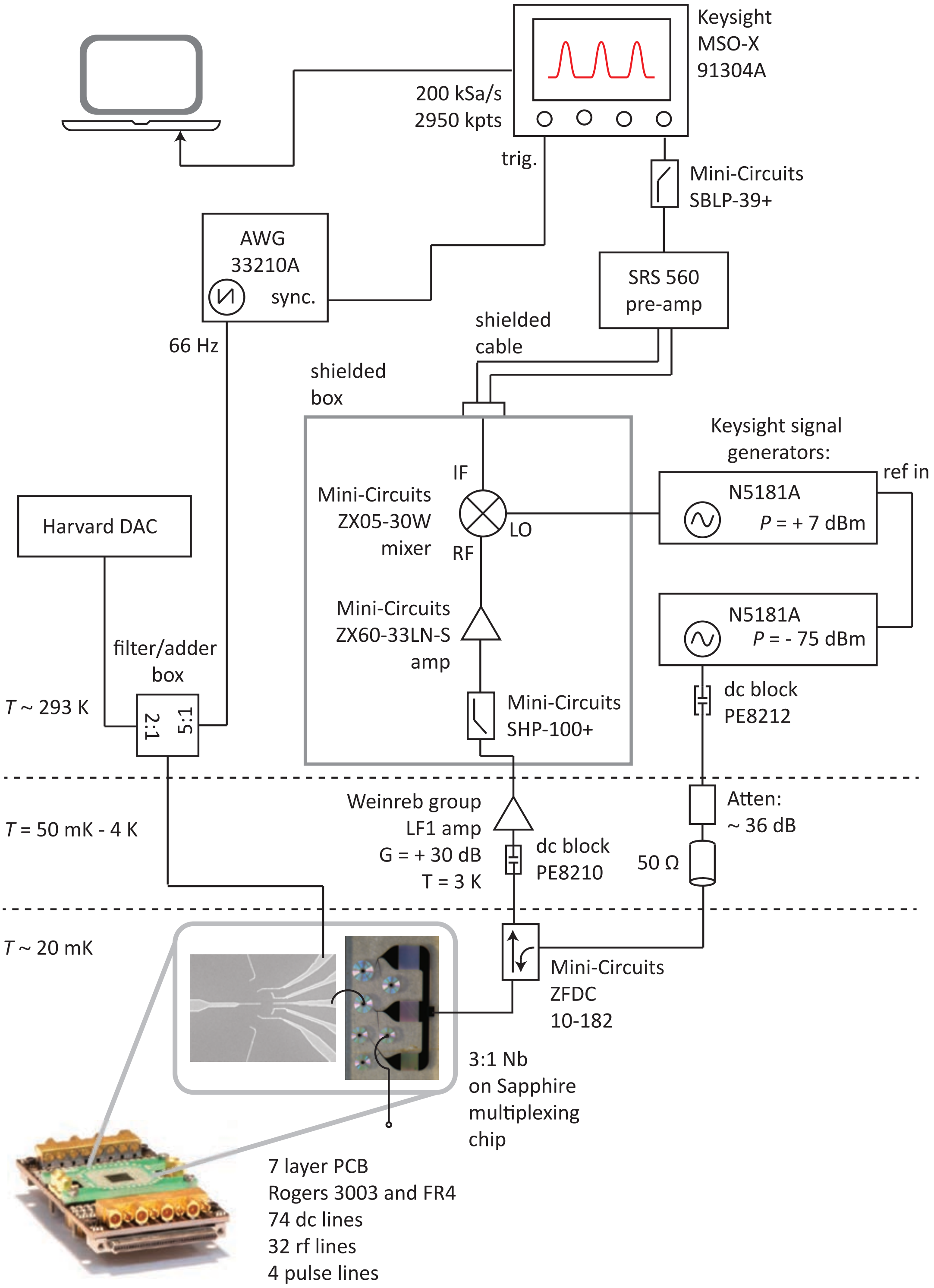

Figure E.2: Quantum dots measurement schematic. Standard measurement setup for quantum dot experiments in the QNL.

F

Nanofabrication

While many aspects of nanofabrication are considered something of a black art, it is a truth universally acknowledged that the more vigilant you are in the cleanrooms, the better your samples (and data) will look. As the recipes used for the fabrication of quantum dot devices in our lab are largely unchanged from those detailed in previous QNL theses [196, 197], I will not go over those steps here. Rather, this section details the QNL fabrication process for making chips suitable for quantum Hall measurements. The wafers used for such experiments typically differ from standard 'dot' material by their high mobility, μ. This increase in mobility is often due to the large distance between the electron plane and the dopant atoms. As a result, such heterostructures can have 2DEGs buried especially deep below the surface. For example, the recipe presented here is optimised for 2DEGs at a depth of $\sim$ 450 nm. Fabricating on these materials has its own challenges, including evaporating metals over deep etched trenches, and making low resistance ohmic contacts for measurements in high magnetic fields. The recipe that is currently used for fabricating EMP devices in the QNL was devised after performing a number of diagnostic tests, adapting standard processes, and by gleaning tips from the detailed notes in PhD theses from other groups. In this spirit, I shall endeavour to do the same here.

F.1 Step-by-step fabrication notes

The following steps refer to the processes developed and equipment used in the Australian National Fabrication Facility (ANFF) UNSW node. The terms ‘wafer’ or ‘heterostructure’ here refer to 2 inch GaAs-AlGaAs wafers grown by molecular beam epitaxy (MBE).

F.1.1 Cleaning and scribing

The quality of a chip can have huge implications for the performance of the finished device, and so the importance of the initial cleaning process can not be overstated. The first step is to scribe and cleave the sample. This step is also crucial in order to keep track of the crystallographic axis, and where on a wafer a sample came from. Due to inhomogeneities in the density and mobility across a wafer, as a general rule using chips from the centre 1 inch of a 2 inch wafer is preferred.

We use a manual diamond scribing tool to accurately measure and cleave a single chip. When using the Karl Suss wafer scriber, clean the sample stage first, then make sure that the vacuum is turned on. The wafer should not move around or swivel when pushed gently with tweezers. If scribing across a whole wafer, it is a good idea to keep the width constant along the minor or major axis directions so that the orientation is always clear for any given chip. When deciding how large to scribe a chip, the size of the pattern needs to be considered as well as leaving space around the edges for where spun photoresist collects, or where a clamp will be placed. The cleaving block should be used to cleanly split the chip. The strip or wafer should be aligned onto the blade, and even pressure applied to either side with cleanroom wipes placed over the chip. Always be careful to clean up any gallium residue. Drawing a picture of the unique edges and imperfections on a chip (viewed under an optical microscope) will help to identify it when processing multiple samples at once.

As a general rule, one should assume that everything in the cleanrooms is contaminated until otherwise cleaned. It is good practice to clean your own beakers both before and after use- generally a good sonicate with acetone, and then isopropanol (IPA) is sufficient (concentrating of the rim and the inside of the beaker). Tweezers should be cleaned by spraying acetone and then IPA pointing downwards into the solvent waste container. Soft, carbon fibre tipped tweezers are recommended for handling small GaAs chips to avoid scratching the surface or edges.

The next step in the chip preparation process is gallium removal. The wafers we use from the Manfra group have gallium on the underside to act as a sticking layer during the growth process. Removing this layer is important both for contamination reasons, and also to ensure that the chip will sit flat during the fabrication steps. If the bottom of a chip has residue on it, it will not adhere well to vacuum stages during lithography, or lay flush when clamped during evaporation. It is helpful to have a dummy wafer for this process, rather than using a glass slide. One technique is to put a drop of resist onto the dummy wafer, and then place the chip face down onto it. The stack is then baked on a hotplate at 125° C for roughly a minute. After the gallium has softened, it can be wiped off with a cleanroom q-tip, or by using a piece of filter paper folded into a point and dipped in acetone. The dummy/chip stack can then be sprayed with acetone in order to loosen the chip and separate it from the larger wafer. The chip should then be placed into a beaker full of N-Methylpyrrolidone (NMP) at 80° C for about 10 minutes, followed by 5 minutes in the sonicator. These steps are repeated in acetone and then IPA using dedicated beakers for the initial cleaning stage. When this is complete, the chip can be dried carefully with the compressed, dry air (CDA) gun and placed under a microscope to inspect the surface. If there are any contaminants the cleaning process should be repeated, making sure to use fresh NMP and solvent. Finally, the chip should be baked on a hotplate at 200° for 5 minutes to remove any residual moisture from the surface.

F.1.2 Mesa etching

The next series of steps should all be completed in a single day in order to produce the best quality ohmic contacts. The rationale for this is to prevent oxidation along the sidewall of the fresh mesa etch, which could impede the annealing process.

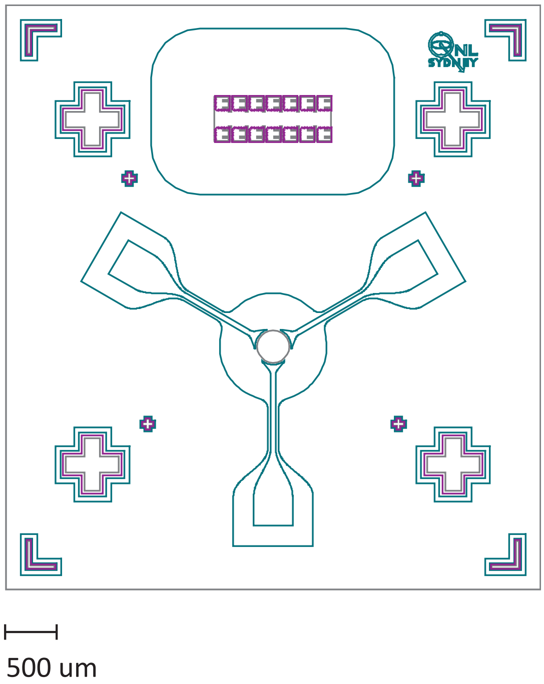

Figure F.1: QHE circulator mask. The different layers are overlayed in this image to illustrate what the final design should look like. The mesa is is grey, ohmics are purple, and optical gates are shown in green. Alignment markers for each layer enable the different structures to be placed with a relative misalignment error of $\sim \pm 1$ μm.

First, a layer of photoresist must be spun and exposed. Even after the initial cleaning process, it is always a good idea to spin clean chips with acetone and IPA prior to depositing resist. In addition, it is good practice to test the spinner vacuum first with a dummy wafer roughly the same size as the chip that will be patterned. When spin cleaning, do not spray the acetone from the bottle until the chip is spinning at a high speed (over $\sim$1000 rpm), as the liquid could prevent the formation of a vacuum and cause the chip to fly off when the spin speed increases. After spin cleaning, fill a pipette with AZ-6612 resist and squeeze out any bubbles. Drop a few droplets of resist onto the chip directly while the spin speed is at 500 rpm. For the recipe detailed in section F.2, this should result in a layer thickness of around 1.5 μm. After the spinning is complete, bake at 95° C for 60 s.

The next step is using optical lithography to define a pattern on the chip. We use a 6 inch soda lime clear field mask, with a chrome backing layer. An example design used for the quantum Hall structures in this thesis is shown in Fig. F.1. Depending on the mask aligner used, the quality of the vacuum, and the size of the chip, blue clean room sticky-tape may also be required to improve the adhesion of the chip to the stage. When the chip is loaded into the aligner, the mask acts like a stencil such that only certain areas of the chip are exposed to the UV light. This exposure (wait time of 1.7 s with 10 mW/cm^{-2} lamp power) weakens the resist by breaking molecular chains. These areas are then washed away using AZ MIF 300 developer for 40 s.

Once the resist has been developed, it is important to obtain a measure of the height across the chip- this will enable you to test the etch rate. The Dektak profilometer is used for this purpose, and measurements should be taken with the stylus on medium force over various features on the sample to obtain an accurate profile. Once these values have been recorded, the device can then be etched with a dilute piranha solution (a 240:8:1 mix of H_20:H_20_2:H_2S0_4). While this solution can be pre-made, best results are almost always obtained when using a freshly prepared acid etch solution.

The piranha solution tends to etch GaAs chips at a rate of about 2 nm/s, although in practice this can vary from about 1.8 - 3 nm/s. When using deep heterostructures, a good technique is to do an initial etch for 100 s, and then re-measure the height of the sample with the Dektak. This enables the etch rate to be easily determined, and then a second etch can be performed to make up the rest of the depth. While some recipes suggest only etching to a depth just below the first layer of dopants in a heterostructure, we have found that this can lead to resistances of a few kΩ in between mesas. Because of this, it is worth etching down below the quantum well (overshooting by around 15%) in order to ensure electrical isolation between structures.

F.1.3 Ohmic contacts

After etching and recording carefully the mesa height, the chip is ready for patterning ohmic contacts. It is a good idea to repeat the three-stage clean (warm NMP, acetone and IPA, with sonication) at this point as the chip should be in pristine condition before annealing. In order to ensure the the ohmic metal is easily removed after evaporating, we use a lift off resist (LOR 5A) underneath the standard AZ-6612 resist to form an undercut layer. However, one issue when using thick bilayer resist is that edge beads can more easily form around the sample perimeter. These can be carefully removed or flattened using tweezers under a microscope, or by loading a chip into the aligner and letting the surface come into contact with a blank section of the mask. This technique serves to even the bubbles at the edges of the chip. It is also a good idea to try to align the chip as best as possible with the mask before starting the move the micrometer knobs.

The ohmic patterns used in the QNL differ from those used in standard dot experiments, with the aim of providing low resistance contact to the 2DEG even at high magnetic fields. To this end, the mesa underneath the ohmics is patterned into a ‘key’ shape with cut-outs either in-line or at 90° angles to the crystallographic axis of the chip (see Fig. F.2). The ohmic metal structures overlap the mesa in order to enable annealing via the top and sidewall surfaces, and have a ‘postage stamp’ cut-out pattern to facilitate better 2DEG contact and annealing through opening up access to multiple tunnelling paths.

Once the chip is exposed and developed, it can be carefully loaded onto the sample stage in the thermal or e-beam evaporator. The chip should be clamped evenly along one side at the centre of the stage and away from the designs so that it sits flat. When

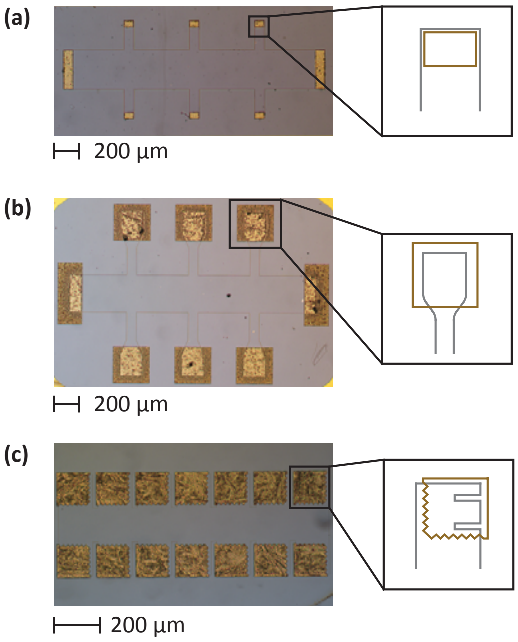

Figure F.2: Evolution of ohmic contacts. In **(a)**, the ohmic metal pattern and mesa are designed to be the same size. Small misalignment between the layers however can lead to the contacts becoming insulating at high magnetic fields where the QH edge can travel around the ohmic. The design in **(b)** improves upon this by overlapping the ohmics on top of the mesa. This also has the advantage that the metal can be annealed both top-down and via the side wall, which tends to give lower resistances. The design in **(c)** was adapted from Ref. [198]. A cut-out mesa pattern along with zig-zag edges on the ohmic contacts provides multiple tunnelling channels and produces reasonably low contact resistances.

loading the boats and materials, gloves should be changed and the tweezers cleaned with IPA between handling different metals in order to avoid contamination. It is also a good idea to load multiple boats of nickel (or titanium when patterning gates), as these metals tend to outgas more than others and the boats are more likely to crack. In order to get an accurate height reading, the crystal on the evaporator should be changed if the reading is $> 20\%$. After waiting at least 1 hour (preferably overnight) for the chamber to pump down to around 5×10^{-6} Torr, the power supply can be turned on to begin the evaporation process.

The ohmic layer stack should be chosen such that the total height is greater than the etch depth of the mesa. Normally, a 60 Å Ni sticking layer is used, and capping layers of 100-200 Å Ni and 500 Å Au. The Au/Ge eutectic layer in the middle is chosen to make up the height difference with a thickness ratio of 2:1 (corresponding to an atomic weight ratio of about 88:12). When the evaporation is finished, the chip should be placed in warm NMP at 80° C for around 15 minutes.

The ULVAC MILA rapid thermal annealer is used to anneal the ohmic contacts in an environment of forming gas (4% Hydrogen and 96% Nitrogen). Best results have been obtained when using a SiC coated carbon susceptor with thermocouple assembly. For large ohmic layer stacks like those used for QH devices, the anneal time tends to be longer than for dot devices, $\sim$ 2 minutes 10 s at 430° C (the melting temperature of the Au:Ge eutectic stack should be 360° C). Good ohmics will look obviously bubbly after annealing, with roughly uniform sized bubbles and no dark spots.

F.1.4 Optical gates

The final stage requires the pattering of large electrode gates. When evaporating metallic gates that will overlap with the mesa, it is important that the height of the metal deposited is greater than the depth of the etch, otherwise there will be an electrical break (this is another reason why it is important to use the Dektak and carefully record the heights of samples). We therefore use a thick lift-off resist, LOR 20B, for this procedure. While the plasma asher is often used prior to evaporating optical gates in quantum dot structures, there is some evidence to suggest that this can reduce the quality and mobility of quantum Hall samples, and so this step is left out.

F.2 Device fabrication recipe

Scribing

- Equipment: Karl Suss wafer scriber
- Standard QHE circulator chip size is 5.5 mm x 6.5 mm
- Cleave on block after scribing (use filter paper to apply pressure)

Gallium removal

- Stick chip (gallium side up) to dummy wafer and glass slide using a drop of AZ6612
- Heat on hotplate at 120 degrees for about 60 s
- Use a cleanroom q-tip dipped in acetone to remove the melted gallium, or folded filter paper
- Sonicate in acetone to un-stick the chip from the dummy wafer
- Dip chip in 30 % HCl if necessary

Cleaning

- Place chip in warm NMP for 5 mins, sonicate for 5 mins
- Place chip in acetone, sonicate for 5 mins
- Rinse chip in IPA
- Heat chip on hotplate at 200 degrees for 5 mins or longer

Spinning single layer resist

- Equipment: Headway Research PWM32 spinner
- Use the following recipe for AZ6612 positive resist:
  1. 500 rpm at 500 rpm/s for 5 s
  2. 10000 rpm at 4000 rpm/s for 20 s
  3. 4000 rpm at 4000 rpm/s for 20 s
  4. 0 rpm at 1000 rpm/s for 0 s
  5. Bake at 95 degrees on hotplate for 60 s

Optical lithography

- Equipment: Karl Suss MA6 mask aligner
- Lamp power should read 299 W
- Use the following program settings for exposure: Hard contact mode, 60 μm alignment gap, 10 s wait time, 1.7 s exposure time

Resist developing

- Fill a clean beaker with MIF300 from the stock bottle, alongside a beaker of DI water
- Place chip in MIF300 for 40 s (stirring the chip around with tweezers), then water for 20 s
- Dry with CDA hose

Measuring resist height

- Equipment: Dektak 3030 surface profiler
- Measure across a few different areas on the chip with force at level 4, then normalise the background to determine the height

Mesa etching

- Prepare solution of 240 mL H20, 8 mL H202, 1 mL H2SO4,
- Stir, then tip etch solution into a smaller beaker
- Etch for 50 s, then rinse in water for 15 s
- Calculate etch rate after measuring with dektak (should be about 2.5 nm/s)
- Place chip back into etch solution as needed
- Clean chip with NMP, acetone and IPA

Spinning bi-layer resist

- Equipment: Headway Research PWM32 spinner

- Use the following recipe for LOR 7B resist (ohmics) or LOR 20B resist (gates):
  1. 500 rpm at 500 rpm/s for 5 s
  2. 10000 rpm at 10000 rpm/s for 1 s
  3. 6000 rpm at 4000 rpm/s for 60 s
  4. 0 rpm at 1000 rpm/s for 0 s
  5. Bake at 170 degrees for 5 mins
- follow with a single spin using the AZ6612 standard recipe

Evaporating ohmics

- Equipment: Kurt J Lesker thermal evaporator
- Use following recipe for ohmic layer stack:
  1. 60 Å Ni at 0.5 Å/s
  2. 1350 Å Ge at 3 Å/s
  3. 2700 Å Au at 5 Å/s
  4. 200 Å Ni at 1 Å/s
  5. 500 Å Au at 3 Å/s

Annealing ohmics

- Equipment: ULVAC MILA 5000 thermal annealer
- Vent with nitrogen gas for 3 mins before loading sample, then forming gas for 3 mins after loading sample. Evaporate using the following steps:
  1. Ramp to 130 degrees over 10 seconds
  2. Hold at 130 degrees for 1 minute
  3. Ramp to 430 degrees over 8 seconds
  4. Hold at 430 degrees for 130 seconds
- As soon as the anneal process has finished, vent the chamber with nitrogen gas

Evaporating large gates

- Equipment: Lesker PVD75 e-beam evaporator
- Evaporate large gates using the following recipe:
  1. 100 Å Ti at 1 Å/s
  2. 4000 Å Au at 5 Å/S

Bibliography

[1] R. P. Feynman, "Simulating physics with computers," *International journal of theoretical physics*, vol. 21, no. 6, pp. 467–488, 1982. 3

[2] P. W. Shor, "Polynomial-time algorithms for prime factorisation and discrete logarithms on a quantum computer," *SIAM J. Comput.*, vol. 26, pp. 1484–1509, 1997. 3

[3] L. K. Grover, "Quantum mechanics helps in searching for a needle in a haystack," *Phys. Rev. Lett.*, vol. 79, pp. 325–328, 1997. 3

[4] K. v. Klitzing, G. Dorda, and M. Pepper, "New method for high-accuracy determination of the fine-structure constant based on quantized Hall resistance," *Physical Review Letters*, vol. 45, no. 6, p. 494, 1980. 10, 30, 41

[5] D. C. Tsui, H. L. Störmer, and A. C. Gossard, "Two-dimensional magnetotransport in the extreme quantum limit," *Physical Review Letters*, vol. 48, no. 22, p. 1559, 1982. 10, 39

[6] H. L. Störmer, "Nobel lecture: the fractional quantum Hall effect," *Reviews of Modern Physics*, vol. 71, no. 4, p. 875, 1999. 10

[7] C. Kittel and D. F. Holcomb, "Introduction to solid state physics," *American Journal of Physics*, vol. 35, no. 6, pp. 547–548, 1967. 10

[8] B. K. Tanner, *Introduction to the Physics of Electrons in Solids.* Cambridge University Press, 1995. 10, 11

[9] D. Ferry and S. M. Goodnick, *Transport in nanostructures.* No. 6, Cambridge university press, 1997. 10, 34, 40

[10] T. Ihn, *Semiconductor Nanostructures: Quantum states and electronic transport.* Oxford University Press, 2010. 10, 12, 14, 33, 34, 39, 40

[11] C. Harmans, “Mesoscopic physics: An introduction,” *Delft University*, 1997. 10, 11, 12

[12] M. Kuno, *Introductory Nanoscience.* Garland Science, 2011. 11

[13] C. W. J. Beennakker and H. van Houten, “Quantum transport in semiconductor nanostructures,” *Solid State Physics*, vol. 44, pp. 1–228, 1991. 13

[14] R. Hanson, L. P. Kouwenhoven, J. R. Petta, S. Tarucha, and L. M. K. Vandersypen, “Spins in few-electron quantum dots,” *Rev. Mod. Phys.*, vol. 79, pp. 1217–1265, 2007. 13, 18, 19, 20, 21, 22, 52, 59, 66, 122

[15] J. D. Watson, *Growth of low disorder GaAs/AlGaAs heterostructures by molecular beam epitaxy for the dtudy of correlated electron phases in two dimensions.* PhD thesis, Purdue University, May 2015. 14

[16] M. J. Manfra, “Molecular beam epitaxy of ultra-high-quality AlGaAs/GaAs heterostructures: Enabling physics in low-dimensional electronic systems,” *Annu. Rev. Condens. Matter Phys.*, vol. 5, no. 1, pp. 347–373, 2014. 16

[17] L. P. Kouwenhoven, C. M. Marcus, P. L. McEuen, S. Tarucha, R. M. Westervelt, and N. S. Wingreen, “Electron transport in quantum dots,” *Proceedings of the NATO Advanced Study Institute on Mesoscopic Electron Transport*, pp. 105–214, 1997. 19

[18] Y. V. Nazarov and Y. M. Blanter, *Quantum transport: introduction to nanoscience.* Cambridge University Press, 2009. 20, 25

[19] L. P. Kouwenhoven, “Quantum adiabatic electron transport in ballistic conductors,” in *Physics of Low-Dimensional Semiconductor Structures*, pp. 463–498, Springer, 1993. 24, 25

[20] M. Büttiker, “Quantized transmission of a saddle-point constriction,” *Physical Review B*, vol. 41, no. 11, p. 7906, 1990. 25, 78

[21] B. Van Wees, H. Van Houten, C. Beenakker, J. G. Williamson, L. , D. Van der Marel, and C. Foxon, “Quantized conductance of point contacts in a two-dimensional electron gas,” *Physical Review Letters*, vol. 60, no. 9, p. 848, 1988. 25, 30, 78

[22] D. Wharam, T. Thornton, R. Newbury, M. Pepper, H. Ahmed, J. Frost, D. Hasko, D. Peacock, D. Ritchie, and G. Jones, “One-dimensional transport and the quantisation of the ballistic resistance,” *Journal of Physics C: solid state physics*, vol. 21, no. 8, p. L209, 1988. 25, 30, 78

[23] H. van Houten, C. Beenakker, and B. Van Wees, “Quantum point contacts,” *Semiconductors and Semimetals*, vol. 35, pp. 9–112, 1992. 25

[24] L. Glazman and A. Khaetskii, “Quantum conductance of a lateral microconstraint in a magnetic field,” *Journal of Physics: Condensed Matter*, vol. 1, no. 30, p. 5005, 1989. 25

[25] R. Landauer, “Conductance from transmission: common sense points,” *Physica Scripta*, vol. 1992, no. T42, p. 110, 1992. 26

[26] A. Micolich, “What lurks below the last plateau: experimental studies of the 0.7× 2e2/h conductance anomaly in one-dimensional systems,” *Journal of Physics: Condensed Matter*, vol. 23, no. 44, p. 443201, 2011. 26, 78

[27] D. J. Reilly, C. M. Marcus, M. P. Hanson, and A. C. Gossard, “Fast single-charge sensing with a rf quantum point contact,” *Appl. Phys. Lett.*, vol. 91, p. 162101, 2007. 27, 55, 66, 67, 72, 92, 130, 131, 153

[28] J. K. Jain, *Composite fermions.* Cambridge University Press, 2007. 33, 34, 40

[29] B. I. Halperin, “Quantized Hall conductance, current-carrying edge states, and the existence of extended states in a two-dimensional disordered potential,” *Physical Review B*, vol. 25, no. 4, p. 2185, 1982. 34

[30] S. M. Girvin, “The quantum Hall effect: novel excitations and broken symmetries,” in *Aspects topologiques de la physique en basse dimension. Topological aspects of low dimensional systems*, pp. 53–175, Springer, 1999. 36

[31] D. Chklovskii, B. Shklovskii, and L. Glazman, “Electrostatics of edge channels,” *Physical Review B*, vol. 46, no. 7, p. 4026, 1992. 36

[32] R. B. Laughlin, "Anomalous quantum Hall effect: an incompressible quantum fluid with fractionally charged excitations," *Physical Review Letters*, vol. 50, no. 18, p. 1395, 1983. 39

[33] C. Kane and C. O. Head, "Topological band theory and the Z2 invariant," *Topological Insulators*, vol. 6, p. 1, 2013. 41, 42

[34] F. Ortmann, S. Roche, and S. O. Valenzuela, *Topological insulators: Fundamentals and perspectives.* John Wiley & Sons, 2015. 41, 42, 43

[35] J. E. Avron, D. Osadchy, and R. Seiler, "A topological look at the quantum Hall effect," *Physics Today*, vol. 56, no. 8, pp. 38–42, 2003. 41, 42

[36] S.-s. Chern, "A simple intrinsic proof of the Gauss-Bonnet formula for closed Riemannian manifolds," *Annals of mathematics*, pp. 747–752, 1944. 41

[37] D. Thouless, M. Kohmoto, M. Nightingale, and M. Den Nijs, "Quantized Hall conductance in a two-dimensional periodic potential," *Physical Review Letters*, vol. 49, no. 6, p. 405, 1982. 42

[38] F. D. M. Haldane, "Model for a quantum Hall effect without landau levels: Condensed-matter realization of the" parity anomaly"," *Physical Review Letters*, vol. 61, no. 18, p. 2015, 1988. 42, 107

[39] C.-X. Liu, S.-C. Zhang, and X.-L. Qi, "The quantum anomalous Hall effect: Theory and experiment," *Annual Review of Condensed Matter Physics*, vol. 7, pp. 301–321, 2016. 42

[40] C.-Z. Chang and M. Li, "Quantum anomalous Hall effect in time-reversal-symmetry breaking topological insulators," *Journal of Physics: Condensed Matter*, vol. 28, no. 12, p. 123002, 2016. 42

[41] K. He, Y. Wang, and Q.-K. Xue, "Quantum anomalous Hall effect," *National Science Review*, vol. 1, no. 1, pp. 38–48, 2014. 42

[42] X. Kou, Y. Fan, M. Lang, P. Upadhyaya, and K. L. Wang, "Magnetic topological insulators and quantum anomalous Hall effect," *Solid State Communications*, vol. 215, pp. 34–53, 2015. 42, 44

[43] R. Yu, W. Zhang, H.-J. Zhang, S.-C. Zhang, X. Dai, and Z. Fang, "Quantized anomalous Hall effect in magnetic topological insulators," *Science*, vol. 329, no. 5987, pp. 61–64, 2010. 42, 108

[44] X.-L. Qi, T. L. Hughes, and S.-C. Zhang, "Topological field theory of time-reversal invariant insulators," *Physical Review B*, vol. 78, no. 19, p. 195424, 2008. 44, 108

[45] C.-Z. Chang, J. Zhang, X. Feng, J. Shen, Z. Zhang, M. Guo, K. Li, Y. Ou, P. Wei, L.-L. Wang, *et al.*, "Experimental observation of the quantum anomalous Hall effect in a magnetic topological insulator," *Science*, vol. 340, no. 6129, pp. 167–170, 2013. 44, 104, 107, 110

[46] D. Mast, A. Dahm, and A. Fetter, "Observation of bulk and edge magnetoplasmons in a two-dimensional electron fluid," *Physical review letters*, vol. 54, no. 15, p. 1706, 1985. 45, 93

[47] D. C. Glattli, E. Y. Andrei, G. Deville, J. Poitrenaud, and F. I. B. Williams, "Dynamical Hall effect in a two-dimensional classical plasma," *Physical review letters*, vol. 54, no. 15, p. 1710, 1985. 45, 93

[48] A. L. Fetter, "Edge magnetoplasmons in a bounded two-dimensional electron fluid," *Physical Review B*, vol. 32, no. 12, p. 7676, 1985. 45

[49] V. Volkov and S. Mikhailov, "Theory of edge magnetoplasmons in a two-dimensional electron gas," *Soviet Journal of Experimental and Theoretical Physics Letters*, vol. 42, p. 556, 1985. 45, 148

[50] V. Volkov and S. Mikhailov, "Edge magnetoplasmons-low-frequency weakly damped excitations in homogeneous two-dimensional electron systems," *Zhurnal Eksperimentalnoi i Teoreticheskoi Fiziki*, vol. 94, pp. 217–241, 1988. 45, 46, 47, 93, 94, 108

[51] O. Kirichek and S. A. Mikhailov, "Edge and inter-edge magnetoplasmons in two-dimensional electron systems.," in *Edge excitation of low-dimensional charged systems*, pp. 1–47, Nova Science Publishers Inc., 2001. 45, 47

[52] R. Ashoori, H. Störmer, L. Pfeiffer, K. Baldwin, and K. West, "Edge magnetoplasmons in the time domain," *Physical Review B*, vol. 45, no. 7, p. 3894, 1992. 45, 93, 108, 148

[53] M. Field, C. G. Smith, M. Pepper, D. A. Ritchie, J. E. F. Frost, and D. G. Jones, G. A. C. amd Hasko, "Measurements of Coulomb blockade with a noninvasive voltage probe," *Phys. Rev. Lett.*, vol. 70, pp. 1311–1314, 1993. 52

[54] D. Sprinzak, Y. Ji, M. Heiblum, D. Mahalu, and H. Shtrikman, "Charge distribution in a Kondo-correlated quantum dot," *Phys. Rev. Lett.*, vol. 88, p. 176805, 2002. 52

[55] J. M. Elzerman, R. Hanson, L. H. W. van Beveren, B. Witkamp, L. M. K. Vandersypen, and L. P. Kouwenhoven, "Single-shot read-out of an individual electron spin in a quantum dot," *Nature*, vol. 430, pp. 431–435, 2004. 52, 66

[56] L. DiCarlo, H. J. Lynch, A. C. Johnson, L. I. Childress, K. Crockett, C. M. Marcus, M. P. Hanson, and A. C. Gossard, "Differential charge sensing and charge delocalization in a tunable double quantum dot," *Phys. Rev. Lett.*, vol. 92, p. 226801, 2004. 52, 66

[57] J. R. Petta, A. C. Johnson, J. M. Taylor, E. A. Laird, A. Yacoby, M. D. Lukin, C. M. Marcus, M. P. Hanson, and A. C. Gossard, "Coherent manipulation of coupled electron spins in semiconductor quantum dots," *Science*, vol. 309, no. 5744, pp. 2180–2184, 2005. 52, 122

[58] S. Amasha, K. MacLean, I. P. Radu, D. M. Zumbühl, M. A. Kastner, M. P. Hanson, and A. C. Gossard, "Electrical control of spin relaxation in a quantum dot," *Phys. Rev. Lett.*, vol. 100, p. 046803, 2008. 52, 66

[59] B. M. Maune, M. G. Borselli, B. Huang, T. D. Ladd, P. W. Deelman, K. S. Holabird, A. A. Kiselev, I. Alvarado-Rodriguez, R. S. Ross, A. E. Schmitz, M. Sokolich, C. A. Watson, M. F. Gyure, and A. T. Hunter, "Coherent singlet-triplet oscillations in a silicon-based double quantum dot," *Nature*, vol. 481, pp. 344–347, 2012. 52

[60] W. Lu, J. Shongqing, L. Pfeiffer, K. W. West, and A. J. Rimberg, “Real-time detection of electron tunnelling in a quantum dot,” *Nature*, vol. 423, pp. 422–425, 2003. 52, 66

[61] M. Yuan, F. Pan, Z. Yang, T. J. Gilheart, F. Chen, D. E. Savage, M. G. Lagally, M. A. Eriksson, and A. J. Rimberg, “Si/SiGe quantum dot with superconducting single-electron transistor charge sensor,” *Appl. Phys. Lett.*, vol. 98, p. 142104, 2011. 52

[62] M. H. Devoret and R. J. Schoelkopf, “Amplifying quantum signals with the single-electron transistor,” *Nature*, vol. 406, pp. 1039–1046, 2000. 52

[63] C. Barthel, D. J. Reilly, C. M. Marcus, M. P. Hanson, and A. C. Gossard, “Rapid single-shot measurement of a Singlet-Triplet qubit,” *Phys. Rev. Lett.*, vol. 103, p. 160503, 2009. 52, 66, 92, 130, 153

[64] M. D. Shulman, O. E. Dial, S. P. Harvey, H. Bluhm, V. Umansky, and A. Yacoby, “Demonstration of entanglement of electrostatically coupled Singlet-Triplet qubits,” *Science*, vol. 336, no. 6078, pp. 202–205, 2012. 52, 122, 131

[65] R. C. Ashoori, H. L. Störmer, J. S. Weiner, L. N. Pfeiffer, S. J. Pearton, K. W. Baldwin, and K. W. West, “Single-electron capacitance spectroscopy of discrete quantum levels,” *Phys. Rev. Lett.*, vol. 68, pp. 3088–3091, 1992. 52

[66] S. Ilani, L. Donev, M. Kindermann, and P. McEuen, “Measurement of the quantum capacitance of interacting electrons in carbon nanotubes,” *Nat. Phys.*, vol. 2, pp. 687–691, 2006. 52, 79

[67] T. Ota, T. Hayashi, K. Muraki, and T. Fujisawa, “Wide-band capacitance measurement on a semiconductor double quantum dot for studying tunneling dynamics,” *Appl. Phys. Lett.*, vol. 96, p. 032104, 2010. 52

[68] D. J. Heinzen and M. S. Feld, “Vacuum radiative level shift and spontaneous-emission linewidth of an atom in an optical resonator,” *Phys. Rev. Lett*, vol. 59, pp. 2623–2626, 1987. 52

[69] T. Duty, G. Johansson, K. Bladh, D. Gunnarsson, C. Wilsonand, and P. Delsing,

"Observation of quantum capacitance in the cooper-pair transistor," *Phys. Rev. Lett.*, vol. 95, p. 206807, 2005. 52

[70] L. Roschier, M. Sillanpää, and P. Hakonen, "Quantum capacitive phase detector," *Phys. Rev. B.*, vol. 71, p. 024530, 2005. 52

[71] A. Wallraff, D. I. Schuster, A. Blais, L. Frunzio, J. Majer, M. H. Devoret, S. M. Girvin, and R. J. Schoelkopfs, "Approaching unit visibility for control of a superconducting qubit with dispersive readout," *Phys. Rev. Lett*, vol. 95, p. 060501, 2005. 52

[72] M. D. LaHaye, J. Suh, P. M. Echternach, K. C. Schwab, and M. L. Roukes, "Nanomechanical measurements of a superconducting qubit," *Nature*, vol. 459, pp. 960–964, 2009. 52

[73] T. Frey, P. J. Leek, M. Beck, A. Blais, T. Ihn, K. Ensslin, and A. Wallraff, "Dipole coupling of a double quantum dot to a microwave resonator," *Phys. Rev. Lett.*, vol. 108, p. 046807, 2012. 52, 128

[74] H. Toida, T. Nakajima, and S. Komiyama, "Vacuum Rabi splitting in a semiconductor circuit qed system," *Phys. Rev. Lett.*, vol. 110, p. 066802, 2013. 52

[75] T. Frey, P. J. Leek, M. Beck, J. Faist, A. Wallraff, K. Ensslin, and T. Ihn, "Quantum dot admittance probed at microwave frequencies with an on-chip resonator," *Phys. Rev. B*, vol. 86, p. 115303, 2012. 52, 53

[76] K. Petersson, L. McFaul, M. Schroer, M. Jung, J. M. Taylor, A. A. Houck, and J. Petta, "Circuit quantum electrodynamics with a spin qubit," *Nature*, vol. 490, no. 7420, pp. 380–383, 2012. 52

[77] M. R. Delbecq, V. Schmitt, F. D. Parmentier, N. Roch, J. J. Viennot, G. Fève, B. Huard, C. Mora, A. Cottet, , and T. Kontos, "Coupling a quantum Dot, fermionic leads, and a microwave cavity on a chip," *Phys. Rev. Lett.*, vol. 107, p. 256804, 2011. 52

[78] K. D. Petersson, C. G. Smith, D. Anderson, P. Atkinson, G. A. C. Jones, and D. A. Ritchie, "Charge and spin state readout of a double quantum dot coupled to a resonator," *Nano. Lett.*, vol. 10, pp. 2789–2793, 2010. 52, 55, 59, 78, 131

[79] S. J. Chorley, J. Wabnig, Z. V. Penfold-Fitch, K. D. Petersson, J. Frake, C. G. Smith, and M. R. Buitelaar, “Measuring the complex admittance of a carbon nanotube double quantum dot,” *Phys. Rev. Lett.*, vol. 108, p. 036802, 2012. 52, 56

[80] M. D. Schroer, M. Jung, K. D. Petersson, and J. R. Petta, “Radio frequency charge parity meter,” *Phys. Rev. Lett.*, vol. 109, p. 166804, 2012. 52, 59

[81] J. I. Colless and D. J. Reilly, “Cryogenic high-frequency readout and control platform for spin qubits,” *Rev. Sci. Instrum.*, vol. 83, p. 023902, 2012. 53, 67, 175

[82] C. Barthel, J. Medford, C. M. Marcus, M. P. Hanson, and A. C. Gossard, “Interlaced dynamical decoupling and coherent operation of a Singlet-Triplet qubit,” *Phys. Rev. Lett.*, vol. 105, p. 266808, 2010. 55

[83] J. Gabelli, G. Fève, J. M. Berroir, B. Placais, A. Cavanna, B. Etienne, Y. Jin, and D. C. Glattli, “Violation of Kirchhoff’s Laws for a coherent RC circuit,” *Science*, vol. 313, no. 5786, pp. 499–502, 2006. 56

[84] S. Gustavsson, I. Shorubalko, R. Leturcq, T. Ihn, K. Ensslin, and S. Schön, “Detecting terahertz current fluctuations in a quantum point contact using a nanowire quantum dot,” *Phys. Rev. B*, vol. 78, p. 035324, 2008. 59

[85] T. R. Stevenson, F. A. Pellerano, C. M. Stahle, K. Aidala, and R. J. Schoelkopf, “Multiplexing of radio-frequency single-electron transistors,” *Appl. Phys. Lett.*, vol. 80, pp. 3012–3014, 2002. 62, 66

[86] T. M. Buehler, D. J. Reilly, R. P. Starrett, A. D. Greentree, A. R. Hamilton, A. S. Dzurak, and R. G. Clark, “Single-shot readout with the radio frequency single electron transistor in the presence of charge noise,” *Appl. Phys. Lett.*, vol. 86, p. 143117, 2005. 62, 66, 130

[87] A. Morello, J. J. Pla, F. A. Zwanenburg, K. W. Chan, K. Y. Tan, H. Huebl, M. Möttönen, C. D. Nugroho, C. Yang, J. A. van Donkelaar, A. D. C. Alves, D. N. Jamieson, C. C. Escott, L. C. L. Hollenberg, R. G. Clark, and A. S. Dzurak, “Single-shot readout of an electron spin in silicon,” *Nature*, vol. 467, pp. 687–691, 2010. 62

[88] V. Mourik, K. Zuo, S. M. Frolow, S. R. Plissard, E. P. A. M. Bakkers, and L. P. Kouwenhoven, “Signatures of Majorana fermions in hybrid superconductor-semiconductor nanowire devices,” *Science*, vol. 336, no. 6084, pp. 1003–1007, 2012. 62, 122

[89] M. H. Devoret and R. J. Schoelkopf, “Superconducting circuits for quantum information: An outlook,” *Science*, vol. 339, no. 6124, pp. 1169–1174, 2013. 66

[90] J. Colless, A. Mahoney, J. Hornibrook, A. Doherty, H. Lu, A. Gossard, and D. Reilly, “Dispersive readout of a few-electron double quantum dot with fast rf gate sensors,” *Physical review letters*, vol. 110, no. 4, p. 046805, 2013. 66, 67, 72, 78, 85, 92, 153

[91] P. K. Day, H. G. LeDuc, B. A. Mazin, A. Vayonakis, and J. Zmuidzinas, “A broadband superconducting detector suitable for use in large arrays,” *Nature*, vol. 425, pp. 817–821, 2003. 66

[92] Y. Chen, D. Sank, P. O’Malley, T. White, R. Barends, B. Chiaro, J. Kelly, E. Lucero, M. Mariantoni, A. Megrant, C. Neill, A. Vainsencher, J. Wenner, Y. Yin, A. N. Cleland, and J. M. Martinis, “Multiplexed dispersive readout of superconducting phase qubits,” *Appl. Phys. Lett.*, vol. 101, p. 182601, 2012. 66

[93] M. Jerger, S. Poletto, P. Macha, U. Hübner, E. Il’ichev, and A. V. Ustinov, “Frequency division multiplexing readout and simultaneous manipulation of an array of flux qubits,” *Appl. Phys. Lett.*, vol. 101, p. 042604, 2012. 66

[94] M. J. Biercuk, D. J. Reilly, T. M. Buehler, V. C. Chan, J. M. Chow, R. G. Clark, and C. M. Marcus, “Charge sensing in carbon-nanotube quantum dots on microsecond timescale,” *Phys. Rev. B.*, vol. 73, p. 201402, 2006. 66

[95] S. S. Mohan, M. Henderson, S. P. Boyd, and T. H. Lee, “Simple accurate expressions for planar spiral inductances,” *IEEE Journal of Solid-State Circuits*, vol. 34, pp. 1419–1424, 1999. 69

[96] J. Zmuidzinas, “Superconducting microresonators: Physics and applications,” *Annu. Rev. Condens. Matter Phys.*, vol. 3, pp. 169–214, 2012. 74

[97] R. Landauer, "Spatial variation of currents and fields due to localized scatterers in metallic conduction," *IBM Journal of Research and Development*, vol. 1, no. 3, pp. 223–231, 1957. 78

[98] R. Landauer, "Conductance determined by transmission: probes and quantised constriction resistance," *Journal of Physics: Condensed Matter*, vol. 1, no. 43, p. 8099, 1989. 78

[99] K. Thomas, J. Nicholls, M. Simmons, M. Pepper, D. Mace, and D. Ritchie, "Possible spin polarization in a one-dimensional electron gas," *Physical Review Letters*, vol. 77, no. 1, p. 135, 1996. 78

[100] D. Reilly, "Phenomenological model for the 0.7 conductance feature in quantum wires," *Physical Review B*, vol. 72, no. 3, p. 033309, 2005. 78

[101] Y. Meir, K. Hirose, and N. S. Wingreen, "Kondo model for the "0.7 anomaly" in transport through a quantum point contact," *Physical review letters*, vol. 89, no. 19, p. 196802, 2002. 78

[102] S. Cronenwett, H. Lynch, D. Goldhaber-Gordon, L. Kouwenhoven, C. Marcus, K. Hirose, N. Wingreen, and V. Umansky, "Low-temperature fate of the 0.7 structure in a point contact: a Kondo-like correlated state in an open system," *Physical review letters*, vol. 88, no. 22, p. 226805, 2002. 78

[103] T. Rejec and Y. Meir, "Magnetic impurity formation in quantum point contacts," *Nature*, vol. 442, no. 7105, pp. 900–903, 2006. 78

[104] P. M. Wu, P. Li, H. Zhang, and A. Chang, "Evidence for the formation of quasibound states in an asymmetrical quantum point contact," *Physical Review B*, vol. 85, no. 8, p. 085305, 2012. 78

[105] M. Iqbal, R. Levy, E. Koop, J. Dekker, J. De Jong, J. van der Velde, D. Reuter, A. Wieck, R. Aguado, Y. Meir, *et al.*, "Odd and even Kondo effects from emergent localization in quantum point contacts," *Nature*, vol. 501, no. 7465, pp. 79–83, 2013. 78

[106] B. Brun, F. Martins, S. Faniel, B. Hackens, G. Bachelier, A. Cavanna, C. Ulysse, A. Ouerghi, U. Gennser, D. Mailly, *et al.*, "Wigner and Kondo physics in quantum

point contacts revealed by scanning gate microscopy," *Nature communications*, vol. 5, 2014. 78, 85

[107] M. Jung, M. Schroer, K. Petersson, and J. Petta, "Radio frequency charge sensing in InAs nanowire double quantum dots," *Applied Physics Letters*, vol. 100, no. 25, p. 253508, 2012. 78

[108] S. Lüscher, L. S. Moore, T. Rejec, Y. Meir, H. Shtrikman, and D. Goldhaber-Gordon, "Charge rearrangement and screening in a quantum point contact," *Physical review letters*, vol. 98, no. 19, p. 196805, 2007. 79

[109] L. Smith, A. Hamilton, K. Thomas, M. Pepper, I. Farrer, J. Griffiths, G. Jones, and D. Ritchie, "Compressibility measurements of quasi-one-dimensional quantum wires," *Physical review letters*, vol. 107, no. 12, p. 126801, 2011. 79

[110] J. M. Hornibrook, J. I. Colless, A. C. Mahoney, X. G. Croot, S. Blanvillain, H. Lu, A. C. Gossard, and D. J. Reilly, "Frequency multiplexing for readout of spin qubits," *Appl. Phys. Lett.*, vol. 104, p. 103108, 2014. 79, 80

[111] M. Topinka, B. LeRoy, R. Westervelt, S. Shaw, R. Fleischmann, E. Heller, K. Maranowski, and A. Gossard, "Coherent branched flow in a two-dimensional electron gas," *Nature*, vol. 410, no. 6825, pp. 183–186, 2001. 85

[112] M. Jura, M. Topinka, M. Grobis, L. Pfeiffer, K. West, and D. Goldhaber-Gordon, "Electron interferometer formed with a scanning probe tip and quantum point contact," *Physical Review B*, vol. 80, no. 4, p. 041303, 2009. 85

[113] B. Brun, F. Martins, S. Faniel, B. Hackens, A. Cavanna, C. Ulysse, A. Ouerghi, U. Gennser, D. Mailly, P. Simon, *et al.*, "Electron phase shift at the zero-bias anomaly of quantum point contacts," *Physical review letters*, vol. 116, no. 13, p. 136801, 2016. 85

[114] Y. Komijani, M. Csontos, T. Ihn, K. Ensslin, Y. Meir, D. Reuter, and A. Wieck, "Origins of conductance anomalies in a p-type GaAs quantum point contact," *Physical Review B*, vol. 87, no. 24, p. 245406, 2013. 87

[115] R. Fleury, D. L. Sounas, C. F. Sieck, M. R. Haberman, and A. Alù, “Sound isolation and giant linear nonreciprocity in a compact acoustic circulator,” *Science*, vol. 343, no. 6170, pp. 516–519, 2014. 92

[116] L. Feng, M. Ayache, J. Huang, Y. Xu, M. Lu, Y. Chen, Y. Fainman, and A. Scherer, “Nonreciprocal light propagation in a silicon photonic circuit,” *Science*, vol. 333, no. 6043, pp. 729–733, 2011. 92

[117] L. Bi, J. Hu, P. Jiang, D. Kim, G. Dionne, L. Kimerling, and C. Ross, “On-chip optical isolation in monolithically integrated non-reciprocal optical resonators,” *Nature Photonics*, vol. 5, no. 12, pp. 758–762, 2011. 92

[118] N. Estep, D. Sounas, J. Soric, and A. Alù, “Magnetic-free non-reciprocity and isolation based on parametrically modulated coupled-resonator loops,” *Nature Physics*, vol. 10, no. 12, pp. 923–927, 2014. 92

[119] T. Stace, C. Barnes, and G. Milburn, “Mesoscopic one-way channels for quantum state transfer via the quantum Hall effect,” *Physical review letters*, vol. 93, no. 12, p. 126804, 2004. 92

[120] J. Kerckhoff, K. Lalumière, B. Chapman, A. Blais, and K. Lehnert, “On-chip superconducting microwave circulator from synthetic rotation,” *Physical Review Applied*, vol. 4, no. 3, p. 034002, 2015. 92

[121] B. Abdo, K. Sliwa, L. Frunzio, and M. Devoret, “Directional amplification with a josephson circuit,” *Physical Review X*, vol. 3, no. 3, p. 031001, 2013. 92

[122] K. Sliwa, M. Hatridge, A. Narla, S. Shankar, L. Frunzio, R. Schoelkopf, and M. Devoret, “Reconfigurable josephson circulator/directional amplifier,” *Physical Review X*, vol. 5, no. 4, p. 041020, 2015. 92

[123] G. Viola and D. P. DiVincenzo, “Hall effect gyrators and circulators,” *Physical Review X*, vol. 4, no. 2, p. 021019, 2014. 92, 100, 108, 112, 154

[124] W. Mason, W. Hewitt, and R. Wick, “Hall effect modulators and“gyrators”employing magnetic field independent orientations in germanium,” *Journal of Applied Physics*, vol. 24, no. 2, pp. 166–175, 1953. 92

[125] R. Wick, “Solution of the field problem of the germanium gyrator,” *Journal of Applied Physics*, vol. 25, no. 6, pp. 741–756, 1954. 92

[126] M. Büttiker, “Absence of backscattering in the quantum Hall effect in multiprobe conductors,” *Physical Review B*, vol. 38, no. 14, p. 9375, 1988. 92

[127] J. Pla, K. Tan, J. Dehollain, W. Lim, J. Morton, D. Jamieson, A. Dzurak, and A. Morello, “A single-atom electron spin qubit in silicon,” *Nature*, vol. 489, no. 7417, pp. 541–545, 2012. 92

[128] A. Miroshnichenko, S. Flach, and Y. Kivshar, “Fano resonances in nanoscale structures,” *Reviews of Modern Physics*, vol. 82, no. 3, p. 2257, 2010. 93, 100

[129] E. Andrei, D. Glattli, F. Williams, and M. Heiblum, “Low frequency collective excitations in the quantum-Hall system,” *Surface Science*, vol. 196, no. 1, pp. 501–506, 1988. 93, 148

[130] V. Talyanskii, M. Wassermeier, A. Wixforth, J. Oshinowo, J. Kotthaus, I. Batov, G. Weimann, H. Nickel, and W. Schlapp, “Edge magnetoplasmons in the quantum Hall effect regime,” *Surface Science*, vol. 229, no. 1-3, pp. 40–42, 1990. 93, 148

[131] N. Zhitenev, R. Haug, K. v. Klitzing, and K. Eberl, “Experimental determination of the dispersion of edge magnetoplasmons confined in edge channels,” *Physical Review B*, vol. 49, no. 11, p. 7809, 1994. 93, 148

[132] N. Kumada, S. Tanabe, H. Hibino, H. Kamata, M. Hashisaka, K. Muraki, and T. Fujisawa, “Plasmon transport in graphene investigated by time-resolved electrical measurements,” *Nature communications*, vol. 4, p. 1363, 2013. 93, 102, 110, 148

[133] I. Petković, F. Williams, K. Bennaceur, F. Portier, P. Roche, and D. Glattli, “Carrier drift velocity and edge magnetoplasmons in graphene,” *Physical review letters*, vol. 110, no. 1, p. 016801, 2013. 93, 110, 148

[134] N. Kumada, P. Roulleau, B. Roche, M. Hashisaka, H. Hibino, I. Petković, and D. Glattli, “Resonant edge magnetoplasmons and their decay in graphene,” *Physical review letters*, vol. 113, no. 26, p. 266601, 2014. 93, 110, 148

[135] N. Kumada, H. Kamata, and T. Fujisawa, “Edge magnetoplasmon transport in gated and ungated quantum Hall systems,” *Physical Review B*, vol. 84, no. 4, p. 045314, 2011. 93, 110, 113, 148

[136] H. Kamata, T. Ota, K. Muraki, and T. Fujisawa, “Voltage-controlled group velocity of edge magnetoplasmon in the quantum Hall regime,” *Physical Review B*, vol. 81, no. 8, p. 085329, 2010. 93, 110, 113, 148

[137] J. Cano, A. Doherty, C. Nayak, and D. Reilly, “Microwave absorption by a mesoscopic quantum Hall droplet,” *Physical Review B*, vol. 88, no. 16, p. 165305, 2013. 93, 125, 129

[138] N. Balaban, U. Meirav, H. Shtrikman, and V. Umansky, “Observation of the logarithmic dispersion of high-frequency edge excitations,” *Physical Review B*, vol. 55, no. 20, p. R13397, 1997. 93, 148

[139] S. Bosco, F. Haupt, and D. P. DiVincenzo, “Self-impedance-matched Hall-effect gyrators and circulators,” *Phys. Rev. Applied*, vol. 7, p. 024030, Feb 2017. 95, 108, 126, 127, 153

[140] B. Placke, S. Bosco, and D. P. DiVincenzo, “A model study of present-day Hall-effect circulators,” *arXiv preprint arXiv:1609.09624*, 2016. 95, 116, 153

[141] D. Druist, P. Turley, K. Maranowski, E. Gwinn, and A. Gossard, “Observation of chiral surface states in the integer quantum Hall effect,” *Physical review letters*, vol. 80, no. 2, p. 365, 1998. 95

[142] H. Kamata, N. Kumada, M. Hashisaka, K. Muraki, and T. Fujisawa, “Fractionalized wave packets from an artificial Tomonaga-Luttinger liquid,” *Nature nanotechnology*, vol. 9, no. 3, pp. 177–181, 2014. 102

[143] X. Kou, S.-T. Guo, Y. Fan, L. Pan, M. Lang, Y. Jiang, Q. Shao, T. Nie, K. Murata, J. Tang, *et al.*, “Scale-invariant quantum anomalous Hall effect in magnetic topological insulators beyond the two-dimensional limit,” *Physical review letters*, vol. 113, no. 13, p. 137201, 2014. 107, 110

[144] J. Checkelsky, R. Yoshimi, A. Tsukazaki, K. Takahashi, Y. Kozuka, J. Falson, M. Kawasaki, and Y. Tokura, “Trajectory of the anomalous Hall effect towards

the quantized state in a ferromagnetic topological insulator," *Nature Physics*, vol. 10, no. 10, pp. 731–736, 2014. 107, 110

[145] C.-Z. Chang, W. Zhao, D. Y. Kim, H. Zhang, B. A. Assaf, D. Heiman, S.-C. Zhang, C. Liu, M. H. Chan, and J. S. Moodera, "High-precision realization of robust quantum anomalous Hall state in a hard ferromagnetic topological insulator," *Nature materials*, vol. 14, no. 5, pp. 473–477, 2015. 107, 125

[146] M. Z. Hasan and C. L. Kane, "Colloquium: topological insulators," *Reviews of Modern Physics*, vol. 82, no. 4, p. 3045, 2010. 107

[147] A. Bestwick, E. Fox, X. Kou, L. Pan, K. L. Wang, and D. Goldhaber-Gordon, "Precise quantization of the anomalous Hall effect near zero magnetic field," *Physical review letters*, vol. 114, no. 18, p. 187201, 2015. 107, 110, 116, 119

[148] J. Wang, B. Lian, H. Zhang, and S.-C. Zhang, "Anomalous edge transport in the quantum anomalous Hall state," *Physical review letters*, vol. 111, no. 8, p. 086803, 2013. 107, 119

[149] C.-Z. Chang, W. Zhao, D. Y. Kim, P. Wei, J. K. Jain, C. Liu, M. H. W. Chan, and J. S. Moodera, "Zero-field dissipationless chiral edge transport and the nature of dissipation in the quantum anomalous Hall state," *Phys. Rev. Lett.*, vol. 115, p. 057206, Jul 2015. 107, 119

[150] C.-X. Liu, X.-L. Qi, X. Dai, Z. Fang, and S.-C. Zhang, "Quantum anomalous Hall effect in $\mathrm{Hg}_{1-y}\mathrm{Mn}_y\mathrm{Te}$ quantum wells," *Physical review letters*, vol. 101, no. 14, p. 146802, 2008. 108

[151] X.-L. Qi and S.-C. Zhang, "Topological insulators and superconductors," *Reviews of Modern Physics*, vol. 83, no. 4, p. 1057, 2011. 108

[152] K. Nomura and N. Nagaosa, "Surface-quantized anomalous Hall current and the magnetoelectric effect in magnetically disordered topological insulators," *Physical review letters*, vol. 106, no. 16, p. 166802, 2011. 108

[153] V. Talyanskii, A. Polisski, D. Arnone, M. Pepper, C. Smith, D. Ritchie, J. Frost, and G. Jones, "Spectroscopy of a two-dimensional electron gas in the quantum-

Hall-effect regime by use of low-frequency edge magnetoplasmons," *Physical Review B*, vol. 46, no. 19, p. 12427, 1992. 108

[154] J. C. W. Song and M. S. Rudner, "Chiral plasmons without magnetic field," *Proceedings of the National Academy of Sciences*, vol. 113, no. 17, pp. 4658–4663, 2016. 108

[155] A. C. Mahoney, J. I. Colless, S. J. Pauka, J. M. Hornibrook, J. D. Watson, G. C. Gardner, M. J. Manfra, A. C. Doherty, and D. J. Reilly, "On-chip microwave quantum Hall circulator," *Phys. Rev. X*, vol. 7, p. 011007, Jan 2017. 108, 110, 112, 113, 116

[156] J. Wang, B. Lian, and S.-C. Zhang, "Universal scaling of the quantum anomalous Hall plateau transition," *Physical Review B*, vol. 89, no. 8, p. 085106, 2014. 119

[157] X. Kou, L. Pan, J. Wang, Y. Fan, E. S. Choi, W.-L. Lee, T. Nie, K. Murata, Q. Shao, S.-C. Zhang, *et al.*, "Metal-to-insulator switching in quantum anomalous Hall states," *Nature communications*, vol. 6, 2015. 119

[158] Y. Feng, X. Feng, Y. Ou, J. Wang, C. Liu, L. Zhang, D. Zhao, G. Jiang, S.-C. Zhang, K. He, *et al.*, "Observation of the zero Hall plateau in a quantum anomalous Hall insulator," *Physical review letters*, vol. 115, no. 12, p. 126801, 2015. 119

[159] W. Li, M. Claassen, C.-Z. Chang, B. Moritz, T. Jia, C. Zhang, S. Rebec, J. Lee, M. Hashimoto, D.-H. Lu, *et al.*, "Origin of the low critical observing temperature of the quantum anomalous Hall effect in V-doped (Bi, Sb)$_2$Te$_3$ film," *Scientific Reports*, vol. 6, 2016. 119

[160] D. Loss and D. DiVincenzo, "Quantum computation with quantum dots," *Phys. Rev. A*, vol. 57, pp. 120–126, 1998. 122

[161] M. Veldhorst, J. Hwang, C. Yang, A. Leenstra, B. De Ronde, J. Dehollain, J. Muhonen, F. Hudson, K. M. Itoh, A. Morello, *et al.*, "An addressable quantum dot qubit with fault-tolerant control-fidelity," *Nature nanotechnology*, vol. 9, no. 12, pp. 981–985, 2014. 122

[162] M. Veldhorst, C. Yang, J. Hwang, W. Huang, J. Dehollain, J. Muhonen, S. Simmons, A. Laucht, F. Hudson, K. M. Itoh, *et al.*, “A two-qubit logic gate in silicon,” *Nature*, 2015. 122

[163] E. Kawakami, P. Scarlino, D. Ward, F. Braakman, D. Savage, M. Lagally, M. Friesen, S. Coppersmith, M. Eriksson, and L. Vandersypen, “Electrical control of a long-lived spin qubit in a Si/SiGe quantum dot,” *Nature nanotechnology*, vol. 9, no. 9, pp. 666–670, 2014. 122

[164] K. Eng, T. D. Ladd, A. Smith, M. G. Borselli, A. A. Kiselev, B. H. Fong, K. S. Holabird, T. M. Hazard, B. Huang, P. W. Deelman, *et al.*, “Isotopically enhanced triple-quantum-dot qubit,” *Science advances*, vol. 1, no. 4, p. e1500214, 2015. 122

[165] B. E. Kane, “A silicon-based nuclear spin quantum computer,” *Nature*, pp. 133–137, 1998. 122

[166] J. J. Pla, K. Y. Tan, J. P. Dehollain, W. H. Lim, J. J. L. Morton, D. N. Jamieson, A. S. Dzurak, and A. Morello, “A single-atom electron spin qubit in silicon,” *Nature*, vol. 489, pp. 541–545, 2012. 122

[167] J. J. Pla, K. Y. Tan, J. P. Dehollain, W. H. Lim, J. J. L. Morton, F. A. Zwanenburg, D. N. Jamieson, A. S. Dzurak, and A. Morello, “High-fidelity readout and control of a nuclear spin qubit in silicon,” *Nature*, vol. 496, pp. 334–338, 2013. 122

[168] A. Das, Y. Ronen, Y. Most, Y. Oreg, M. Heiblum, and H. Shtrikman, “Zero-bias peaks and splitting in an Al-InAs nanowire topological superconductor as a signature of Majorana fermions,” *Nature Physics*, vol. 8, no. 12, pp. 887–895, 2012. 122

[169] D. Aasen, M. Hell, R. V. Mishmash, A. Higginbotham, J. Danon, M. Leijnse, T. S. Jespersen, J. A. Folk, C. M. Marcus, K. Flensberg, *et al.*, “Milestones toward Majorana-based quantum computing,” *Physical Review X*, vol. 6, no. 3, p. 031016, 2016. 122

[170] T. Karzig, C. Knapp, R. Lutchyn, P. Bonderson, M. Hastings, C. Nayak, J. Alicea, K. Flensberg, S. Plugge, Y. Oreg, *et al.*, “Scalable designs for quasiparticle-

poisoning-protected topological quantum computation with Majorana zero modes," *arXiv preprint arXiv:1610.05289*, 2016. 122, 131

[171] M. R. Delbecq, T. Nakajima, T. Otsuka, S. Amaha, J. D. Watson, M. J. Manfra, and S. Tarucha, "Full control of quadruple quantum dot circuit charge states in the single electron regime," *Appl. Phys. Lett.*, vol. 104, p. 183111, 2014. 122

[172] D. J. Reilly, "Engineering the quantum-classical interface of solid-state qubits," *npj Quantum Information*, vol. 1, p. 15011, 2015. 123, 134

[173] Y. Han, J.-G. Wan, G.-X. Ge, F.-Q. Song, and G.-H. Wang, "High-temperature quantum anomalous Hall effect in honeycomb bilayer consisting of au atoms and single-vacancy graphene," *Scientific reports*, vol. 5, 2015. 125

[174] S. Qi, Z. Qiao, X. Deng, E. D. Cubuk, H. Chen, W. Zhu, E. Kaxiras, S. Zhang, X. Xu, and Z. Zhang, "High-temperature quantum anomalous Hall effect in n- p codoped topological insulators," *Physical Review Letters*, vol. 117, no. 5, p. 056804, 2016. 125

[175] H. Wang, W. Luo, and H. Xiang, "Prediction of high-temperature quantum anomalous Hall effect in two-dimensional transition-metal oxides," *Physical Review B*, vol. 95, no. 12, p. 125430, 2017. 125

[176] D. M. Pozar, *Microwave engineering.* John Wiley & Sons, 2009. 126

[177] L. Trifunovic, O. Dial, M. Trif, J. R. Wootton, R. Abebe, A. Yacoby, and D. Loss, "Long-distance spin-spin coupling via floating gates," *Phys. Rev. X.*, vol. 2, p. 011006, 2012. 128

[178] M. Serina, L. Trifunovic, C. Kloeffel, and D. Loss, "Long-range interaction between charge and spin qubits in quantum dots," *arXiv preprint arXiv:1601.03564*, 2016. 128

[179] G. Burkard and A. Imamoglu, "Ultra-long-distance interaction between spin qubits," *Physical Review B*, vol. 74, no. 4, p. 041307, 2006. 128

[180] J. Taylor and M. Lukin, "Cavity quantum electrodynamics with semiconductor double-dot molecules on a chip," *arXiv preprint cond-mat/0605144*, 2006. 128

[181] K. D. Petersson, L. W. McFaul, M. D. Schroer, M. Jung, J. M. Taylor, A. A. Houck, and J. R. Petta, "Circuit quantum electrodynamics with a spin qubit," *Nature*, vol. 490, pp. 380–383, 2012. 128

[182] L. Trifunovic, F. L. Pedrocchi, and D. Loss, "Long-Distance entanglement of spin qubits via ferromagnet," *Phys. Rev. X.*, vol. 3, p. 041023, 2013. 128

[183] V. Srinivasa, H. Xu, and J. Taylor, "Tunable spin-qubit coupling mediated by a multielectron quantum dot," *Physical review letters*, vol. 114, no. 22, p. 226803, 2015. 128

[184] G. Yang, C.-H. Hsu, P. Stano, J. Klinovaja, and D. Loss, "Long-distance entanglement of spin qubits via quantum Hall edge states," *Physical Review B*, vol. 93, no. 7, p. 075301, 2016. 128

[185] S. Elman, S. D. Bartlett, and A. C. Doherty, "Long-range entanglement for spin qubits via quantum Hall edge modes," *In preparation*, 2017. 128

[186] R. J. Schoelkopf, "The radio-frequency single-electron transistor (RF-SET): A fast and ultrasensitive electrometer," *Science*, vol. 280, no. 5367, pp. 1238–1242, 1998. 130

[187] C. Barthel, M. Kjærgaard, J. Medford, M. Stopa, C. M. Marcus, M. P. Hanson, and A. C. Gossard, "Fast sensing of double-dot charge arrangement and spin state with a radio-frequency sensor quantum dot," *Phys. Rev. B*, vol. 81, p. 161308, 2010. 130

[188] A. Betz, R. Wacquez, M. Vinet, X. Jehl, A. Saraiva, M. Sanquer, A. Ferguson, and M. Gonzalez-Zalba, "Dispersively detected pauli spin-blockade in a silicon nanowire field-effect transistor," *Nano letters*, vol. 15, no. 7, pp. 4622–4627, 2015. 131

[189] I. Siddiqi, R. Vijay, F. Pierre, C. Wilson, M. Metcalfe, C. Rigetti, L. Frunzio, and M. Devoret, "Rf-driven Josephson bifurcation amplifier for quantum measurement," *Physical review letters*, vol. 93, no. 20, p. 207002, 2004. 132

[190] T. Yamamoto, K. Inomata, M. Watanabe, K. Matsuba, T. Miyazaki, W. Oliver,

Y. Nakamura, and J. Tsai, “Flux-driven Josephson parametric amplifier,” *Applied Physics Letters*, vol. 93, no. 4, p. 042510, 2008. 132

[191] R. Vijay, M. Devoret, and I. Siddiqi, “Invited review article: The Josephson bifurcation amplifier,” *Review of Scientific Instruments*, vol. 80, no. 11, p. 111101, 2009. 132

[192] J. Stehlik, Y.-Y. Liu, C. Quintana, C. Eichler, T. Hartke, and J. Petta, “Fast charge sensing of a cavity-coupled double quantum dot using a Josephson parametric amplifier,” *Physical Review Applied*, vol. 4, no. 1, p. 014018, 2015. 132

[193] J. M. Hornibrook, J. I. Colless, I. D. Conway Lamb, S. J. Pauka, A. C. Gossard, J. D. Watson, G. C. Gardner, S. Fallahi, M. J. Manfra, and D. J. Reilly, “Cryogenic control architecture for large-scale quantum computing,” *Submitted to Phys. Rev. Applied.*, 2014. 134

[194] I. Conway Lamb, J. Colless, J. Hornibrook, S. Pauka, S. Waddy, M. Frechtling, and D. Reilly, “An FPGA-based instrumentation platform for use at deep cryogenic temperatures,” *Review of Scientific Instruments*, vol. 87, no. 1, p. 014701, 2016. 134

[195] J. I. Colless and D. J. Reilly, “Modular cryogenic interconnects for multi-qubit devices,” *Accepted in Rev. Sci. Instrum.*, 2014. 175

[196] J. Colless, *Scalable Control and Measurement of Gate-Defined Quantum Dot Systems.* PhD thesis, University of Sydney, 2015. 177

[197] J. Hornibrook, *Readout and Control Beyond a Few Qubits: Scaling-up Solid State Quantum Systems.* PhD thesis, University of Sydney, 2015. 177

[198] J. Miller, *Electron Transport in GaAs Heterostructures at Various Magnetic Field Strengths.* PhD thesis, Harvard University, February 2007. 183

This thesis was typeset using LaTeX, and created using the
template *PhDthesis version 2* style file by Jakob Suckale, 2007,
based on *CUEDthesis version 1* by Harish Bhanderi 2002
http://www-h.eng.cam.ac.uk/help/tpl/textprocessing/ThesisStyle/
made available through OpenWetWare.org


NL
SYDNEY